Air-Sea Gas Exchange in Tidal Fronts

by

Burkard Baschek
Diplom, Universität zu Kiel, 1998

A Dissertation submitted in Partial Fulfillment of the
Requirements for the Degree of

DOCTOR OF PHILOSOPHY

in the School of Earth and Ocean Sciences

We accept this dissertation as conforming to the required standard

Dr. D.M. Farmer, Supervisor (School of Earth and Ocean Sciences)

Dr. C. Garrett, Co-supervisor/Outside Member (Department of Physics and Astronomy)

Dr. E. Carmack, Departmental Member (School of Earth and Ocean Sciences)

Dr. R. Lueck, Departmental Member (School of Earth and Ocean Sciences)

Dr. P. Cummins, Additional Member (Institute of Ocean Sciences, Sidney)

Dr. W. Jenkins, External Examiner (Woods Hole Oceanographic Institution, MA, USA)

Examiners:

Dr. D.M. Farmer, Supervisor (School of Earth and Ocean Sciences)

Dr. C. Garrett, Co-supervisor/Outside Member (Department of Physics and Astronomy)

Dr. E. Carmack, Departmental Member (School of Earth and Ocean Science)

Dr. R. Lueck, Departmental Member (School of Earth and Ocean Science)

Dr. P. Cummins, Additional Member (Institute of Ocean Sciences, Sidney)

Dr. W. Jenkins, External Examiner (Woods Hole Oceanographic Institution, MA, USA)

Supervisors: Dr. D.M. Farmer, Dr. C. Garrett

Abstract

Strong tidal currents in the Fraser Estuary, BC, Canada, cause intense flow-topography interaction around islands and over shallow sills. At Boundary Pass, a steep sill forms a pronounced barrier for flow of dense water from the Pacific Ocean into the Strait of Georgia. The processes at the sill control the renewal of deep and intermediate water in the Strait.

The strong flood tidal flow forces dense water to flow over the sill. It then meets a fresh surface layer just downstream of the sill crest and subducts underneath the fresh water, setting up a hydraulic sill flow with an arrested upper layer. Vertical current speeds at the downstream side of the sill reach up to $0.75\,\mathrm{m\,s^{-1}}$, and intense detrainment of dense water from the lower into the upper layer causes a volume loss of 60% over a distance of 200 m.

Surface waves travelling into the convergence zone (tidal front) over the sill crest tend to steepen and break due to wave-current interaction. The breaking waves inject gas bubbles, which either rise back to the sea surface or dissolve completely, depending on their rise speed and the strength of the vertical currents. Bubbles injected close to the plunge point of the dense water mass are drawn down by the extreme currents to depths of up to 160 m, enhancing air-sea gas exchange.

The hydraulic flow, wave-current interaction, and gas bubble behaviour are described with simple models. They are used to interpret extensive ship-board measurements during two cruises in the Fraser estuary and help in the understanding of the physical processes involved in air-sea gas exchange in tidal fronts. The oxygen flux in the tidal front at Boundary Pass is compared with other oxygen sources in the Fraser Estuary and shows that tidal fronts

may contribute significantly to the aeration of an estuary.

The described processes may be also applicable to other coastal areas with strong tidal currents like Norway, Chile, or Japan, and may be important in convergence zones like deep convection regimes.

Table of Contents

List of Tables

List of Figures

Acknowledgements

Many thanks to my supervisors Dr. David Farmer and Dr. Chris Garrett for the opportunity to participate in an exciting project at the beautiful coast of British Columbia. I am very grateful for the many stimulating discussions and critical comments and highly appreciate their great support during my time at the University of Victoria.

I also would like to thank my committee members Dr. Patrick Cummins, Dr. Rolf Lueck, and Dr. Eddy Carmack for their helpful suggestions and discussions to improve this thesis, and I am grateful to Dr. William Jenkins for coming to Victoria as my external examiner.

I gratefully acknowledge the support and cooperation of the captains and crew of CCGS Vector, which was essential in collecting data in a navigationally very challenging environment.

I am indebted to the Ocean Acoustics Group for their wonderful support during the project and the pleasant work atmosphere at the Institute of Ocean Sciences and during the experiments on sea. Thanks also to my fellow students Frank Gerdes and Roblyn Kendall for their support in many scientific and non-scientific respects.

Many thanks to my father Bodo and brother Björn for the careful proofreading of my thesis. But most of all, I would like to thank my parents Elke and Bodo for their enduring support throughout my studies.

1 Introduction

Coastal environments are often characterized by productive but fragile ecosystems and are often important for human food resources and for recreational activities. The excess supply of nutrients and waste water by the surrounding communities can harm these ecosystems and diminish commercially valuable fish populations. It is therefore important to better understand the mechanisms responsible for the mixing of (polluted) water in coastal environments and for supplying oxygen to the water below the surface layer where the decomposition of organic material can cause oxygen depletion.

The estuary of the Fraser River in British Columbia, Canada (Figure 1.1), is a highly productive ecosystem renowned for its salmon populations. These support the fishery fleets of Canada and the USA and are the main food source of resident orcas (killer whales). Oxygen concentrations, however, can drop in the deeper regions of the Strait of Georgia (Figure 1.1) to levels at which fish are affected negatively and may be forced to move away.

In this thesis particular attention is given to the mechanisms which supply oxygen to the Strait. It is suggested that they are as follows: pronounced interaction of strong (tidal) currents with topography in parts of the estuary (Haro Strait) mixes dense water from the Pacific Ocean with fresh, oxygenated surface water (a significant portion of this oxygen is contributed by the generation and subduction of gas bubbles in tidal fronts). At the entrance to the Strait of Georgia (Boundary Pass), this water flows over a sill down to intermediate depths, from where the oxygen is likely to be transported by diffusion to the deeper parts of the Strait. Oxygen input by rare deep water renewal events of somewhat oxygenated water in spring (Masson, 2002) will not be considered.

This thesis will describe the mechanisms responsible for the supply of intermediate water in the Strait of Georgia and it will be shown that *air-sea gas exchange in tidal fronts* can contribute significantly to the aeration of an estuary.

Estuarine Circulation

The two big straits in the Fraser Estuary, Juan de Fuca Strait (160–280 m water depth) and the Strait of Georgia (200 – 440 m water depth), are connected by various smaller straits and channels (Figure 1.2). The most important one for the estuarine dynamics is Haro Strait (250 – 300 m deep, 3 – 4 km wide) which is separated from Juan de Fuca Strait by Victoria Sill (60 – 70 m water depth) and from the Strait of Georgia by a sill at Boundary

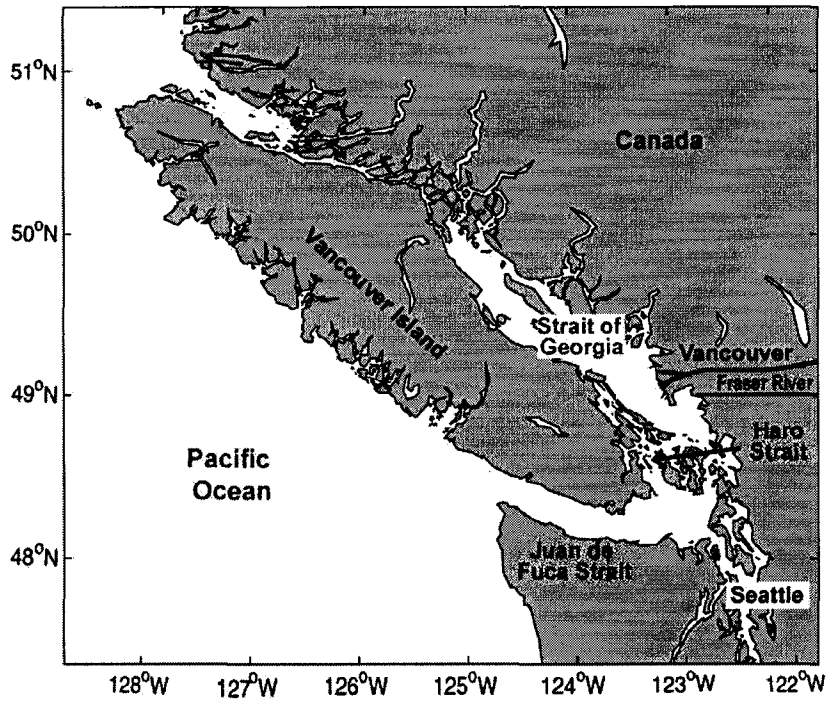

Figure 1.1: *Map of southern British Columbia, Canada. The Fraser River supplies fresh water to the estuary which flows from the Strait of Georgia through Haro Strait and Juan de Fuca Strait into the Pacific Ocean.*

Pass (60 m water depth). The total area of the estuary is 10 950 km^2, with the areas of the Strait of Georgia 6 800 km^2, Juan de Fuca Strait 3 700 km^2 (Thomson, 1994), and Haro Strait 450 km^2.

The estuary is greatly influenced by the fresh water delivered by the Fraser River, which drains an area of 217 300 km^2 and has a mean annual volume transport of 4 400 $m^3 s^{-1}$ (Thomson, 1994). This fresh water flows at the surface through Haro Strait and Juan de Fuca Strait into the Pacific Ocean, while, beneath it, saltier and denser water enters the estuary from the Pacific Ocean setting up a classical estuarine circulation. Superimposed on this mean circulation (the mean current speed in Haro Strait is about 0.2 $m s^{-1}$ and in Juan de Fuca Strait 0.05 $m s^{-1}$ (Pawlowicz & Farmer, 1998), is a strong tidal regime with pronounced spring-neap tidal variability (Pawlowicz, 2002) (see also Appendix B.1).
Predictions from a fully 3-dimensional constant density finite-element frequency-domain model (Foreman & Thomson, 1997) give some idea of the peak ebb tidal flow in Haro Strait (Figure 1.2), where current speeds can reach up to 1.3 $m s^{-1}$ like at Turn Point, Stuart Island (Fisheries and Oceans Canada, 2000). Measurements during two cruises (Section 2) showed even higher values of up to 3 $m s^{-1}$ at the sill at Boundary Pass.

Mixing and tidal fronts

As the currents in this region interact strongly with the topography, Haro Strait plays an important role in the mixing of dense water from the Pacific Ocean and fresh surface water from the Fraser River (Pawlowicz & Farmer, 1998; Farmer *et al.*, 1995). Tidal fronts (sharp transition zones of water masses with different current speed and water mass properties) develop due to flow separation past headlands (Farmer *et al.*, 2002) or flow over shallow sills.

These tidal fronts are clearly visible at the sea surface (Figure 1.3). Energetic eddies (Figure 1.4) with diameters of typically 10–150 m are formed in the front by strong horizontal shear. Front and eddies may tilt further downstream due to density differences across the

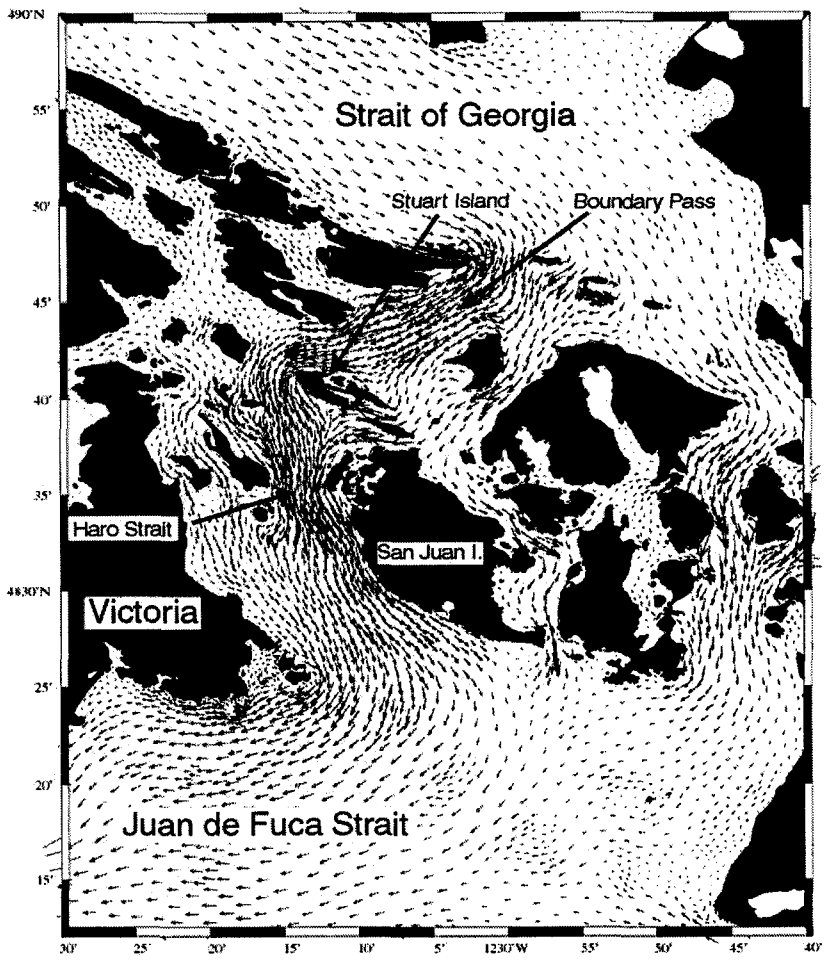

Figure 1.2: *Prediction of the peak ebb tidal flow in Haro Strait on July 1, 1996, from a fully 3-dimensional constant density finite-element frequency-domain model by Foreman & Thomson (1997) (Figure adapted from Farmer* et al. *(2002)).*

front, enhancing the eddy circulation speed and transforming horizontal into vertical mixing (Farmer *et al.*, 2002).

Observations show that in these fronts huge clouds of gas bubbles are drawn into the ocean (Figure 1.5). They can reach depths of up to 160 m (Figure 5.2), which is only slightly deeper than observed by Farmer *et al.* (2002) in Haro Strait, but several times the depth

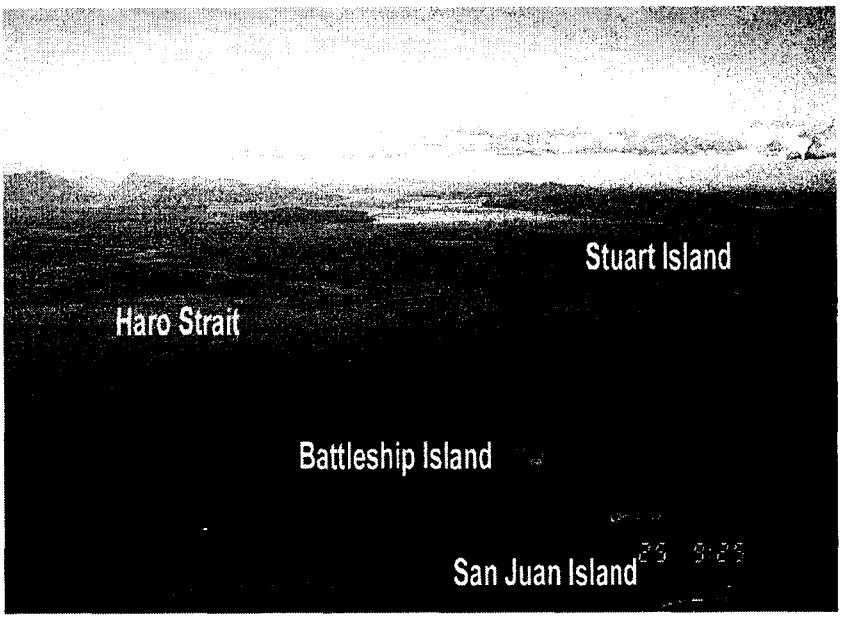

Figure 1.3: *Aerial view of Haro Strait on September 24, 1999, showing tidal fronts (red arrows).*

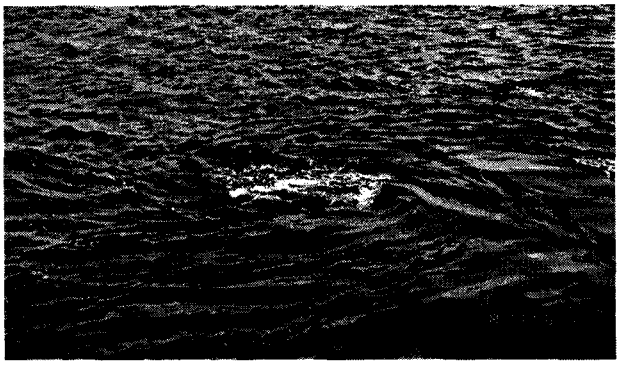

Figure 1.4: *An eddy of approximately 10 m diameter formed in the Stuart Island ebb tidal front. Gas bubbles are visible in the core of the eddy.*

of bubble plumes in the open ocean, where maximal entrainment depths of 15 – 20 m have been measured (Vagle, 1989; Crawford & Farmer, 1987; Wallace & Wirick, 1992). Based on our ship and aerial surveys in Haro Strait (Section 2), it has been assessed that about 9 pronounced fronts develop at ebb tide and 6 at flood tide (Figure 1.6).

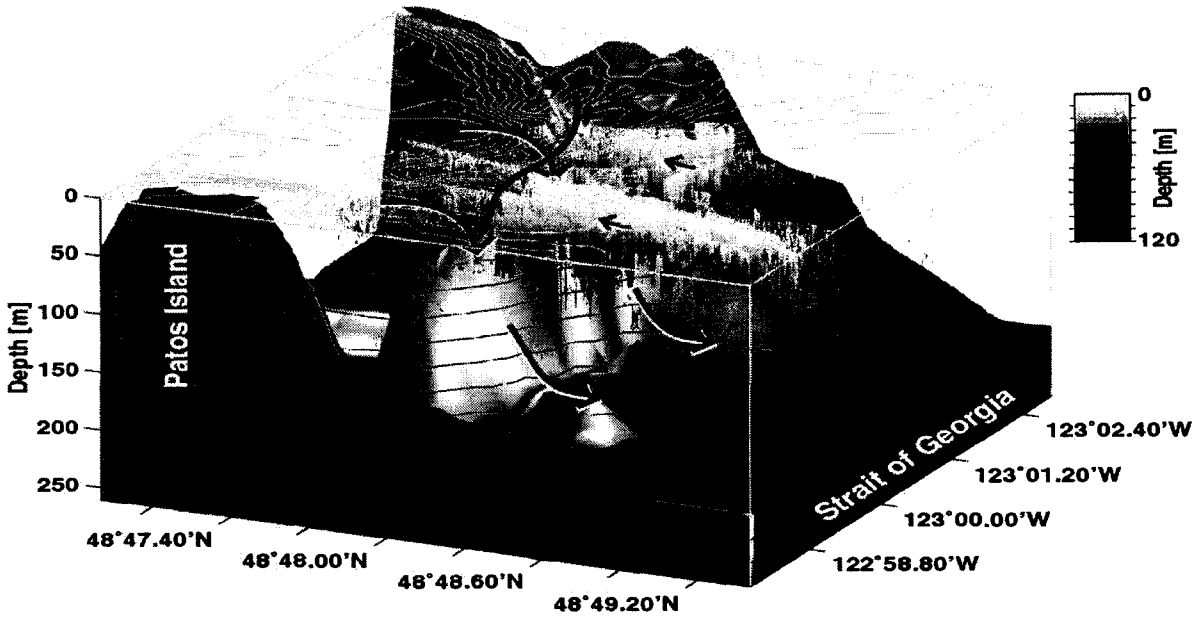

Figure 1.5: *Gas bubble entrainment at Boundary Pass. The colored dots indicate areas of high acoustic backscatter intensity (mostly gas bubbles); the different colors represent depth. The purple line shows the location of the tidal front during strong flood tide and the green arrows the appoximate flow direction.*

This thesis has been motivated by the observations of bubble plumes in tidal fronts suggesting that the processes in the fronts may play an important role in air-sea gas exchange in an estuary. Oxygen is an especially important parameter for marine life and will be studied in more detail. Some of the described processes are also applicable to larger scales in the open ocean where gases like CO_2, a major contributor to global warming, may be more important.

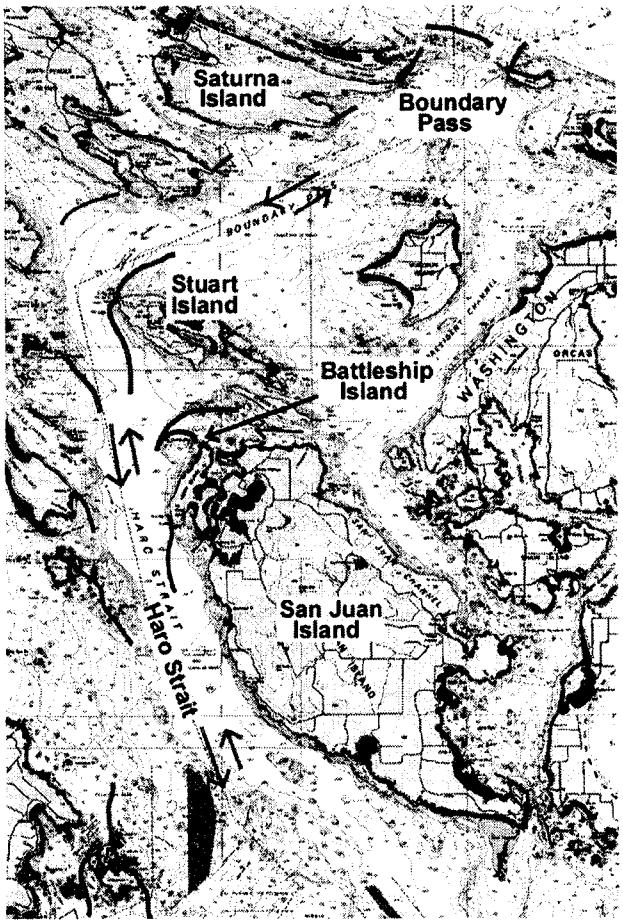

Figure 1.6: *Chart of Haro Strait and Boundary Pass. The red lines and arrows show the approximate locations of the ebb tidal fronts and the flow direction at ebb tide. The green lines and arrows show fronts and currents at flood tide.*

Sill flow at Boundary Pass

The processes at Boundary Pass deserve special attention: the sill controls the renewal and aeration of deep and intermediate water in the Strait of Georgia, as it forms a pronounced barrier for the flow into the Strait, causing intense mixing and hydraulic flow over the sill. But it is also the location of one of the most energetic tidal fronts in the estuary and is therefore important for air-sea gas exchange. The front is generated by the hydraulic sill flow characterized by a strong convergence zone at the sea surface (Figure 1.7). Waves

travelling into the front tend to steepen and break, creating gas bubbles which are then carried down by the currents.

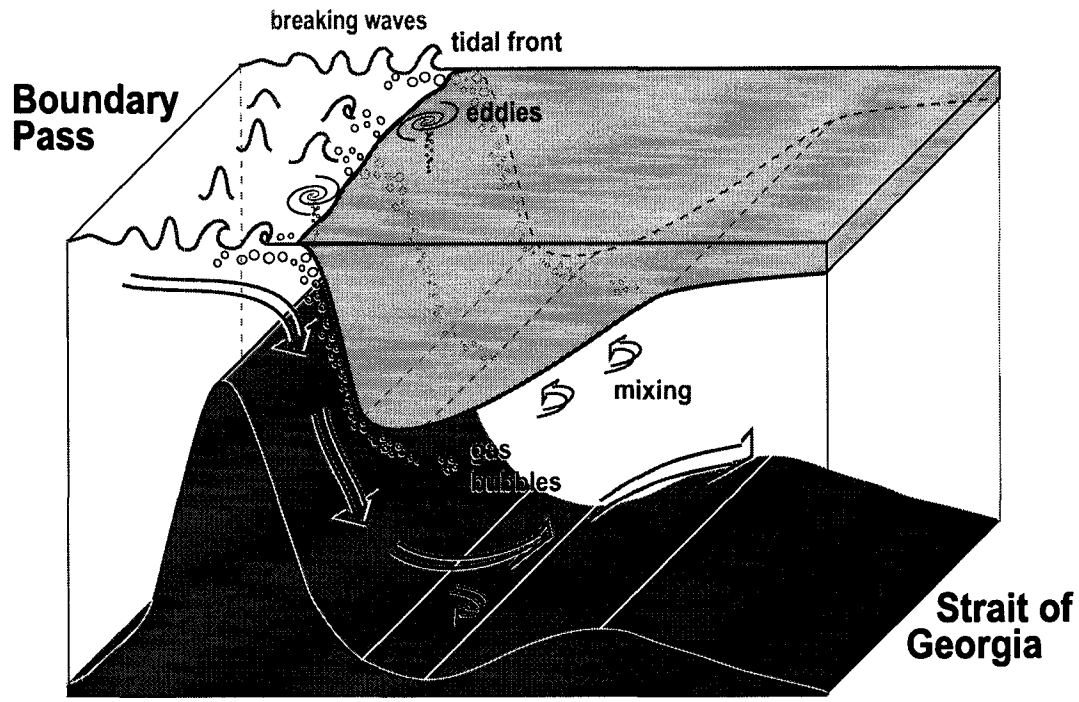

Figure 1.7: *Sketch of the processes important for air-sea gas exchange in the tidal front at Boundary Pass. At the early stage of the flood tide (see also Section 2.2), the hydraulic flow over the sill is characterized by a strong convergence zone at the sea surface causing wave breaking. Bubbles generated by the breaking waves are drawn down by the currents and dissolve.*

At flood tide, the flow over the sill at Boundary Pass can be considered as a two-layer flow with an active lower layer with strong tidal currents of up to $3\,\mathrm{m\,s^{-1}}$ – a situation which is in many respects similar to the one at Knight Inlet, BC, Canada. Armi & Farmer (2002) describe in detail the hydraulic response of the flow during the transition from intermediate to strong and finally (as the tide slackens) moderate forcing (see also Farmer & Armi (1986)).

The observed flow at Boundary Pass at the early stage of the flood tide fits into the category of strong tidal forcing with an arrested upper layer. The plunge point (the tidal front), where the dense lower layer is forced to subduct underneath the fresh surface layer is located downstream of the sill crest; the supercritical flow follows the bottom topography to the bottom of the sill where a hydraulic jump marks the transition to subcritical conditions (Figure 2.5).

Dense water is detrained from the lower layer into the passive, wedge-shaped surface layer. Tank experiments by Pawlak & Armi (1986) show that the volume of detrained fluid depends on the slope of the sill and the distance over which it is detrained.

At even stronger forcing (peak flood tide), the flow at Boundary Pass forms an overshooting jet, which separates at the sill crest. The plunge point is shifted far downstream by the currents and is not marked by a clear front line any more as turbulence and eddy activity seem to be more important.

The hydraulic flow described is connected to air-sea gas exchange processes by setting up a flow convergence zone at the surface (plunge point/tidal front) which favours wave breaking. The breaking waves inject gas bubbles into the ocean, which are then drawn down by the currents and dissolve.

Gas bubbles

Gas bubbles are generated by breaking waves, precipitation, and in supersaturated conditions (Blanchard & Woodcock, 1957). Bubbles have been studied in the open ocean, surf zone, or in tank experiments for various reasons: bubbles can significantly change the optical properties of water (Terrill *et al.*, 1998) as well as the transmission of sound (Deane & Stokes, 1999) – sound speeds as low as $500\,\mathrm{m\,s^{-1}}$ have been observed under breaking waves in the surf zone (Deane, 1999). Farmer & Vagle (1988) and Deane (1997) used the sound radiated by bubbles to identify wave breaking events, and Thorpe (1982), Vagle (1989), as well as Crawford & Farmer (1987) connected the penetration depth of bubbles generated

by white caps with wind speed. It is on the order of $1-2$ wave heights (Hwang *et al.*, 1990; Loewen *et al.*, 1996) and can be increased by the downwelling currents in Langmuir circulations (Thorpe, 1982). Keeling (1993) suggests that bubbles make an important contribution to air-sea gas exchange at wind speeds above $10\,\mathrm{m\,s^{-1}}$, as they can increase gas transfer rates by a factor of up to three (Merlivat & Memery, 1983) and hence also the oxygen content in the surface layer (Wallace & Wirick, 1992).

In tidal fronts, however, gas bubbles are also generated and entrained into the ocean on calm days with very low wind speeds (a process which is greatly enhanced at higher wind speeds though). Tidal fronts are usually characterized by a flow convergence zone at the sea surface. (Small) waves travelling into the convergence zone tend to steepen and break due to wave-current interaction (Bretherton & Garrett, 1969; Phillips, 1977). Gas bubbles which are generated by the breaking waves are carried down by downwelling currents. Vertical velocities are usually in the order of $0.15–0.2\,\mathrm{m\,s^{-1}}$ (Farmer *et al.*, 1995), although observations in Haro Strait (Farmer *et al.*, 2002) and at the sill at Boundary Pass show values as high as $0.5\,\mathrm{m\,s^{-1}}$ and $0.75\,\mathrm{m\,s^{-1}}$ respectively. These strong downwelling currents are responsible for the great bubble entrainment depths observed in the tidal fronts in Haro Strait.

Oxygen supply to the deep and intermediate water in the Strait of Georgia

While oxygen is abundant in the surface layer, it may be a restrictive parameter for marine life in greater depths, especially when oxygen is consumed by the decomposition of organic material. At oxygen levels of less than $2\,\mathrm{ml\,l^{-1}}$ fish cannot survive, but at values of $2-4\,\mathrm{ml\,l^{-1}}$ they are also negatively affected and might move away (The Swedish Environmental Protection Agency, 2003).

Monthly measurements in 1969 by Crean & Ages (1971) show that oxygen levels in the Strait of Georgia below 200 m are always less than $4\,\mathrm{ml\,l^{-1}}$, with minimal values of $< 3\,\mathrm{ml\,l^{-1}}$ in January to April for depths below 250–300 m. However, newer measurements by D. Masson,

IOS, Sidney, Canada (pers. communication; Figure 1.8) show even lower values for summer 2000 close to the critical value of $2\,\mathrm{ml\,l^{-1}}$ at depths below $200-250\,\mathrm{m}$.

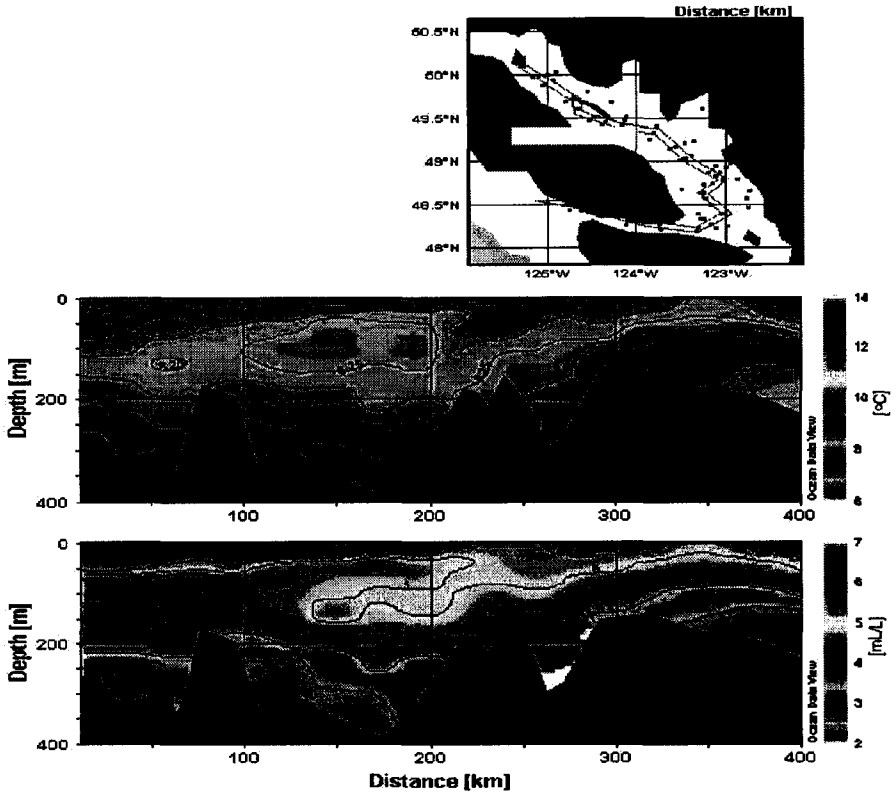

Figure 1.8: *Hydrographic survey in the Fraser Estuary in July 2000 by D. Masson, IOS, Sidney, Canada. a) Chart of the hydrographic stations; b) Temperature section along the Fraser estuary. The Pacific Ocean is to the right, the Strait of Georgia to the left. The sill at Boundary Pass is located at $x=220\,km$. c) Oxygen section.*

In the Strait of Georgia, as in most other estuaries, local formation of (oxygenated) deep water by convection is inhibited by the stratification of the water column. Oxygen in the subsurface water masses is therefore renewed only by advection or by slow diffusion from the surface layer. The Fraser Estuary is characterized by two shallow sills, Victoria Sill and the sill at Boundary Pass, over which the dense water from the Pacific Ocean has to flow

before entering the Strait of Georgia. Both sills are regions of vigorous mixing of this dense water mass with the fresh water of the surface layer and are therefore important for deep water renewal in the Strait as suggested by LeBlond *et al.* (1991) and Masson (2002).

Deep water renewal events are most likely to happen in spring (April) and fall (September/October). Masson (2002) distinguishes intrusions of cold, saline, and oxygen rich water in spring and warm, saline, low oxygen water in fall. During these periods, the upwelling region off the coast of British Columbia brings dense water into Juan de Fuca Strait (Waldichuk, 1957) and the amount of fresh water brought in by the Fraser River is not too large. If also the tidal mixing between these water masses is minimal (at neap tide), the dilution of the dense water is limited, keeping it dense enough to reach the bottom of the Strait of Georgia. LeBlond *et al.* (1991) suggest that renewal events require a current speed of no more than $0.5\,\mathrm{m\,s^{-1}}$ at Boundary Pass.

At spring tide, tidal mixing is stronger in Haro Strait and Boundary Pass. The water flowing into the Strait of Georgia is now too diluted with fresh water to reach the bottom and subducts only to intermediate depths of $150-250\,\mathrm{m}$. However, this water mass carries high concentrations of oxygen (Figure 1.8) as the mixed surface water has had recent contact with the atmosphere. From intermediate depths, the oxygen might be supplied to the deeper parts of the Strait by turbulent diffusion.

Overview

The objectives of this thesis are to understand the physical processes which are important for the generation and entrainment of gas bubbles in tidal fronts and to estimate the contribution of tidal fronts to the air-sea gas exchange in the Fraser Estuary.

The thesis is structured as follows: In Section 2, the research cruises and measurements are described. The (hydraulically controlled) flow over the sill at Boundary Pass will be discussed in Section 3 by using a simple model, based on the Bernoulli equations. Wave-current interaction in a convergence zone as well as the formation of gas bubbles by breaking

waves are the subjects of Section 4. The behaviour of these gas bubbles is then described in Section 5. In Section 6, the models of hydraulically controlled flow, wave-current interaction, and bubble behaviour are combined in order to explain the processes at the flood tidal front at Boundary Pass. The contribution of this and other tidal fronts to the aeration of the Fraser Estuary will then be compared to other oxygen sources in Section 7. It will be finally shown in Section 8 that the physical processes described in this thesis may be also applicable to other areas in the world with strong flow-topography interaction or to open ocean processes like deep convection.

2 Observations

Tidal fronts can be defined as sharp transition zones between two water masses of different density and (tidal) current speed. In the Fraser Estuary, several of these fronts develop due to a pronounced interaction of strong tidal currents in the straits and adjacent channels with the topography. Tidal fronts can be grouped into three main categories, with typical examples at Stuart Island, Battleship Island, and Boundary Pass:

- flow over a shallow sill, i.e. flow-topography interaction at a horizontal boundary (e.g. sill at Boundary Pass, Section 2.2)
- flow separation processes past a headland, i.e. flow-topography interaction at a vertical boundary (e.g. Stuart Island front, Section 2.3.1)
- inflow of dense water from an adjacent channel and plunging flow into intermediate depths (e.g. Battleship Island front, Section 2.3.2)

All these fronts are characterized by converging flow at the surface, which enhances wave breaking and the formation of gas bubbles which are drawn down by the downwelling currents sometimes reaching significant depths ($\sim$ 160 m at Boundary Pass, Section 2.2).

The tidal fronts at Stuart Island, Battleship Island, and Boundary Pass were investigated during CCGS Vector cruises 9934 and 0032 in October 1999 and September 2000. The measurements and instrumentation will be described below in Section 2.1. This thesis, however, will concentrate on the processes at Boundary Pass, while the tidal fronts at Stuart and Battleship Island are only described briefly. In particular, the research objectives to investigate are:

- hydraulical flow over a steep sill and detrainment of water from the active lower layer into the the passive upper layer
- temporal evolution of the tidal front
- wave-current interaction in a convergence zone and bubble formation by wave breaking
- subduction of gas bubbles by downwelling currents/energetic eddies and their contribution to the aeration of water
- contribution of tidal fronts to the aeration of the Fraser estuary

2.1 CCGS Vector cruises 9934 and 0032

The measurements presented in this thesis were mainly collected during two research cruises in Haro Strait and Boundary Pass.

CCGS Vector cruise 9934 was carried out in Haro Strait from October 4 to 14, 1999 and focused on the ebb tidal fronts at Stuart and Battleship Island. During this time, the predicted tidal currents at Turn Point/Boundary Pass reached speeds of up to $0.45\,\mathrm{m\,s^{-1}}$ at flood tide and $1.0\,\mathrm{m\,s^{-1}}$ at ebb tide (Figure B.1). Locally, these currents are much stronger, developing pronounced tidal fronts.

The second research cruise took place from September 18 to 30, 2000 (CCGS Vector cruise 0032). Measurements concentrated on the flood tidal front at Boundary, although additional measurements were carried out at the same stations and transects at Stuart and Battleship Island as during the first cruise (for a list of CTD station see Appendix B.2). During the second cruise, the tidal currents were slightly stronger reaching speeds of up to $0.5\,\mathrm{m\,s^{-1}}$ at flood tide and $1.1\,\mathrm{m\,s^{-1}}$ at ebb tide (Turn Point/Boundary Pass, Figure B.2). Flood tidal currents were of similar amplitude during the whole cruise, which allowed the neglect of spring-neap tidal variations and the comparison of measurements from one day to the next.

Ship-board measurements with a conductivity-temperature-depth recorder (CTD), a

150 kHz vessel-mounted acoustic Doppler current profiler (ADCP), a 100 kHz and a 12 kHz echo sounder, as well as a resonator package for measuring size distributions of gas bubbles provided information about the physical processes in the tidal fronts as well as their importance for the aeration of water.

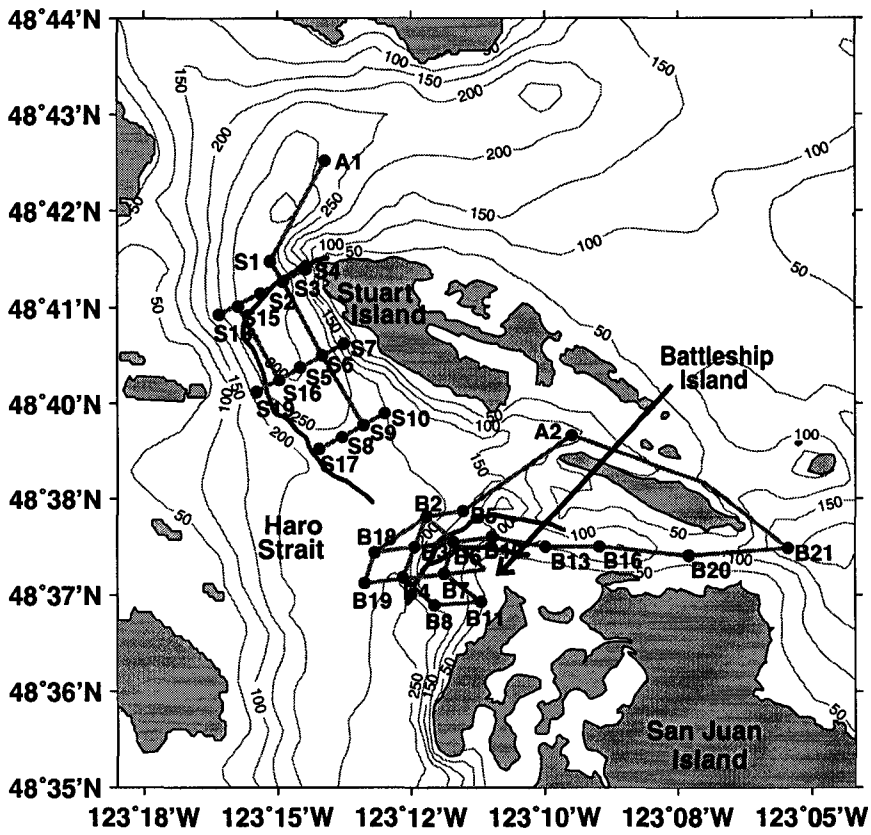

Figure 2.1: *Positions of the CTD-stations (green dots) and the towyos with CTD/resonator package (orange lines) during Vector cruise 9934. The position of the tidal fronts at Stuart Island and Battleship Island during peak ebb tide on October 6, 1999 is shown by the purple lines.*

The instruments were either used on single stations at a given location or on transects through the frontal area. Both single stations and transects were repeated several times over a tidal period to map the temporal evolution of the tidal fronts. Additional measurements

at slack tide were used to map the hydrographic structure in Haro Strait and adjacent channels. Air photos taken from a small plane provided information on the spatial extent of the fronts. Figures 2.1 and 2.2 show the locations of the measurements during both research cruises. The instrumentation was the same on both cruises and will be described in the following in more detail.

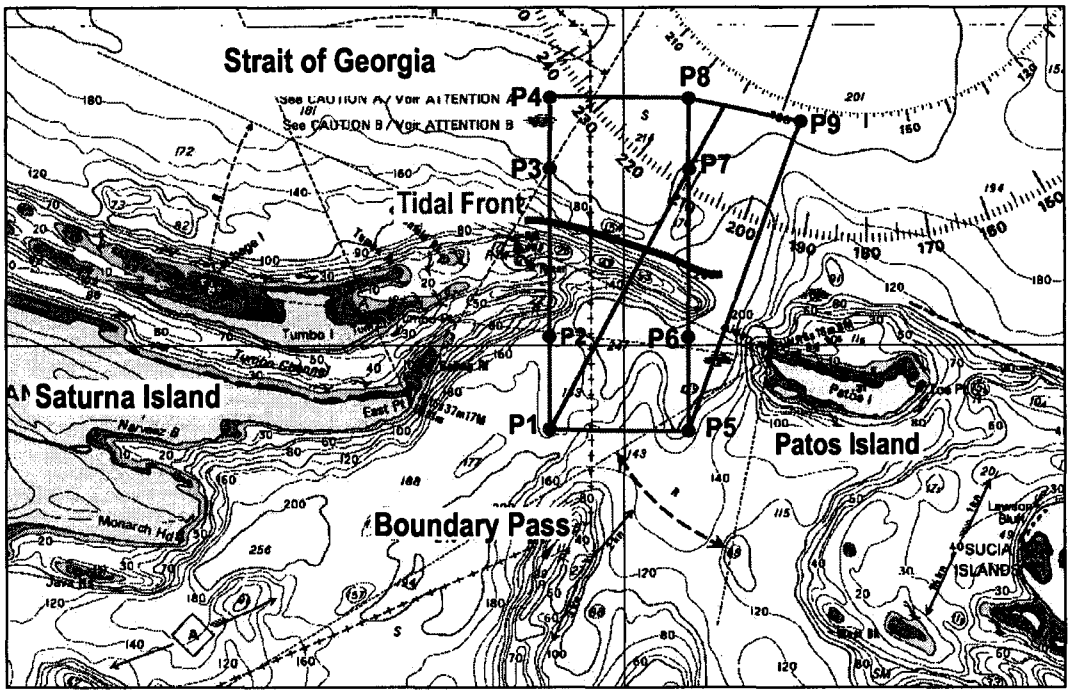

Figure 2.2: *Chart of the sill at Boundary Pass. The purple line shows the approximate location of the flood tidal front. The green dots mark the location of the CTD-stations and the orange lines show the position of the CTD/resonator package-towyos during Vector cruise 0032.*

Additional brief measurements with echo sounder and CTD were carried out on January 14 and 15, 2002 as part of CCGS Vector cruise 0203. The data were collected during flood tide at Boundary Pass.

Global Positioning System

A differential GPS-receiver (Global Positioning System) was used to determine the time and ship's position during the measurements. The data were recorded in 10 s-intervals and the accuracy was generally better than 10 m.

In addition, the locations of the tidal fronts at Battleship and Stuart Island were mapped with a small boat (Zodiac) by driving along the front lines. Also here, the position was determined with a differential GPS with recording intervals of 1 s. Due to the high speed of the Zodiac these measurements provided a quasi-synoptic picture of the location of the tidal front.

Acoustic Doppler current profiler

For measuring the current speed, a 4 beam 150 kHz vessel-mounted broadband acoustic Doppler current profiler (ADCP) from RDI with a bandwidth of 39 kHz and a beam angle of 20° was used.

The instrument was mounted on a strut on the starboard side of the boat allowing for a cruising speed of up to 6 kt. Measurements were therefore only taken in the frontal zones. The strut was taken out of the water for longer transits in order to increase the ship's speed.

The transducer depth was about 1 m. The ADCP was oriented with transducer # 3 to the front, so that beams #3 and #4 were located in a plane parallel to the ship and beams #1 and #2 in a plane orthogonal to it.

The ADCP uses two kinds of pulses: a short 6 ms pulse repeated three times for measuring the current speed and backscatter intensity and a single long 79 ms pulse for bottom tracking. Bottom tracking was used to convert the currents from ship-coordinates into earth-coordinates allowing for a direct correction of the alignment angle of the ADCP and of Schuler oscillations of the gyro compass due to North-South accelerations of the ship. The ship's position was provided by the differential GPS-receiver of the Vector and the

ship's heading was determined with a flux gate compass which was mounted on the upper deck. The compass was calibrated at the beginning of the cruise by running the vessel twice in a tight circle. With a bin size of 4 m, the ADCP measures the upper 200 – 300 m of the water column, which is close to the maximum water depth in the area of investigation. The data were collected at a rate of one ping per second. Data acquisition and processing was carried out with the software package *Transect* from *RDI*. Bad bins and profiles were edited and the data were averaged to 10 s-ensembles.

The calculation of the current speed is based on the assumption of horizontal homogeneity. However, due to the high horizontal gradients in the flow field of the tidal fronts, it can be questioned if this assumption is valid. In a depth of 100 m, the beams of the ADCP spread horizontally over a distance of 73 m (at an beam angle of 20°). Over this distance, significant horizontal changes of the flow field can be observed (Figure 3.2). However, in Appendix B.3 it is shown that the usual 4-beam solution for deriving the current speed can provide useful results in tidal fronts.

CTD

A Seabird CTD system (model SBE 19-03) was used to measure the hydrographic structure of the water. The CTD carried a Paine strain-gauge pressure sensor, a pressure-protected thermistor, and a Pyrex conductivity cell (for sensor accuracy and resolution see Table 2.1).

Sensor	Accuracy	Resolution
Pressure	1.25 dbar	0.75 dbar
Temperature	0.01°C	0.001°C
Conductivity	1 mS m^{-1}	0.1 mS m^{-1}

Table 2.1: *Sensor accuracy and resolution of the Seabird CTD SBE 19-03.*

The CTD was calibrated prior to the cruises and additional salinity samples were taken from

different depths (water masses) to recalibrate it after the cruises. The data were directly transferred to a computer via cable and then processed with the software package *Seasoft 4.2* from Seabird Electronics.

The CTD was attached to a wire on the A-frame of the ship and was used in two different modes. One mode consisted of single stations at a given location with casts reaching to the bottom (for a list of CTD stations see Appendix B.2). These measurements were carried out before and after the strongest ebb and flood tide in order to measure the changes of the hydrographic structure in the frontal area and surrounding waters.

In the other mode, the CTD was used for continously repeated rapid up- and down casts while the ship was moving along a transect ("CTD-towyo"). The towyos were used in the frontal region with the ship slowly moving in the direction of the tidal currents so that the ship's speed over ground was significant while the wire angle of the CTD, which is determined by the speed through the water, could be minimized. Usually, the instrument was lowered to a depth of 15 m above the bottom, although the tidal conditions made it sometimes impossible to avoid a big wire angle so that the instrument could not be lowered far enough.

Echo sounder

The acoustic backscatter intensity of the water column was measured with two echo sounders with a frequency of 12 kHz and 100 kHz. The transducers were mounted in the hull of the *Vector* at a depth of about 2 m. A board unit from *Biosonics* was used to set pulse width, sample frequency, ping interval, etc. (Table 2.2). The data were acquired with the program *Sounder* of the IOS Ocean Acoustics group and processed with *Matlab*.

The echo sounder images show areas of different backscatter intensity. High backscatter intensity indicates the sea floor as well as gas bubbles, turbulence, zooplankton aggregations, or fish.

However, because the acoustical cross section of a bubble is about 1000 times the geometrical

Parameter	Cruise 9934	Cruise 0032
Transmitter pulse width	0.5 (0.3) s	0.2 s
Receiver gain	18 (12) dB	24 dB
Receiver band width	5 (10) kHz	5 kHz
Sample frequency	12 kHz	12 kHz
Pulse width	0.3 s	0.2 s
Ping interval	0.5 s	0.7 s
Trigger interval	0.5 s	0.5 s

Table 2.2: *Settings of the 100 kHz echo sounder during Vector cruises 9934 and 0032. The values in brackets show the settings for the first two days of cruise 9934.*

one (Medwin, 1977*b*) and independent measurements with an acoustical resonator showed that gas bubbles are present in the downwelling regions of tidal fronts, it can be assumed that the high backscatter intensity is mainly due to gas bubbles and not zooplankton or turbulence.

Acoustical resonator

An acoustical resonator was used for measuring bubble size distributions in the tidal fronts. The instrument consists of two identical steel plates with a thickness of 1.27 cm and a diameter of 26.5 cm, which are mounted at a distance of 15.0 cm from each other (Figure 2.3). The steel plates are covered with a layer of piezoelectric polyvinylidenedifluoride (PVDF) and a ρc-compound (Farmer *et al.*, 1998). One of the plates produces broadband noise setting up 37 resonant modes in the resonant cavity between the plates. The other plate is used as a hydrophone, which detects these modes as well as the damping (attenuation) by gas bubbles. The frequency range of $6-196$ kHz allows it to detect gas bubbles with radii of $15-550\,\mu$m.

The resonator was mounted on a frame which also held the battery case, the recording unit, and a CTD (Figure 2.4). During Vector cruise 9934, this resonator package was equipped

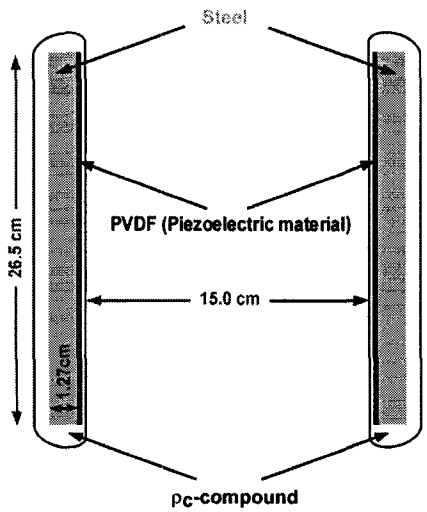

Figure 2.3: *Design of the acoustical resonator. One of the identical plates is used for transmission – the other one for detection.*

Figure 2.4: *The resonator package during Vector cruise 9934. The resonator plates are located at the lower right hand side.*

with an additional *Sensortec* acoustic current meter (model UCM 40 Mk II) and during cruise 0032 with a *Seabird* dissolved oxygen sensor (model 23-01-Y). However, the data from the current meter was not used due to a broken tilt sensor.

The resonator package was attached to a wire at the A-frame of the Vector. Measurements were taken while it was continuously profiling up and down in the upper 60 m of the water column – either along a transect through the frontal region or while the boat was sitting (more or less stationary) in the tidal front.

The distance between the resonator and the hull-mounted echo sounder (sometimes > 50 m) has to be taken into account when the measurements are compared with each other. The measured bubble size distributions in the upper 10 m were not used as they might be "contaminated" with bubbles of the ship's wake.

The data were acquired and processed with a software package from the IOS Ocean Acoustics group.

Aerial photography

A week before Vector cruise 9934 (on September 24) as well as during Vector cruise 0032, air photos were taken with a 35 mm photo camera from a small plane to provide additional information on the surface signals (front lines, eddies, waves) of the tidal fronts. This information was used to estimate the spatial extent of the tidal fronts in the region.

2.2 The tidal front at Boundary Pass

Between Saturna and Patos Island (Figure 2.2), a steep sill forms a pronounced barrier for the water exchange between Boundary Pass and the Strait of Georgia. It rises from 200 m to 60 m depth and blocks about 80% of the width of passage, which is also about 200 m deep. The mean slope of the sill is about 30°.

Measurements at Boundary Pass were carried out in September 2000 during Vector cruise 0032 and also briefly in January 2002 during Vector cruise 0203. In the following, the observations from cruise 0032 are described and are then compared to the ones from cruise 0203 to get an idea of the seasonal variations of the observed processes.

The times which are given in this section in order to describe the temporal evolution of the frontal system are relative to the preceding low tide at Fulford Harbour (Saltspring Island). Slack tide at Boundary Pass is about 1.5 h later.

The strong flood tidal flow in Boundary Pass can reach current speeds of up to $3\,\mathrm{m\,s^{-1}}$. It forces dense water from Boundary Pass over the sill (and partly through the gap at the eastern side of the passage) into the Strait of Georgia. This water mass meets a fresher surface layer in the Strait of Georgia just downstream of the sill crest (Figures 1.7, 2.5) and subducts underneath it due to the density difference between the two water masses (about $2\sigma_\theta$-units in September 2000).

In the early stage of the flood tide, this sets up a two-layer hydraulic flow along the slope of

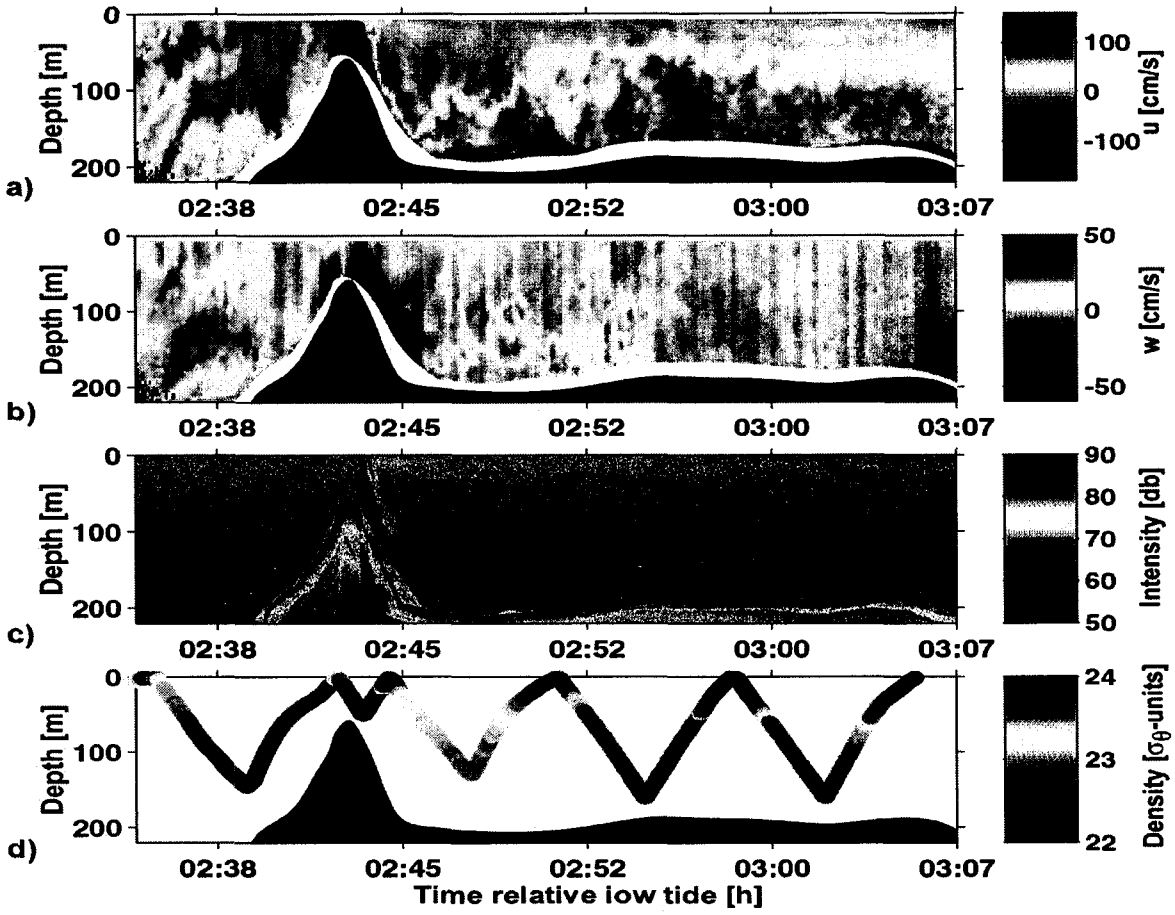

Figure 2.5: *Along-strait transect over the sill at Boundary Pass at the beginning of the flood tidal period on September 29, 2000 (for an enlarged picture of the flow at the sill see Figure 3.2). Measurements were taken with ADCP, echo sounder, and towed CTD. The time is given relative to Fulford Harbour, Saltspring Island. a) North-south (along-strait) component of current speed; b) vertical current speed; c) acoustic backscatter intensity; d) density.*

the sill while at a later stage flow separation at the sill crest can be observed (next Section). At the surface, where the two water masses meet, a distinct tidal front line forms and eddies are generated by the horizontal shear. Waves, which travel into this convergence zone tend to steepen and break (Section 4) creating gas bubbles in the surface layer (Figure 1.7).

The bubbles are drawn down by the strong vertical currents of up to $0.75\,\mathrm{m\,s^{-1}}$ to depths $> 160\,\mathrm{m}$ (Figure 5.2). These current speeds are higher than the rise speed of gas bubbles, which is even for the bigger bubbles only in the order of $15-30\,\mathrm{cm\,s^{-1}}$ (Figure 5.1). This means that all gas bubbles, which are trapped in the downwelling currents are drawn into the ocean where they completely dissolve.

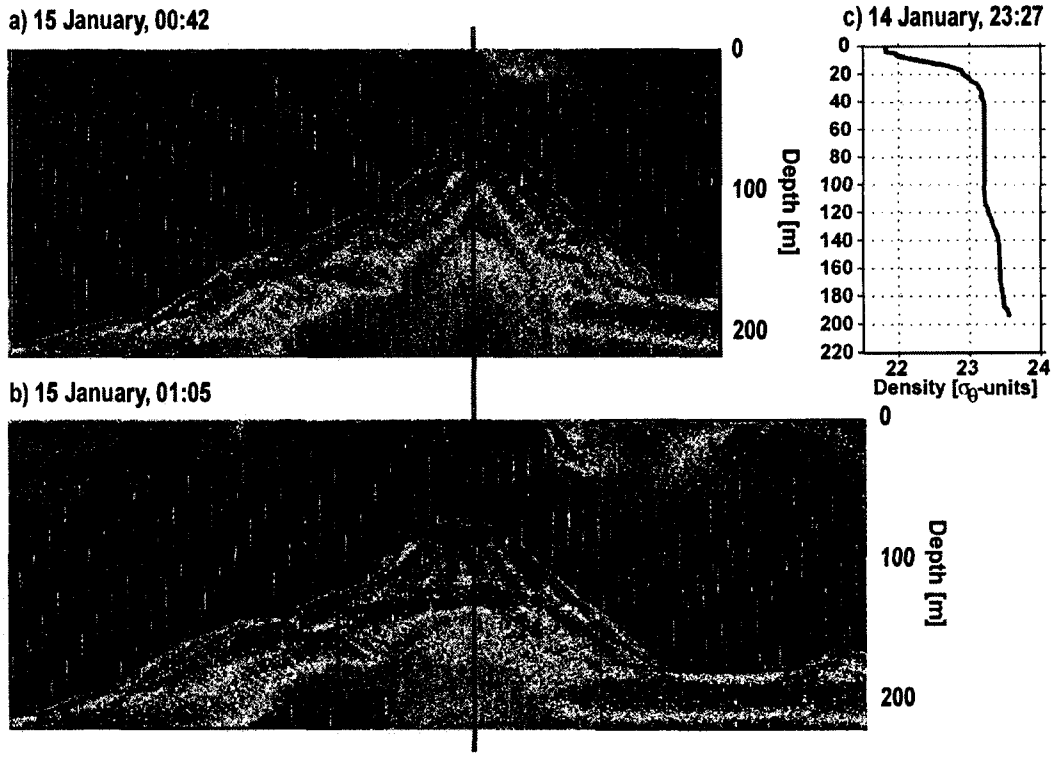

Figure 2.6: *Flood tidal front at Boundary Pass during Vector cruise 0203 in January 2002. a) Echo sounder image 1 h 10 min after low tide (relative to Fulford Harbour); b) echo sounder image 1 h 33 min after low tide; c) density-profile downstream of the sill, 5 min before low tide.*

Measurements taken in January 2002 during Vector cruise 0203, show a frontal system at Boundary Pass which is very similar to the one in September 2000. Echo sounder images (Figure 2.6a-b) indicate hydraulically controlled flow over the sill at about 1 h after low tide

(relative to Fulford Harbour). However, the initial stratification and thickness of the upper layer at low tide was weaker than in fall 2000 (about 1.2 σ_θ-units, Figure 2.6c) and the upper layer of fresh water from the Fraser River much shallower (about 30 m), which also resulted in shallower bubble penetration depths and fewer bubbles. The importance of the tidal front at Boundary Pass to the aeration of the estuary may therefore be less in times of weaker stratification (less discharge from the Fraser River in winter and early spring), but even then some gas bubbles are entrained into the ocean.

Temporal evolution of tidal front

The location and extent of the tidal front at Boundary Pass changes significantly over a flood tidal period, which is also associated with changes in current speed, stratification, and bubble entrainment.

Averaged ADCP measurements from September 2000 (Figure 2.7) show that within the first 1.5–2 h after low tide, the flow in the Strait of Georgia is mainly parallel to the sill and in eastward direction. With increasing flood tidal flow ($\sim$ 2–4 h after low tide), the currents are directed from Boundary Pass into the Strait of Georgia. The currents are now strong enough to flow over the sill (see also Appendix B.4) – this is the scenario which is described in the previous Section (Figures 1.7 and 2.5). The convergence zone at the surface (tidal front) is about 50 m wide. It stretches from the south-eastern tip of Saturna Island to the end of the sill close to Patos Island (Figure 2.2). The interface between upper and lower layer is clearly visible by high concentrations of gas bubbles – the tidal front is the only region where gas bubbles are drawn into the ocean.

Vertical current speeds in the lower layer reach up to 0.75 m s^{-1} (Figure 2.5), which is in the same order of magnitude as the horizontal currents. Between the frontal location and the end of the sill slope, the lower layer loses about 60% of its volume by detrainment to the upper layer (Section 3). Also further downstream in a hydraulic jump, intense mixing reduces the density difference between the two layers. This seems to be important for the

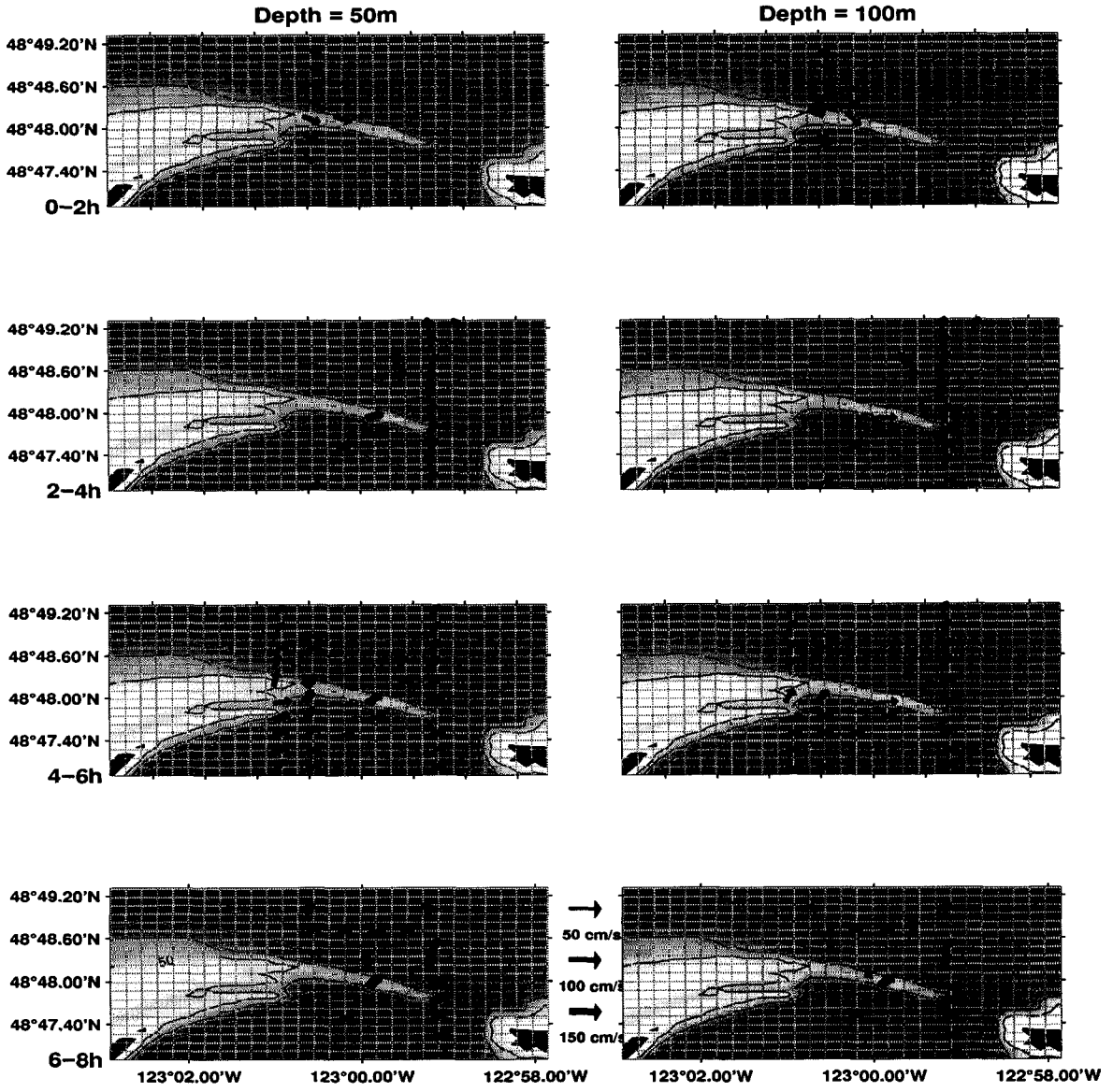

Figure 2.7: *Average horizontal currents during flood tide at Boundary Pass in September 2000 for a depth of 50 m and 100 m and for time intervals 0 – 2 h, 2 – 4 h, 4 – 6 h, and 6 – 8 h. The thickness of the arrows represents the current speed. The water depth is shown in blue, with darker colors representing greater depth. The islands in the lower left and right hand corners are Saturna and Patos Island.*

transition to the next stage in the evolution of the front.

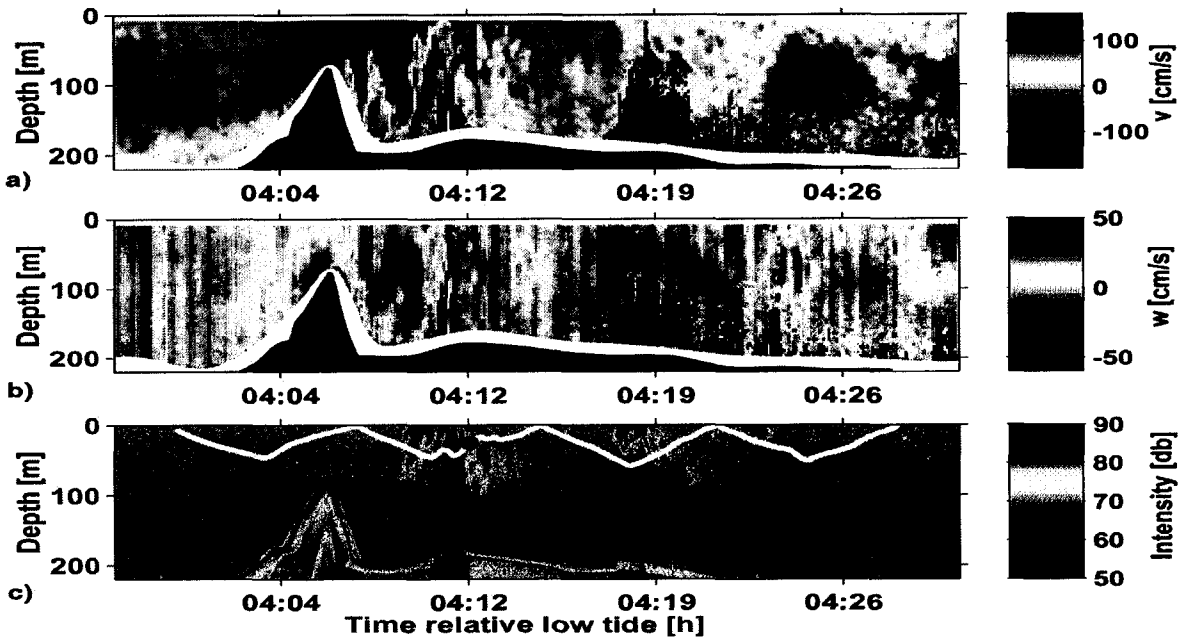

Figure 2.8: *Transect over the sill at Boundary Pass at the later stage of the flood tide measured with ADCP, echo sounder, and towed resonator package on September 29, 2000. a) Along-strait current; b) vertical current; c) acoustic backscatter intensity. The path of the resonator is shown by the white line and the location of the bubble measurements in Figure 7.1 is marked by the black dot.*

At about 4 – 6 h after low tide, the flow is at its peak and separates from the sill crest (Figures 2.8, 2.9). Some of the lower layer water shoots up to the surface, where rings of upwelling water can be observed. The tidal front is shifted further downstream, and is not as well defined anymore. It stretches over a width of about 1000 m with intense wave breaking, eddies, convergence zones, but also upwelling. Consequently, the echo sounder images (Figures 2.8, 5.2) show extended regions of bubble entrainment. Therefore, the contribution to the aeration of water is still significant, even though the vertical currents are much weaker now.

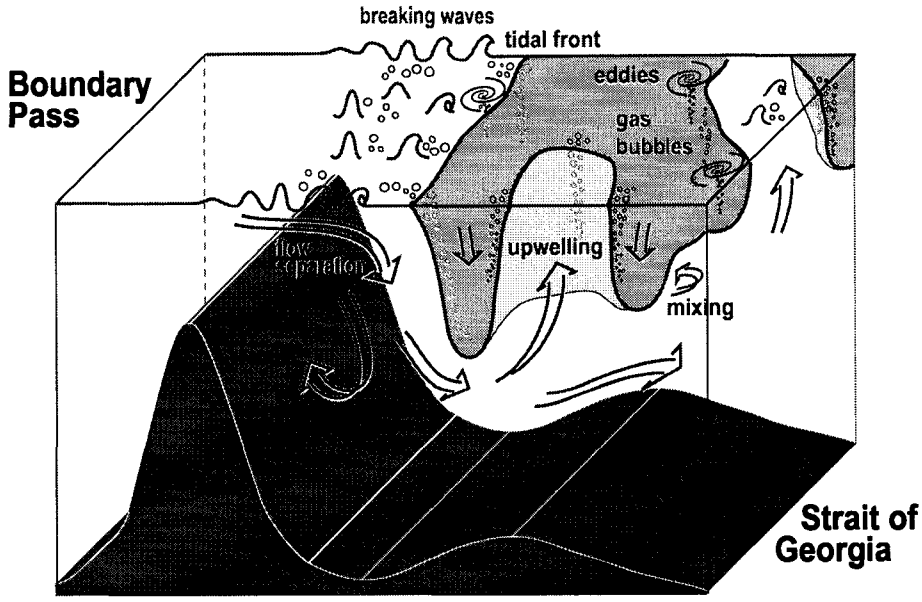

Figure 2.9: *Sketch of the later stage of the tidal front at Boundary Pass (about 4 – 6 h after low tide). For explanations see text.*

Finally, the tide slackens with varying current directions (6 – 8 h after low tide; Figure 2.7, lower row) and air entrainment decreases again.

2.3 The tidal fronts in Haro Strait

2.3.1 Stuart Island

Flow separation processes are responsible for the formation of the tidal front at Stuart Island (Figure 1.6). At ebb tide, strong tidal currents push water from Boundary Pass into Haro Strait. At Turn Point, the northern tip of the island, the flow separates from the shore forming a pronounced tidal front which extends into Haro Strait over several kilometers (Figure 1.3). A back eddy forms between the front and the island, with water moving slowly in the opposite direction (to the North).

As described by Farmer *et al.* (2002), this front is initially vertical but tilts with time

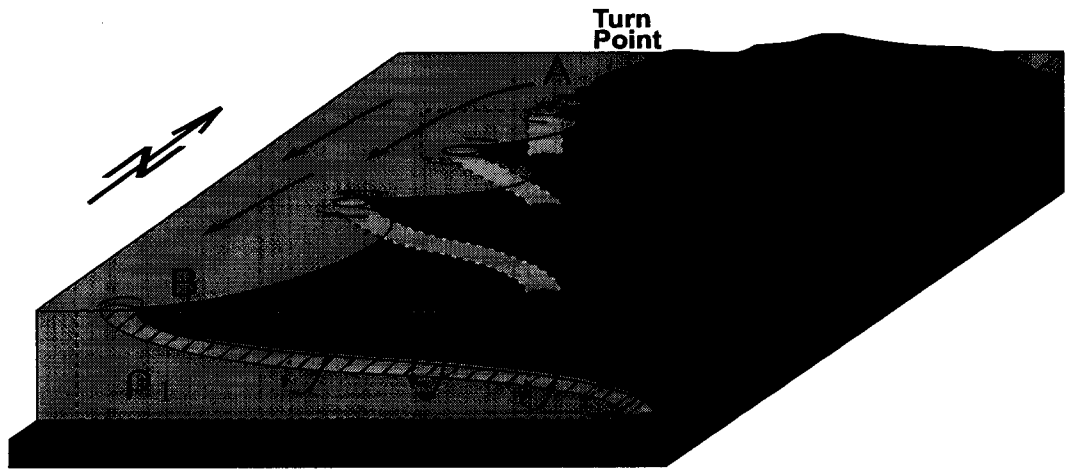

Figure 2.10: *Sketch of the Stuart Island front. The front is initially vertical (Transect A, Figure 2.11), but tilts and stretches with time (Transect B) due to effects of the density gradient across the front (Figure adapted from Farmer* et al. *(2002).*

(further downstream) due to the effect of the density gradient across the front (Figures 2.10, 2.11). The authors suggest that the eddies, which are generated in the frontal zone by the high horizontal shear, are stretched and tilted by the restratification processes. Vortex

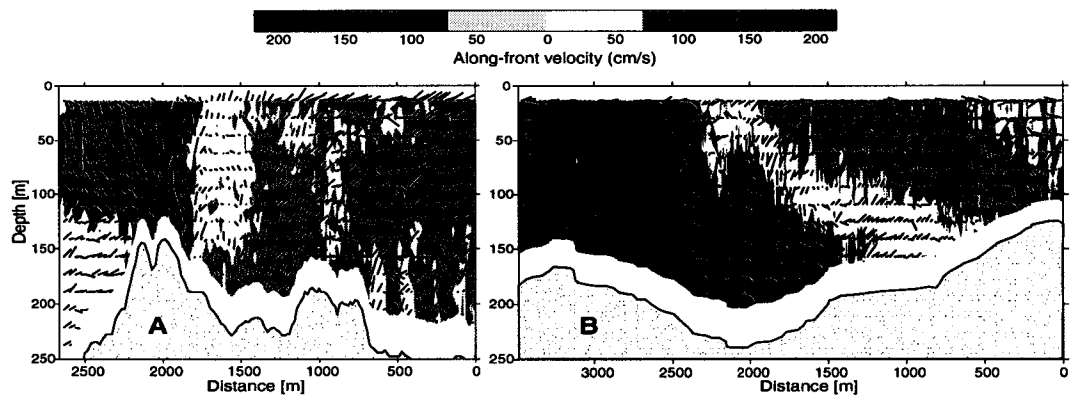

Figure 2.11: *Currents at the Stuart Island front. Colors indicate the along-front current speed and the arrows the currents along the transect (Figure adapted from Farmer et al, 2002). For the location of transects A and B see Figure 2.10.*

stretching increases the circulation speed while vortex tilting transforms horizontal into vertical circulation enhancing the vertical mixing rate.

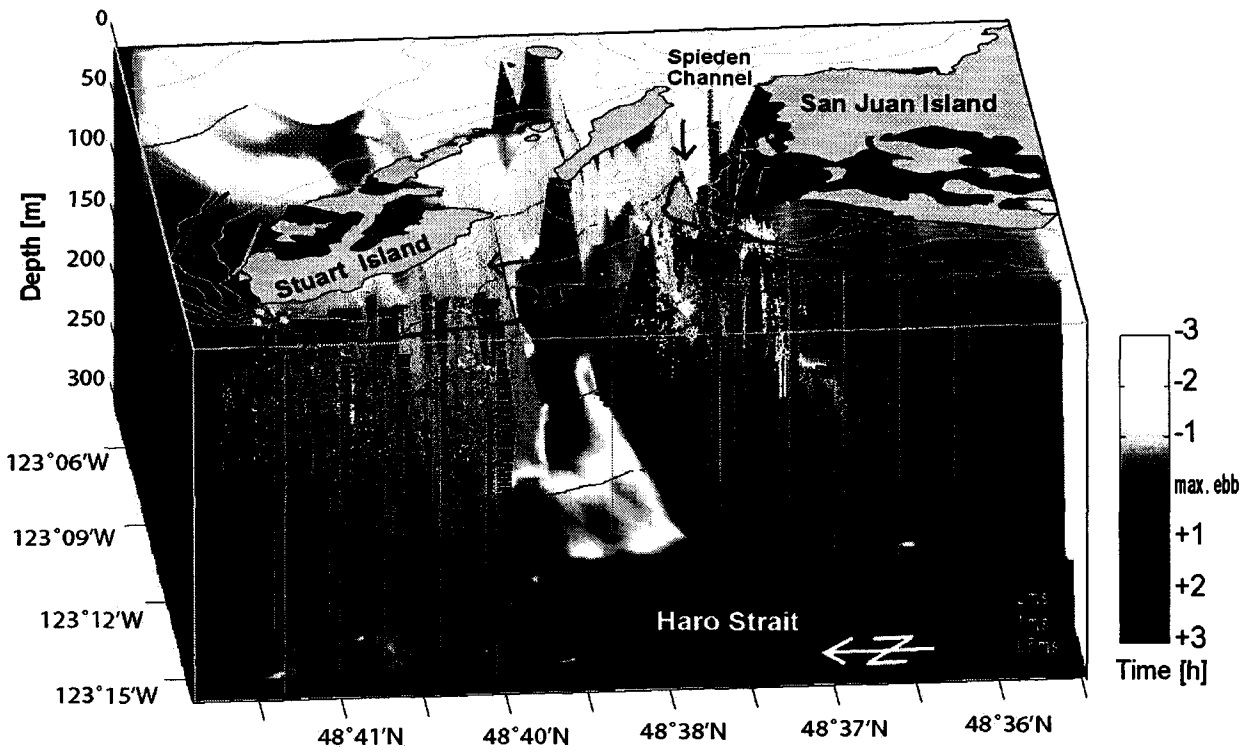

Figure 2.12: *Measurements in Haro Strait. The purple lines show the location of the tidal fronts at Stuart and Battleship Island during strong ebb tide. The colored dots indicate high acoustic backscatter intensity (mostly gas bubbles). The different colors represent the time of measurement relative to the max. ebb current. The green arrows show the mean ebb tidal current.*

The Stuart Island tidal front also forms a convergence zone at the surface with downwelling currents in the frontal zone. Gas bubbles which are created by breaking waves in that region due to wave-current interaction are drawn down by the currents as well as by the energetic eddies formed in the shear zone of the front.

A situation similar to the one described by Farmer *et al.* (2002) was observed in October 1999; the measurements during cruise 9934 are summarized in Figure 2.12. The location of the front lines was mapped with a small boat (Zodiac) and is also indicated by the gas bubbles which are drawn down by the currents to a depth of up to 120 m (backscatter intensity from an echo sounder; colored dots). Current measurements with an ADCP show southward flow in Haro Strait and northward flow in the back eddy at peak ebb flow. However, it has to be noted that the measurements were taken on different days of the cruise and that they may therefore not completely match with each other due to spring-neap tidal variations.

In September 2000, the general situation was the same as in fall 1999. However, the stratification in Haro Strait was weaker resulting in a less distinct front line and a shallower surface layer in the back eddy. Also bubble penetration depths were reduced and were only in the order of 30 m.

2.3.2 Battleship Island

Another pronounced ebb tidal front is located only a few kilometers to the South of Stuart Island close to Battleship Island (Figures 1.6). Measurements there were carried out during Vector cruise 9934 – at a time with strong stratification in the Fraser Estuary.

Two tidal fronts are formed by the strong ebb tidal flow entering Haro from Spieden Channel. Surface signals (Figure 2.13) as well as ADCP/CTD transects through the fronts (Figure 2.14) suggest that the water from Spieden Channel subducts at the meeting point of the two front lines under the water in Haro Strait. Due to its greater density (in October 1999 about $2\sigma_\theta$-units, Figure 2.14d) it sinks into intermediate depths of $50-150$ m. It then spreads and mixes with the water mass in Haro Strait as indicated in the sketch in Figure 2.15.

The front forms a convergence zone at the surface which enhances wave breaking and the generation of gas bubbles. The bubbles are then drawn down by eddies and strong vertical

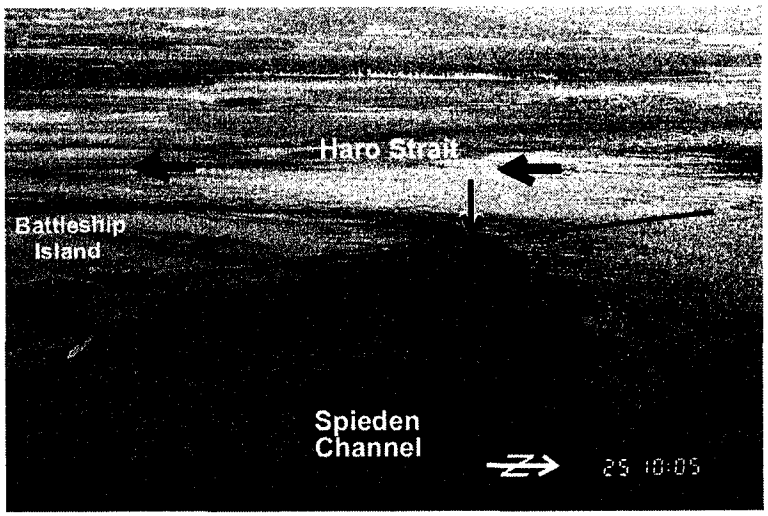

Figure 2.13: *Aerial view of the tidal front at Battleship Island, Haro Strait. The green arrows indicate the flow direction. The red line and purple arrow mark the transect and frontal location shown in Figure 2.14*

currents of up to $0.5\,\mathrm{m\,s^{-1}}$ (Figure 2.14b) to depths of more than 120 m.

It is likely that this front is not as strongly developed all year-round as the density difference between the water in Haro Strait and Spieden Channel, which is influenced by the fresh water discharge of the Fraser River, is critical for the formation of the front. This possible seasonality of the tidal fronts in the Haro Strait region was also indicated by observations in September 2000 when the overall stratification in the Fraser Estuary was less than in the preceding year and the tidal fronts were not as well defined as in October 1999. Gas bubble clouds only reached depths of the order of 20−30 m.

2.3.3 Other tidal fronts

In addition to the tidal fronts at Stuart and Battleship Island as well as Boundary Pass, several other tidal fronts form in Haro Strait at ebb and flood tide. Their approximate locations and extent were estimated from pictures or observations taken from the air, boat, or shore and are shown in Figure 1.6. Measurements were also carried out during Vector

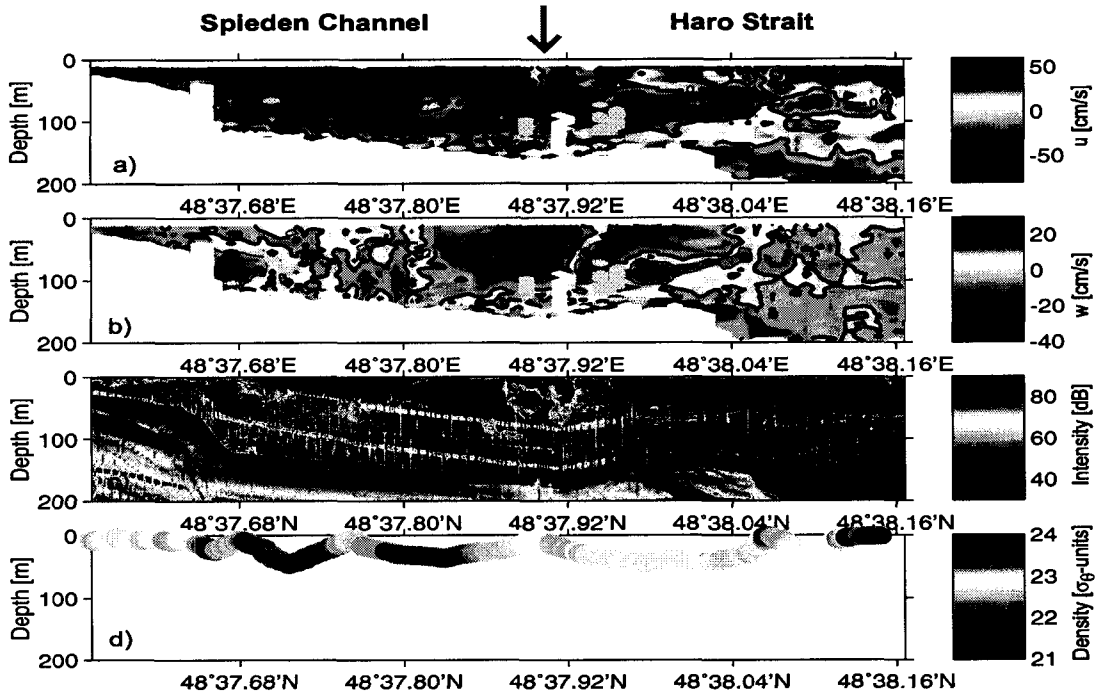

Figure 2.14: *Cross section through the tidal front at Battleship Island (Figures 2.13, 2.15) measured with ADCP, echo sounder, and towed CTD. The location of the tidal front is marked by the purple arrow. a) Along-strait current, b) vertical current, c) acoustic backscatter intensity, d) density.*

cruise 0032 at the flood tidal front at Stuart Island.

In general, the ebb tidal fronts are more pronounced than the flood tidal fronts, which can be explained by the higher current speeds at ebb tide and the fact that the stratification is increased by fresh water brought into Haro Strait by the ebb tidal currents.

All tidal fronts in the Strait can be grouped in one of the three categories mentioned at the beginning of Section 2. However, flow separation at a vertical boundary as at the Stuart Island front seems to be the predominant one.

The location, extent, and temporal evolution of these fronts have to be known in order to estimate their contribution to the aeration of the estuary. A parcel of water moving from

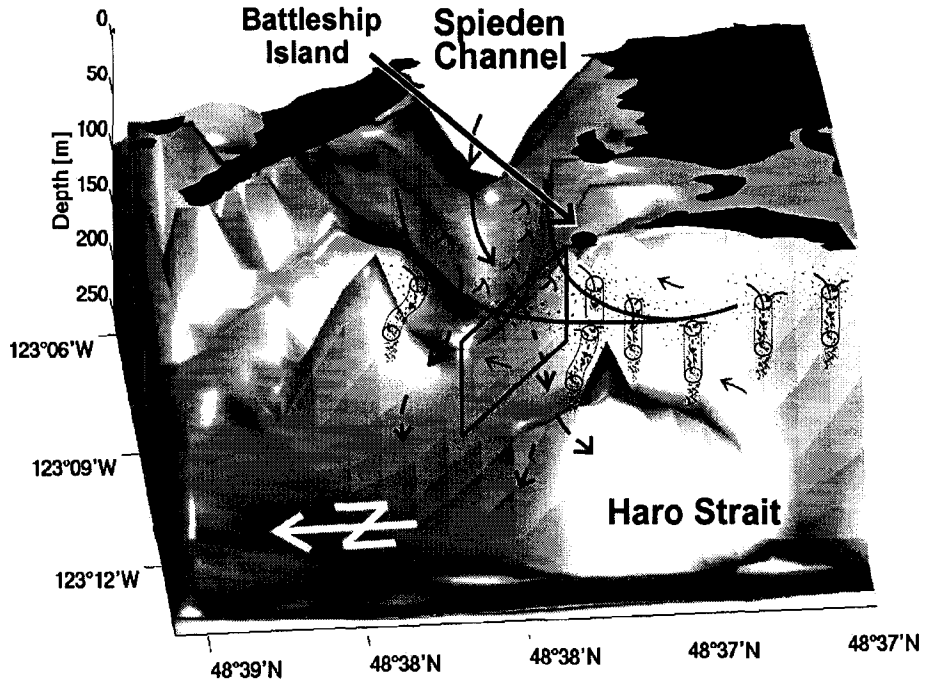

Figure 2.15: *Sketch of the tidal front at Battleship Island. Note that it is oriented the opposite way as Figure 2.13 with North to the left. The purple lines indicate the location of the tidal fronts, the green arrows the direction of flow, and the orange dots locations of gas bubble entrainment by eddies and subducting flow. The red line marks the section across the tidal fronts shown in Figure 2.14.*

Juan de Fuca Strait into the Strait of Georgia will be in contact with several of these fronts – sometimes even more than once, due to the changing flow direction of the tidal currents (Section 7.1). It is estimated that there are about 9 ebb and 7 flood tidal fronts in Haro Strait and Boundary Pass (Figure 1.6).

Hence, the water which is moving towards the Strait of Georgia is aerated by gas bubbles subducted in the tidal fronts (as well as by other mechanisms, like diffusion). The last front it passes is the one at Boundary Pass. But there, not only the entrainment of bubbles is of importance for the aeration of the water in the Strait of Georgia – the dynamics of the

flow itself plays an important role in determining the depth at which the oxygenated water spreads into the Strait. It will therefore be studied in the next chapter in more detail.

3 Model of hydraulic sill flow

The renewal of aerated intermediate water in the Strait of Georgia is greatly influenced by flow over the sill at Boundary Pass, which is located at the entrance of the Strait (Section 2.2). At flood tide, dense water from the Pacific Ocean mixes with fresh surface water upstream of the sill. The newly formed water mass flows over the sill crest and plunges – at the early stage of the flood tide – down to intermediate depths (Figure 1.7). The final depth of this water mass is determined by its density and the stratification downstream of the sill, while the dynamics of the flow are determined by the density difference between the newly formed water mass and the fresh surface layer downstream of the sill as well as the forcing of the flow (tidal currents).

In this Section, the dynamics of the sill flow will be studied with a model based on the Bernoulli equation (Farmer & Armi, 1999). The initial conditions of the model are in agreement with the observations during CCGS Vector cruise 0032 in September 2000 (see also Section 2).

According to the classification by Farmer & Armi (1986), the early stage of the flood tidal sill flow at Boundary Pass can be categorized as strong barotropic flow with an arrested upper layer of light water. The authors describe the transition from weak to intermediate and strong forcing (Figure 3.1): first, a hydraulically controlled 2-layer flow is established, which exchanges water between the reservoirs on both sides of the sill – a situation found in many fjords or sea straits like the Strait of Gibraltar.
When the tidal forcing increases, the upper layer is arrested (Figure 3.1). The plunge point of the lower layer is located upstream of the sill crest and the flow is controlled at the crest,

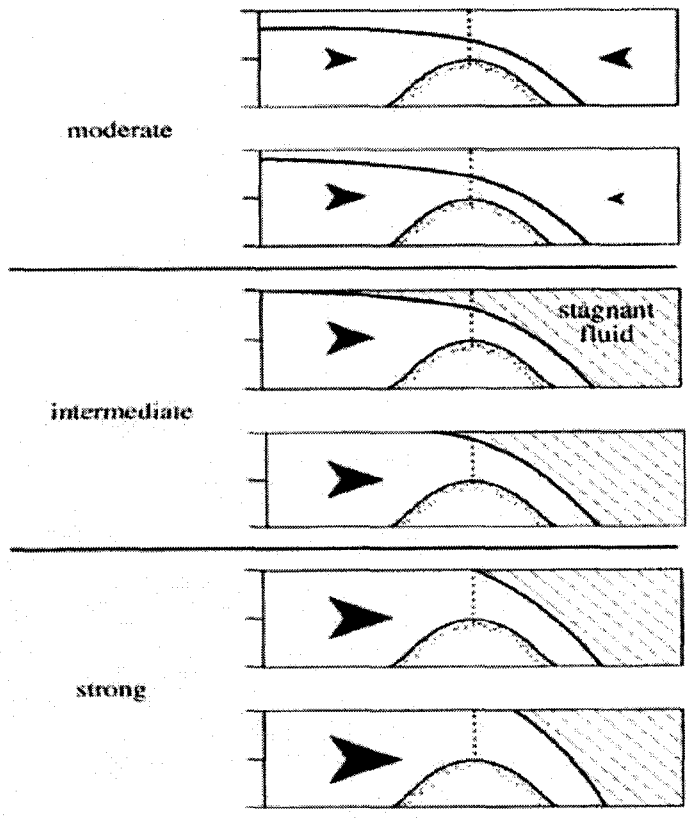

Figure 3.1: *Sketch of barotropically forced sill flow (adapted from Farmer & Armi (1986)).*

where the internal lower layer Froude number is $F_2^2 = u_2^2/g'h_2 = 1$, with the reduced gravity g', the lower layer current speed u_2 and layer thickness h_2.
At even stronger flows, the front is quickly pushed past the sill crest and the plunge point is now located downstream of the sill crest.

Observations at Boundary Pass do not show much evidence of the stages of weak and intermediate flow. Only one of the 46 transects across the sill at flood tide taken during Vector cruise 0032 shows a lower layer plunge point which is located right above the sill crest, indicating the transition from intermediate to strong forcing. It is quite possible that the first two stages have been missed during the measurements, as the time span between slack tide and strong forcing is only about half an hour, while it took about 1 hour to carry

out a complete transect across the sill and to steam upstream again for the next transect. The case of strong barotropic forcing, however, has been observed between 30 min and 90 min after slack tide: 4 transects in September 2000 and one in January 2002 clearly show a plunge point downstream of the sill crest and an interface indicating hydraulic flow. This flow stage has been also observed by Farmer & Smith (1980) during their brief measurements at Boundary Pass.

When the forcing increases even further, the flow shoots over the sill as a jet, which separates from the sill crest (Section 2). The flow field downstream of the sill crest is characterized by irregular convergence/divergence patterns associated with strong eddy activity. No clear front line is apparent anymore, but gas bubble clouds – indicating downwelling currents – are spread over a distance of about 2 km, starting several hundreds of meters downstream of the sill.

It is likely that the aerated water at this stage is not dense enough to reach intermediate depths, because it is too diluted by the intense mixing processes. In the following, we will therefore focus our considerations on the case of strong barotropic forcing. First, the observations will be discussed in detail, before the flow field is modeled as described in Section 3.1.

Observations of hydraulic flow at Boundary Pass

The best example of the flow during the early stage of the flood tide is shown in Figure 3.2. It is an enlargement of Figure 2.5, showing the bottom depth as a dark red line of high backscatter intensity and a red/orange area just above it which is an artificial effect caused by the sidelobe characteristics of the echo sounder. The high intensities extending from the sea surface to about 105 m depth indicate gas bubbles. These are subducted at the lower layer plunge point at about 120 m downstream of the sill crest (at $x = 0$) and are carried down by the currents along the interface between upper and lower layer.

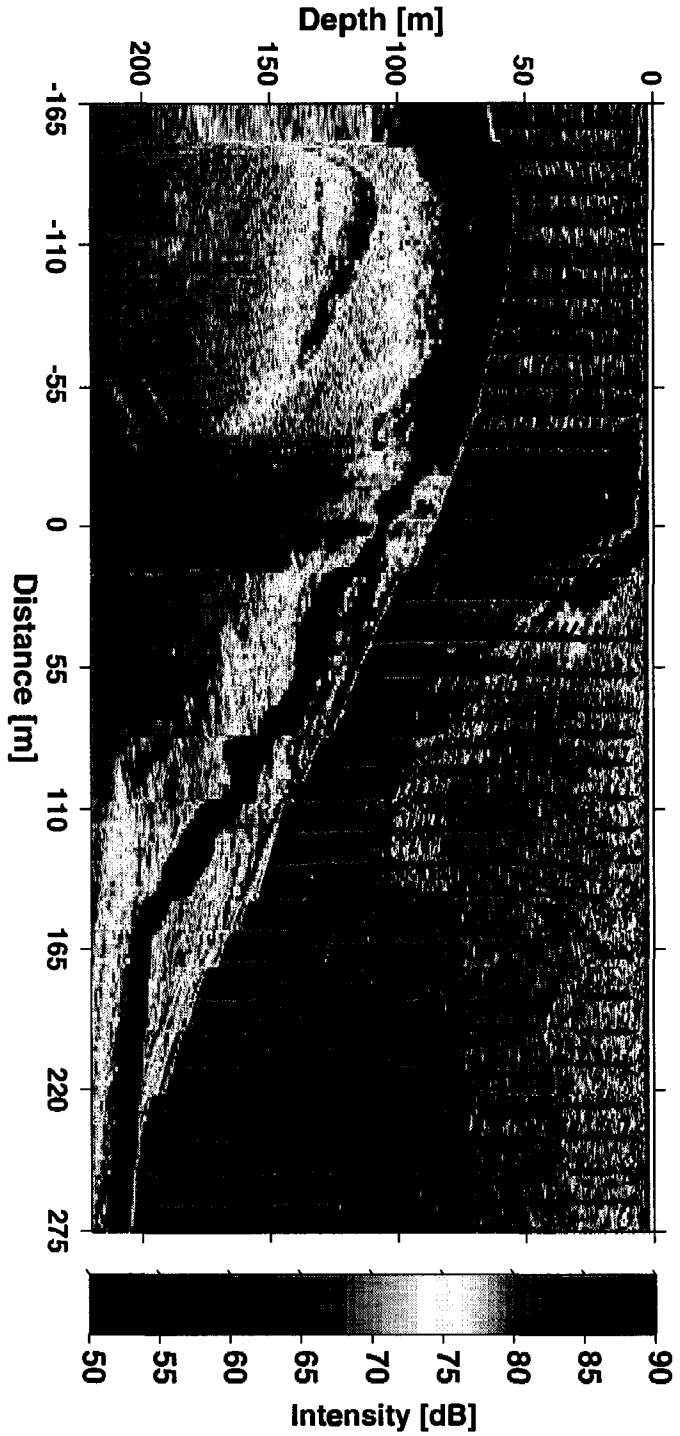

Figure 3.2: *Flow over the sill at Boundary Pass during the early stage of the flood tide (~ 1.5 h after low tide) on September 29, 2000. The colors show the acoustic backscatter intensity measured with an echo sounder and the black arrows indicate the current speed perpendicular to the sill crest. Note that distances in the horizontal and vertical are the same.*

The arrows indicate the current speed in the plane orthogonal to the sill crest. Lower layer currents are mainly parallel to the bathymetry and reach speeds of about $2.2\,\mathrm{m\,s^{-1}}$ at the sill crest and $1.7\,\mathrm{m\,s^{-1}}$ towards the bottom of the sill and before the transition to the subsequent hydraulic jump. The upper layer currents are weak with variable flow directions. Some overturning cells indicate mixing in the upper layer at a depth of $50-150\,\mathrm{m}$.

The observations provide a quasi-synoptic picture of the flow field, as it took only 6 min to complete the part of the transect shown in Figure 3.2, while the time scale over which the tidal currents change is on the order of 1 h.

The change of the lower layer volume transport along the slope of the sill can be estimated from ADCP measurements. The steep bathymetry causes problems in parts of the lower layer, where the currents could not be measured due to the side lobe effect of the ADCP. However, at the sill crest and at the bottom of the sill these effects are minimal, allowing a good estimate of currents and layer thickness. A comparison of the measurements at these two locations shows that about 60% (!) of the lower layer volume is lost to the upper layer by detrainment on its way down the slope (see also below for further discussion).

The corresponding densities are shown in Figure 3.3. The towed instrument (CTD) could be lowered into the lower layer above the sill crest, but not at the downstream side of the sill due to the high current speeds. Densities in the lower layer range between $1023.5\,\mathrm{kg\,m^{-3}}$ and $1042.2\,\mathrm{kg\,m^{-3}}$, while in the upper layer, densities are as low as $1020.1\,\mathrm{kg\,m^{-3}}$ in the fresh and shallow surface layer and increase to about $1023.4\,\mathrm{kg\,m^{-3}}$ close to the interface. The data clearly show the big density jump across the interface at a depth of 15 m at a location close to the plunge point.

Approximations for modeling

The observations justify some approximations which will apply to the model presented in Section 3.1. In particular, it will be assumed that the sill flow at the early stage of the flood tide (0.5-1.5 h after slack tide at Boundary Pass) can be described as a quasi-steady,

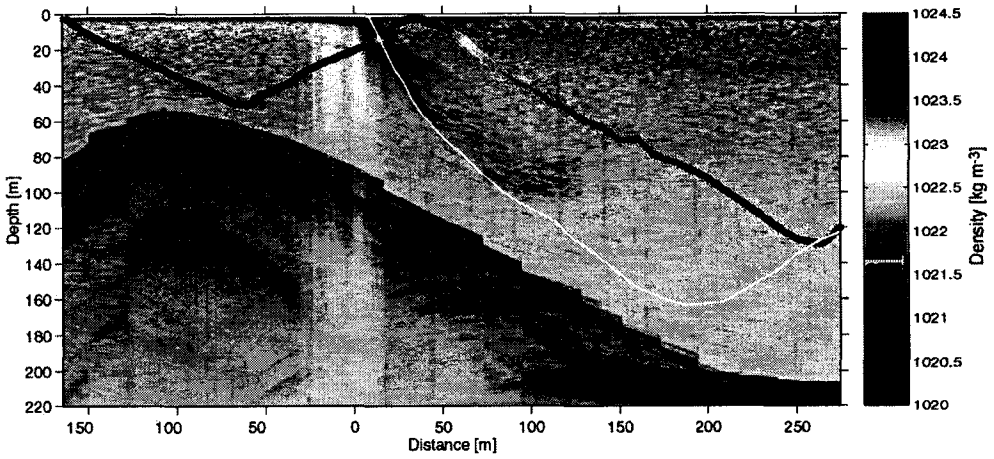

Figure 3.3: *Density (color) of the transect shown in Figure 3.2. Measurements are shown along the path of the instrument. The green line indicates the bottom depth, the white line the interface location.*

inviscid, and irrotational 2-layer flow, with constant lower layer and variable upper layer density. The justification for these approximations will be given in the following.

The observations (Figure 3.2) show that the sill flow is characterized by two distinct layers: a fresh surface layer downstream of the sill crest and a lower layer of denser, fast flowing water. This 2-layer structure is adapted in the models and is sketched in Figure 3.4.

The layer densities are denoted ρ_i and the horizontal current speeds, orthogonal to the sill crest, u_i. η_1 is the sea surface, η_2 the interface between upper and lower layer, B the bottom depth, h_i the layer thicknesses, and v_{ij} the entrainment/detrainment velocity between both layers (entrainment is defined as volume gain by transport across the interface; detrainment is volume loss). The indices $i=1,2$ refer to upper and lower layer respectively. The values at the frontal location (i.e. the plunge point of the lower layer) are indicated by the subscript f and the values at the end of the sill slope by subscript s.

A coordinate system is used with the x-axis in along-strait direction (perpendicular to the sill crest), with x increasing towards the Strait of Georgia, and the z-axis in the vertical,

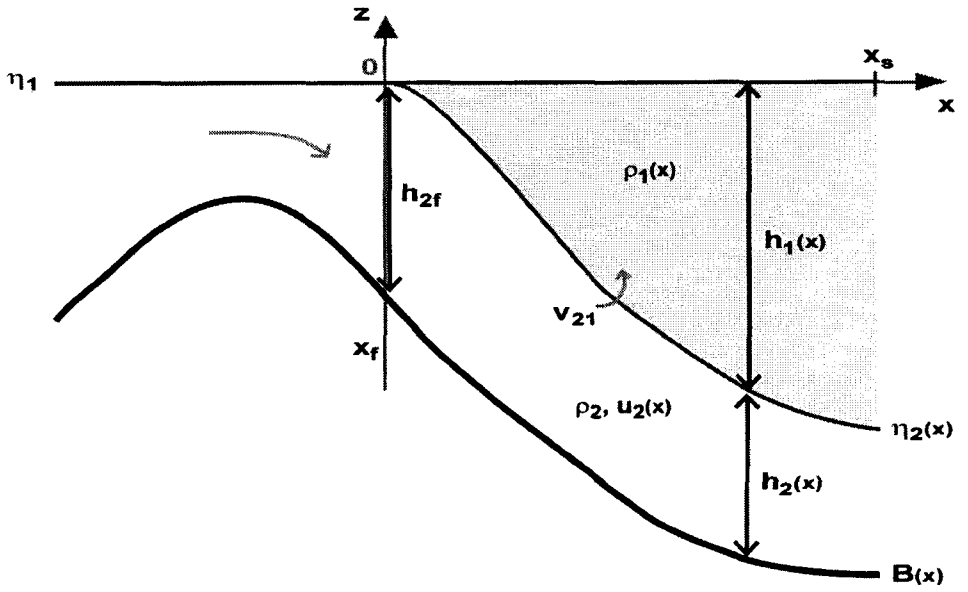

Figure 3.4: *Sketch of the flow over the sill at Boundary Pass. For explanations see text.*

with positive values upwards. At the frontal location $z=0, x=0$.

For easier calculation, it is assumed that the horizontal current speed u_i and density ρ_i are vertically homogeneous within each layer. For the current speed and lower layer density this approximation seems to be quite reasonable, while the upper layer density data suggest that ρ_1 changes significantly with depth. The implications of this for modeling the sill flow will be discussed below.

Measurements show that the sill flow can be considered to be 2-dimensional, since the transverse flow component is small in comparison to the component normal to the sill. In the lower layer, the transverse current speed reaches its maximal values of $50\,\mathrm{cm\,s^{-1}}$ (or 40% of the flow component normal to the sill) in two small patches close to the interface, but is in general less than $20\,\mathrm{cm\,s^{-1}}$ ($< 15\%$). In the upper layer, both flow components are partly of the same order of magnitude, but are always weak with variable flow directions. They are dynamically irrelevant, because the upper layer Froude number is $F_1^2 = u_1^2/g'h_1 \ll 1$ (Figure 3.5c), so that the layer can be considered to be passive and the sea surface can be

treated as a rigid lid, i.e. $d\eta_1/dx = 0$ (Armi & Farmer, 1986).
A consequence of 2-dimensionality is that the earth's rotation is neglibible, an assumption which is supported by the fact that the time scale for the fluid to flow over the sill is short in comparison to a pendulum day.

A transverse flow component which is small in comparison to the component normal to the sill does not necessarily mean that it is negligible for the volume loss, as lateral divergence may still be significant. The importance of divergence can be estimated by integrating the measured volume transport vertically over the whole water column. If the transport is a fairly constant with x, lateral divergence is not important. However, the transverse flow component in the upper layer is – although dynamically negligible – too big for a reliable estimate.

Instead, we may address this question with the following simple argument: The initial volume transport per unit width at the lower layer plunge point is $q_{2f} = 160\,\mathrm{m^2\,s^{-1}}$. The 2-layer hydraulic flow is observed everywhere along the sill (sill width $\mathcal{W} = 1500\,\mathrm{m}$), so that the total volume loss (60% of the initial volume transport) is $144\,000\,\mathrm{m^3\,s^{-1}}$. If we assume that all of this volume loss is caused by divergence only, the required velocity difference between both sides of the sill would have to be $7.2\,\mathrm{m\,s^{-1}}$ for a lower layer thickness of 100 m and a horizontal distance of 200 m in main flow direction. This is an order of magnitude higher than the maximal observed lateral current speed of $0.5\,\mathrm{m\,s^{-1}}$, so that it seems unlikely that lateral divergence contributes significantly to the volume loss, although it cannot be ruled out completely.

Due to the very substantial loss of lower layer volume between sill crest and the end the sill slope, it is assumed that the entrainment of water from the upper into the lower layer is negligible ($v_{12} = 0$). This also means that the lower layer density ρ_2 is horizontally constant, which seems to be supported by the fact that lower layer densities far downstream of the sill ($x = 1000\,\mathrm{m}$) are still very high with values around $1024\,\mathrm{kg\,m^{-3}}$. The upper layer density, however, changes horizontally due to the effects of detrainment.

It is also assumed that the flow is quasi-steady, i.e. the time scales for the adjustment of the flow due to changes of the tidal flow ($\mathcal{O}(1\,\mathrm{min})$) are small in comparison to the ones of the tidal flow itself ($\mathcal{O}(1\,\mathrm{h})$). Hence, the time derivatives of density ρ_i and current speed u_i are dropped, i.e. $\partial/\partial t \equiv 0$.

The importance of friction can be estimated from the ratio of deceleration due to bottom friction $C_d u^2/H$ and acceleration due to hydraulic effects u^2/L (Pratt, 1986). With the mean lower layer thickness $H = 60\,\mathrm{m}$, the horizontal distance over which the currents change significantly, given by $L = 200\,\mathrm{m}$, and a conservative value for the drag coefficient $C_d = 5 \cdot 10^{-3}$, the ratio is $C_d L/H = 0.017$. Locally this value can be higher (e.g. at flow separation points), but overall friction is not important for the flow at Boundary Pass and will therefore be neglected.

In most models of the hydraulic sill flow, it is assumed that the slopes of the bathymetry dB/dx are moderate, so that the hydrostatic approximation can be applied and the vertical flow component neglected. Considering that the slope of the sill at Boundary Pass is as high as 30° and vertical velocities reach up to $75\,\mathrm{cm\,s^{-1}}$, this assumption may seem questionable. However, non-hydrostatic effects are only important when the flow curvature is significant (Zhu & Lawrence, 1998), but can be neglected over constant slopes, like the region of interest between plunge point and the bottom of the sill.

Lower layer hydraulics

Sill flows can be characterized by the internal Froude number $F_i^2 = u_i^2/g'h_i$ (Armi & Farmer, 1986; Farmer & Armi, 1986, 1999), which is given by the ratio of current speed u_i and wave speed $\sqrt{g'h_i}$. For $u_i^2 < g'h_i$, the flow is called subcritical and for $u_i^2 > g'h_i$ supercritical.

As already discussed, for the sill flow at Boundary Pass the upper layer Froude number is negligible ($F_1^2 \ll 1$), so that the dynamics of the flow are determined by the lower layer. The lower layer Froude number can be also expressed in terms of the volume transport $q_2 = u_2 h_2$. Together with the integrated volume loss $\delta(x) = \int_{x_f}^{x} v_{21}/q_{2f}\,dx$ we yield an expression for

the lower layer transport $q_2 = q_{2f}(1-\delta)$, which can then be incorporated in the Froude number

$$F_2^2 = \frac{u_2^2}{g' h_2} = \frac{q_2^2}{g' h_2^3} = \frac{q_{2f}^2 (1-\delta)^2}{g' h_2^3} \quad . \tag{3.1}$$

For critical flow, the Froude number is given by

$$F_2^2 = \frac{q_2^2}{g' h^3} = 1 \quad . \tag{3.2}$$

For weak or intermediate forcing, this condition is satisfied at the sill crest. For strongly forced flows, however, $q_2 > g' h_2^3$ at the crest, which means that the lower layer plunge point will be pushed downstream to a location, where the layer depth (here equal to the water depth) h_2 is big enough to satisfy equation (3.2) (Farmer & Armi, 1986). The location of the plunge point depends therefore on the strength of the barotropic forcing q_2 and adjusts constantly to it. When the flow slackens, the front will move upstream again and re-establish the control condition at the sill.

Downstream of the plunge point, the flow is supercritical (Figure 3.5). This is also suggested by observations of the interface depth, showing a decreasing layer thickness downstream of the plunge point until the beginning of the hydraulic jump at $x = 200\,\mathrm{m}$.

Initial conditions

The initial conditions for the models are chosen on base of the observations and previously presented approximations. In particular, the lower layer thickness h_2 and volume transport q_2, as well as the detrainment velocity v_{21} and reduced gravity g' will have to be prescribed.

The detrainment velocity and hence also the changes in upper layer density and reduced gravity are zero upstream of the plunge point ($x < 0$) and downstream of the bottom of the sill ($x > x_s = 200\,\mathrm{m}$).

The detrainment velocity v_{21} is determined by dividing the total volume loss Δq_{2f}

($\Delta = 0.64$) by the distance $L = 200\,\mathrm{m}$ from the plunge point to the bottom of the sill. Alternatively, it can be calculated from lower layer current speed and thickness (and hence volume transport) provided by the measurements. While the interface thickness is reliably given by the acoustic backscatter intensity of ADCP and echo sounder, the lower layer current speed data cannot be used close to the bottom due to the side lobe effect of the ADCP. The missing data are filled in with the vertical mean value of the layer speed at each location, assuming that the currents are fairly constant with depth (bottom friction is negligible as discussed above). The resulting detrainment velocity is plotted in Figure 3.5d.

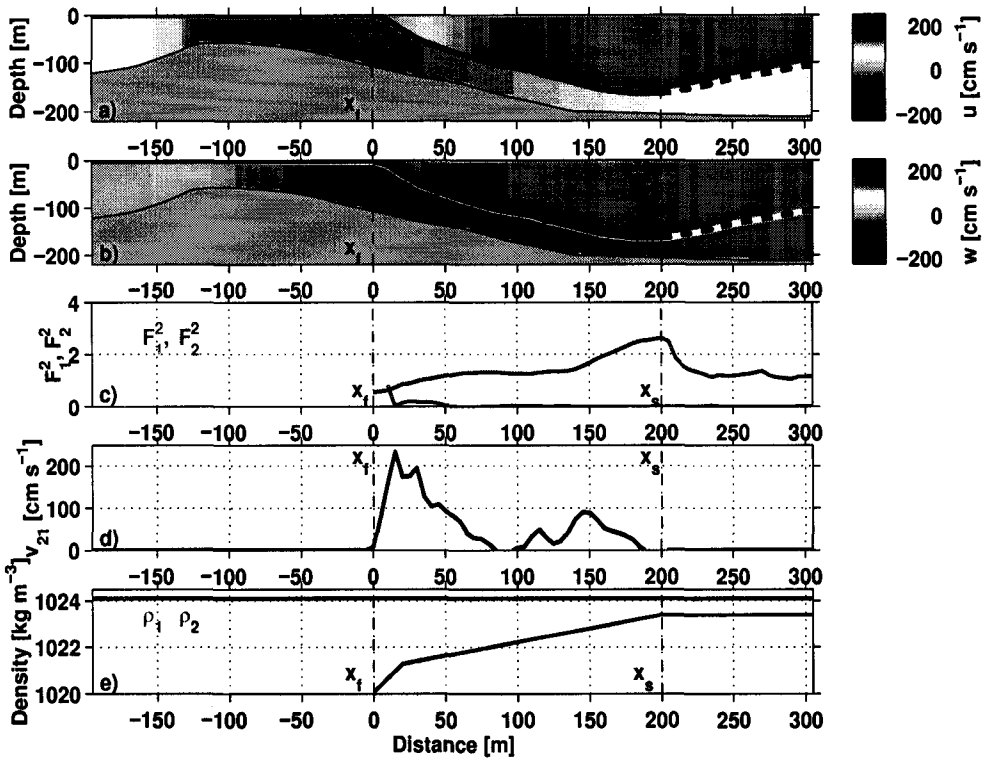

Figure 3.5: *Observed layer-averaged horizontal (a) and vertical (b) flow component u and w; c) upper and lower layer Froude numbers F_1^2 and F_2^2; d) detrainment velocity v_{21}; e) prescribed densities ρ_1 and ρ_2.*

The reduced gravity $g'(x)$ is determined from the upper and lower layer densities. ρ_1 is described by a rapid linear increase from $\rho_{1f} = 1020.1\,\mathrm{kg\,m^{-3}}$ at $x = 0$ to $1021.3\,\mathrm{kg\,m^{-3}}$ at $x = 20\,\mathrm{m}$ in the shallow surface area and by a more gradual change further downstream to $\rho_{1s} = 1023.4\,\mathrm{kg\,m^{-3}}$ at $x = 200\,\mathrm{m}$ (Figure 3.5e). The lower layer density $\rho_2 = 1024.1\,\mathrm{kg\,m^{-3}}$ is assumed to be constant.

3.1 Energy model based on the Bernoulli-equation

Hydraulically controlled flow over a sill can be described with an energy model based on the Bernoulli equation. This model of inviscid and stationary flow is adapted from Farmer & Armi (1999), who applied it to the sill flow in Knight Inlet, BC, Canada. It has the advantage that an analytical solution can be derived.

The Bernoulli equation

$$\frac{1}{2}u_2^2 + g'(h_2 + B) \equiv E_2 = const. \quad , \tag{3.3}$$

with the Bernoulli constant E_2, can be either derived from the conservation law of energy or by horizontal integration of the simplified momentum equations. In this model, the energy of the lower layer is constant, as no water is exchanged with the passive upper layer. However, a small exchange rate can be incorporated by expressing the volume transport in terms of the current speed $q_2 = u_2 h_2$ and by describing the horizontal change of volume in terms of the volume loss δ of water from the lower into the upper layer by $q_2 = (1-\delta)\,q_{2f}$, so that we get

$$\frac{q_{2f}(1-\delta)^2}{2\,g' h_2^2} + h_2 + B = \frac{E_2}{g'} \quad . \tag{3.4}$$

The reduced gravity g' is now a function of x as the upper layer density changes horizontally. At the frontal location x_f, the flow is critical (Farmer & Armi, 1986) so that the Froude

number there is

$$F_2^2 = \frac{q_{2f}^2}{g'_f\, h_{2f}} = 1 \quad , \tag{3.5}$$

which yields

$$\frac{h_{2f}^3\, g'_f (1-\delta)^2}{2\, g' h_2^2} + h_2 + B = \frac{E_2}{g'} \quad . \tag{3.6}$$

This equation can be made dimensionless by scaling layer thickness, bottom depth, and reduced gravity with the lower layer thickness and reduced gravity at the frontal location ($\hat{h}_2 = h_2/h_{2f}$, $\hat{B} = B/h_{2f}$, $\hat{g}' = g'/g'_{2f}$), so that we get

$$\frac{(1-\delta)^2}{2\,\hat{g}'\hat{h}_2^2} + \hat{h}_2 + \hat{B} = \frac{E_f}{h_f g'} \equiv \hat{E}_f \quad , \tag{3.7}$$

where the dimensionless Bernoulli constant is $\hat{E}_f = 1/2$ (at the frontal location $\hat{g}' = 1$, $\hat{h} = 1$, $\hat{B} = -1$). This equation can be rewritten as a polynomial of 3rd order

$$\hat{h}_2^3 + \hat{h}_2^2\,(\hat{B} - \hat{E}_f) + \frac{(1-\delta)^2}{2\,\hat{g}'} = 0 \quad , \tag{3.8}$$

which can be solved analytically. The solution yields the position of the interface $\hat{\eta}_2 = \hat{B} + \hat{h}_2$ from which the horizontal flow component of the lower layer $\hat{u}_2 = \hat{q}_2/\hat{h}_2$ can be calculated.

The vertical flow component $\hat{w}$ is derived from geometrical considerations and volume conservation. At the bottom $\hat{B}$, the lower layer flow is parallel to the bottom, so that $\hat{w}$ is given by

$$\hat{w} = \hat{u}\,\frac{d\hat{B}}{d\hat{x}} \quad . \tag{3.9}$$

At the upper bound of the layer, the flow is mainly along the interface $\hat{\eta}_2$, but has also a small component orthogonal to it, given by the entrainment velocity from the lower into

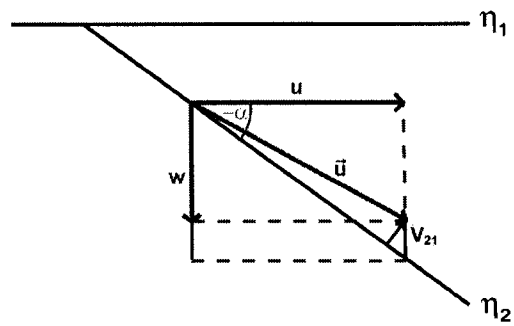

Figure 3.6: *Sketch for the calculation of the vertical flow component w. The current vector is $\vec{u}$, the horizontal flow component u, the detrainment velocity v_{21}, and the slope of the interface α*

the upper layer $\hat{v}_{21}$. According to Figure 3.6, $\hat{w}$ is then at the interface

$$\hat{w} = \hat{u} \tan\alpha + \frac{\hat{v}_{21}}{\cos\alpha} \quad , \tag{3.10}$$

where $\tan\alpha = d(\hat{B} + \hat{h}_2)/d\hat{x}$ is the slope of the interface. The lower layer vertical velocity $\hat{w}$ is then the mean of the values at the upper and lower bounds of the layer.

The resulting flow is plotted for the original case without detrainment $\Delta \equiv 0$ and constant $\hat{g}'$ (Equation 3.3, Figure 3.7), as well as for the case with detrainment (Equation 3.8), where a total relative volume loss of $\Delta = 0.64$ and a variable $\hat{g}'(x)$ are used (Figure 3.8). The values for $\hat{v}_{21}$ and $\hat{g}'(x)$ are determined from measurements as described above.

In the first case (Figure 3.7), the calculated interface depth is close to the observed one, but the current speed is much too high (differences up to $1.5\,\mathrm{m\,s^{-1}}$; see Figure 3.5 for comparison). The reason for this is the neglect of the significant detrainment rate, which is therefore included in the second case (Figure 3.8). The calculated interface depth is similar to the one before, but due to the incorporated volume loss, the lower layer currents are now much closer to the observed ones, with differences of the order of $0.4\,\mathrm{m\,s^{-1}}$ for u_2 and $0.6\,\mathrm{m\,s^{-1}}$ for w.

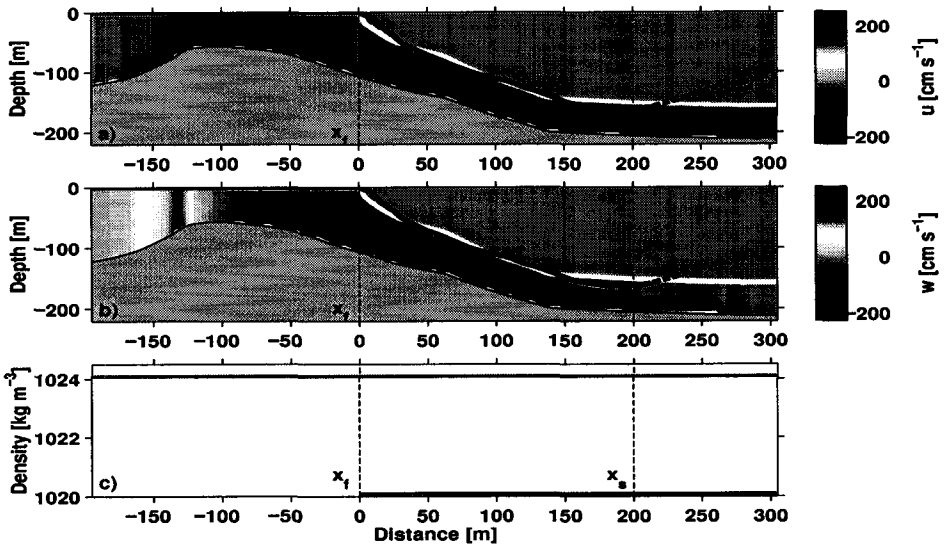

Figure 3.7: *Observed (black line) and modeled interface depth for the model without detrainment (white line; Eq. 3.3). a) Horizontal currents; b) vertical currents; c) prescribed density for upper (red) and lower layer (blue).*

These results depend sensitively on the prescribed upper layer density gradient, the total volume loss due to detrainment, and the changes of the detrainment velocity along the slope. The available flow and density measurements are very sparse and can only give an idea of the hydrographic conditions of the sill flow. They do not provide an accurate horizontal gradient of detrainment velocity or upper layer density, which is essential for getting useful model results. A somewhat realistic estimate of the vertical flow component, which is of primary importance for estimating the contribution of gas bubbles to the air-sea gas exchange in tidal fronts (Section 6), can therefore – with the present boundary conditions – not be derived with the model.

Instead, the observed flow field will be used. But it should be also kept in mind that the current speeds are derived from ADCP measurements, which are based on the assumption of horizontal flow homogenity. Considering that the beams in 100 m depth spread over a distance of 73 m, it is clear that the data should be treated with some caution in such a

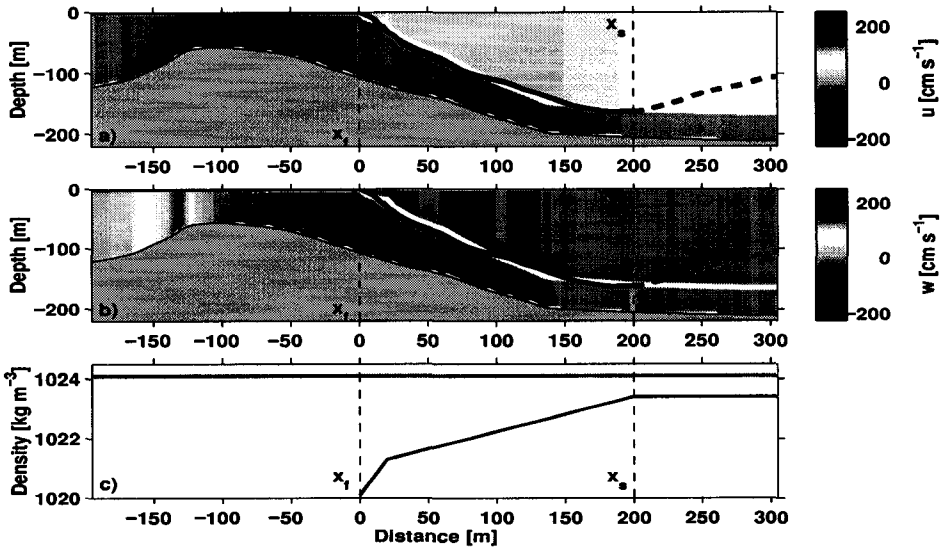

Figure 3.8: *Observed (black line) and modeled interface depth (white line) for the model with detrainment and variable $g'(x)$ (white line; Eq. 3.8). a) Horizontal currents; b) vertical currents; c) prescribed density for upper (red) and lower layer (blue).*

highly variable environment like at Boundary Pass.

4 Model for gas bubble formation by breaking waves on a current

Most tidal fronts are characterized by converging flow at the sea surface with either both water masses flowing towards the front (e.g. Stuart Island) or one of them being stagnant (e.g. Boundary Pass). Surface gravity waves, which are generated by wind or any other disturbance of the sea surface, travel into the convergence zone, steepen due to the effect of the opposing currents, and tend to break (Figures 4.1, 4.2). This situation is similar to the one for waves breaking in shallow water. Wave energy is dissipated by breaking and gas bubbles are injected into the surface water which is then subducted by the downwelling currents enhancing the air-sea gas exchange.

Figure 4.1: *Wave breaking in the convergence zone of the Stuart Island ebb tidal front.*

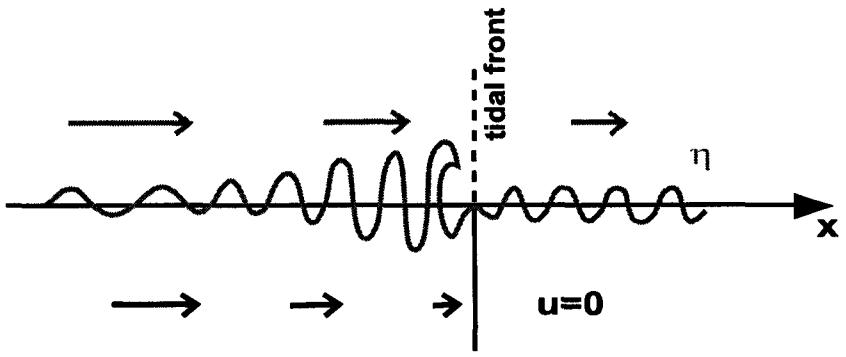

Figure 4.2: *Sketch of wave-current interaction in a convergence zone (η: sea surface elevation). The transition is from fast current (in the same direction) to still water ($u=0$).*

During flood tide at Boundary Pass, the waves approaching the convergence zone encounter two slightly different situations depending on the direction from which they travel into the front: waves approaching from the west ride on the strong tidal currents until they reach the front, which marks the transition to the stagnant surface layer in the east (Strait of Georgia, Figure 4.2). For waves approaching the front from the east, the transition is from stagnant water to fast opposing currents. The general problem, however, is adequately described by the first case. The difference between the two cases, which is important for determining the location of wave breaking relative to the tidal front, will be discussed in Section 6.2.

In this section, the behaviour of waves travelling on a spatially slowly varying current is described. After introducing some basic wave equations, a model for wave-current interaction is reviewed. This leads to considerations on wave breaking, energy dissipation, and the generation of gas bubbles at the sea surface.

4.1 Basic wave equations

The sea surface excursion η of a train of monochromatic sinusoidal waves travelling in x-direction can be described by

$$\eta(x,t) = a\cos(kx - \omega t + \phi) \quad , \tag{4.1}$$

where a is the amplitude, k the wave number, ω the frequency, and ϕ the phase of the wave. We assume that the processes can be described by linear wave theory and that wave-wave interactions can be neglected.

The dispersion relation for gravity waves (Krauss, 1973) is given by

$$\tanh kH = \frac{\omega^2}{gk} \quad , \tag{4.2}$$

where H is the water depth and g the gravitational acceleration. This yields together with the expression for the phase speed $c = \omega/k$

$$c = \sqrt{\frac{g}{k}\tanh kH} \quad . \tag{4.3}$$

The wind generated gravity waves in the protected waters of the Fraser estuary typically have a wave length λ of up to a few meters. Since the water depth is of the order of 150−200 m (at Boundary Pass $H = 60$ m), $\lambda \ll 2H$ and hence the waves can be treated as deep water waves (short waves), with an error of less than 0.5%.

For $\lambda \ll 2H$, the expression in the square root in equation (4.3) is then approximately given by $\tanh(kH) = \tanh(2\pi H/\lambda) \approx 1$, so that we get a simplified equation for the phase speed

$$c = \sqrt{g/k} \quad , \tag{4.4}$$

which shows that deep water waves are dispersive, i.e. waves with different wave numbers k travel with different phase speeds.

The wave energy is transported with the group velocity c_g. It is given for deep water waves by

$$c_g = \frac{d\omega}{dk} = \frac{c}{2} \quad . \tag{4.5}$$

The potential energy per unit area E_{pot} of a sinusoidal wave is calculated by integrating the local potential energy over a wave length λ

$$E_{pot} = \frac{1}{\lambda}\int_0^{\lambda} \frac{\rho g \eta^2}{2} dx = \frac{\rho g k}{4\pi}\int_0^{2\pi/k} a^2 \cos^2(kx - \omega t) dx = \frac{\rho g a^2}{4} \quad , \tag{4.6}$$

in which a constant density ρ, $\lambda = 2\pi/k$, and the general wave equation (4.1) were used. The potential energy is set to zero at the mean sea surface height.

The sum of kinetic and potential energy is constant (with a phase difference of $\pi/2$ between the two), so that the total energy E of a wave is given by

$$E = \frac{\rho g a^2}{2} \quad . \tag{4.7}$$

This is also true for a wave travelling on a current, if a reference frame moving with the currents is chosen.

4.2 Wave-current interaction

In the absence of any currents, a monochromatic wave is characterized by wave number k_0, amplitude a_0, and phase speed c_0. When the wave encounters a current, these values are changed to k, a, and c. In the following, variables in a reference frame moving with the currents have no subscript while variables in a medium at rest ($u = 0$; u is the horizontal

current speed) are marked by the subscript '0'.

For waves travelling on a current, the frequency for a fixed reference frame is

$$ku + \omega = const. \equiv \omega_0 \quad , \tag{4.8}$$

where ω_0 is the frequency at $u = 0$ (Phillips, 1977). With the expressions $\omega = \sqrt{gk}$ and $c = \sqrt{g/k}$ we get

$$k(u + c) = k_0 c_0 \quad , \tag{4.9}$$

from which we can derive a quadratic equation for the phase speed c, which has the solution

$$\frac{c}{c_0} = \frac{1}{2} + \frac{1}{2}\sqrt{1 + \frac{4u}{c_0}} \quad . \tag{4.10}$$

Bretherton & Garrett (1969) derived a conservation equation for wave action, which is valid for waves travelling on a slowly varying current (i.e. the currents change only little over a wave length)

$$\frac{\partial}{\partial t}\left(\frac{E}{\omega}\right) + \nabla \cdot \left\{(\mathbf{u} + \mathbf{c}_g)\frac{E}{\omega}\right\} = 0 \quad , \tag{4.11}$$

where $\mathbf{u}$ and $\mathbf{c}_g$ are the vectors of the current speed and group velocity. For steady wave trains travelling in the x-direction this can be written as

$$\frac{d}{dx}\left\{(u + c_g)\frac{E}{\omega}\right\} = 0 \quad , \tag{4.12}$$

so that we get for deep water waves, using $\omega = g/c$ and equations (4.4) and (4.5)

$$E\left(u + \frac{1}{2}c\right)c = const. \equiv \frac{1}{2}E_0 c_0^2 \quad . \tag{4.13}$$

Together with the wave energy equation (4.7) we finally get an expression for the wave

amplitude (Phillips, 1977)

$$\frac{a}{a_o} = \frac{c_0}{\sqrt{(2u+c)c}} \quad . \tag{4.14}$$

The wave energy is then given by $E/E_0 = (a/a_0)^2$ and is shown in Figure 4.3 (black curve) as a function of the normalized current speed u/c_0. The waves travel from left to right (for explanations of the other curves see next section). At $u=0$, $E/E_0=1$ by definition and E/E_0 goes towards infinity as u goes towards the negative group speed of the wave ($u/c_0=-1/4$).

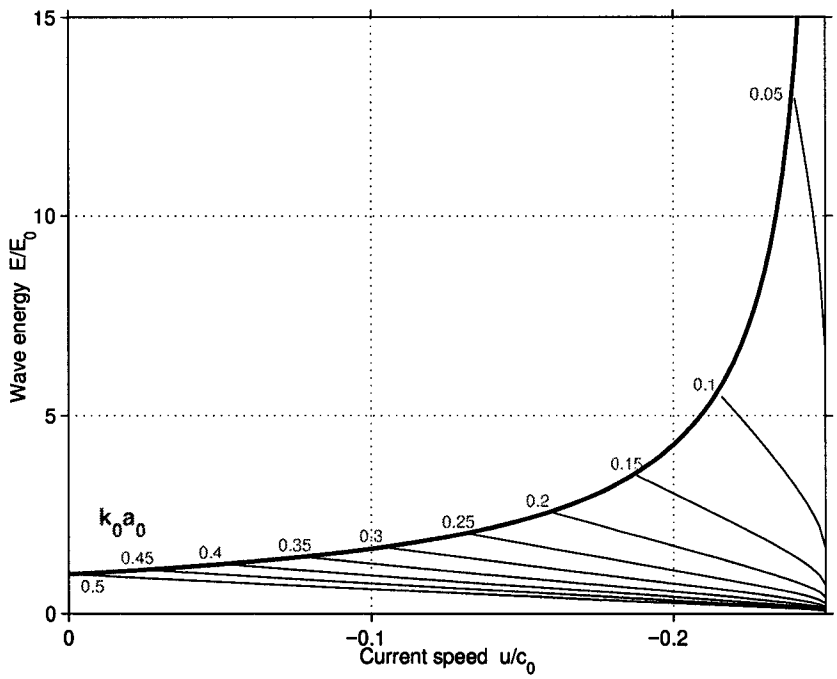

Figure 4.3: *Wave energy as a function of current speed. Current speed and amplitude are scaled with the values for a medium at rest ($u=0$). The wave energy in the absence of wave breaking (black curve) is plotted together with the wave energy for a breaking wave of initial steepness k_0a_0 (gray curves, Equation 4.16).*

4.3 Breaking waves on a current

In reality, waves do not reach infinite amplitudes but break when they reach a critical steepness of

$$ka = \frac{1}{2} \tag{4.15}$$

(Longuet-Higgins, 1969). This process is essential for the formation of gas bubbles in the convergence zone of a tidal front and will therefore be studied in the following in more detail.

Obviously, the location at which the wave breaks, the amplitude of the wave, and also the amount of dissipated energy depends on the current speed but also on the initial wave number k_0 and wave height a_0. Figure 4.3 shows – as described above – the energy of a wave travelling on an opposing current (the amplitude can be derived from this by taking the square root of the energy). At some point the wave reaches its critical steepness and breaks. For waves with high initial steepness $k_0 a_0$ this will happen at low current speeds and for waves with lower initial steepness at higher current speeds. To derive the equation for the energy of a breaking wave, equation (4.15) is multiplied by $1/(ka_0)$. By also using the expression $(c/c_0)^2 = k_0/k$ we get

$$\frac{a}{a_0} = \left(\frac{c}{c_0}\right)^2 \frac{1}{2k_0 a_0} \quad , \tag{4.16}$$

where c/c_0 is given by equation (4.10). $E/E_0 = (a/a_0)^2$ yields the change of energy and is plotted in Figure 4.3 for different initial steepnesses $k_0 a_0$ (gray curves). The more the currents increase the more energy is lost by breaking. The amplitude at which the wave breaks decreases as the wave travels further against the current, because the wave number increases with current speed.

4.3.1 Amplitude and energy of a breaking wave

The phase speed of a deep water wave on a current is given by equation (4.10). The current speed equals the group velocity at a current speed of $u/c_0 \geq -1/4$, which means that the wave cannot proceed against the currents anymore and will have to break somewhere in the convergence zone. To calculate the amplitude of a wave when it breaks, we insert equation (4.9) into (4.14) and use $(c/c_0)^2 = k_0/k$, yielding

$$\left(\frac{a_0}{a}\right)^2 = \frac{c}{c_0^2}\left(2\frac{k_0 c_0}{k} - 2c + c\right) = 2\left(\frac{k_0}{k}\right)^{3/2} - \frac{k_0}{k} \quad , \tag{4.17}$$

which is then multiplied by $(a_0/a)^{3/2}$

$$\left(\frac{a_0}{a}\right)^{7/2} + \frac{k_0 a_0}{ka}\left(\frac{a_0}{a}\right)^{1/2} - 2\left(\frac{k_0 a_0}{ka}\right)^{3/2} = 0 \quad . \tag{4.18}$$

Together with the condition for wave breaking $ka = 1/2$ we get

$$\left(\frac{a_0}{a}\right)^{7/2} + 2k_0 a_0\left(\frac{a_0}{a}\right)^{1/2} - 2(2k_0 a_0)^{3/2} = 0 \quad . \tag{4.19}$$

This equation can be solved for the relative amplitude a/a_0 which is plotted in Figure 4.4 as the gray curve, which shows the situation for a wave travelling from still water (right) to fast opposing current (left, Figure 4.2). The corresponding current speed is indicated by the black dots and numbers. The amplitude at which the wave breaks depends only on its initial steepness and increases with decreasing $k_0 a_0$. It goes towards infinity as $k_0 a_0$ goes towards zero.

The amplitude $k_0 a$ can also be plotted as function of current speed by multiplying equation (4.14) by $k_0 a_0$ – the result is plotted in Figure 4.5. A wave of initial steepness $k_0 a_0$ travels from left to right into the convergence zone (gray curves) until it breaks. From then on it follows the black curve (in the absence of breaking it would follow the dashed gray curves),

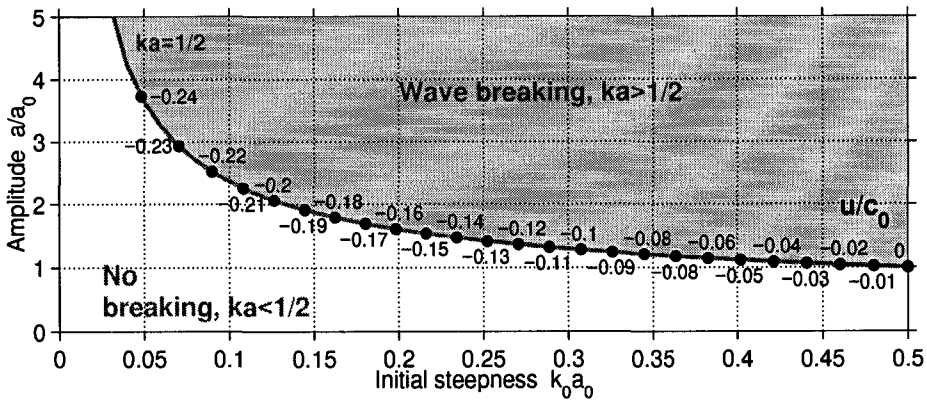

Figure 4.4: *Relative change of amplitude of a breaking wave as function of the initial wave steepness. The numbers indicate the corresponding current speed* u/c_0.

which is derived by multiplying equation (4.16) by k_0a_0.

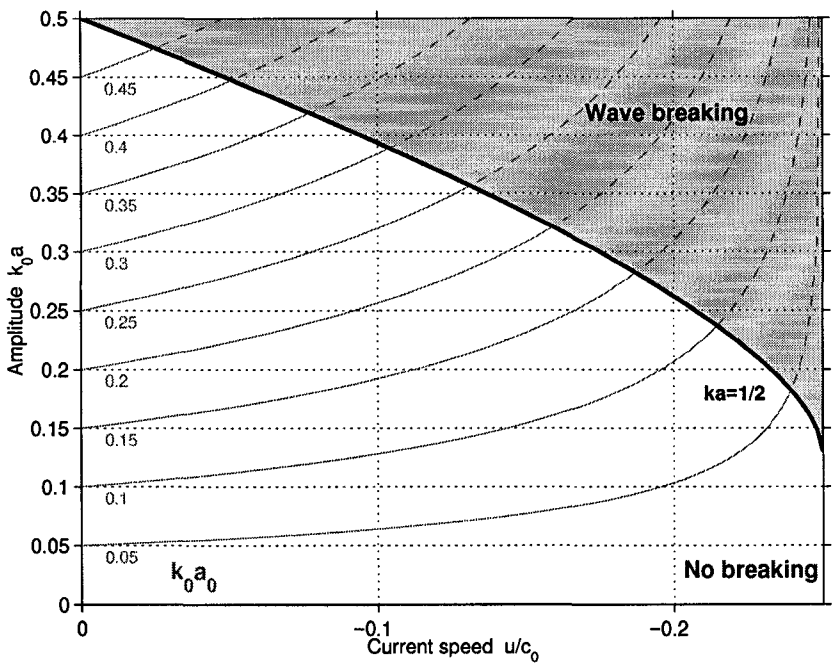

Figure 4.5: *The gray curves show the normalized amplitude of a wave of initial steepness* k_0a_0 *as a function of current speed. After the wave reaches the critical value of* $ka = 1/2$ *it is given by the black curve, or in the absence of breaking by the dashed gray curves.*

4.3.2 Continuous and intermittent breaking

In the previous chapter, the energy of a (breaking) monochromatic wave travelling on a current was calculated. However, for the prediction of size distributions of bubbles generated by wave breaking it is important to know how much energy is lost by breaking, how it is lost, and where.

There are different types of breaking waves (Galvin, 1968) depending on environmental conditions like wind, currents, or bathymetry:

- Spilling breakers occur when the wave slowly reaches its critical steepness. The wave becomes unstable at the top and the "excess height" is lost by breaking in form of a whitecap (Figure 4.6a), which then flows down the front face of the wave. This kind of wave breaking will be discussed below.
- Plunging breakers occur when the wave crest curls over the front face, plunges forward, and falls into the base of the wave enclosing some larger amount of air while breaking (Figure 4.6b). Most of the wave energy is dissipated by one short breaking event.
- Collapsing and surging breakers occur when the wave crest remains unbroken and the wave base advances up a steep beach.

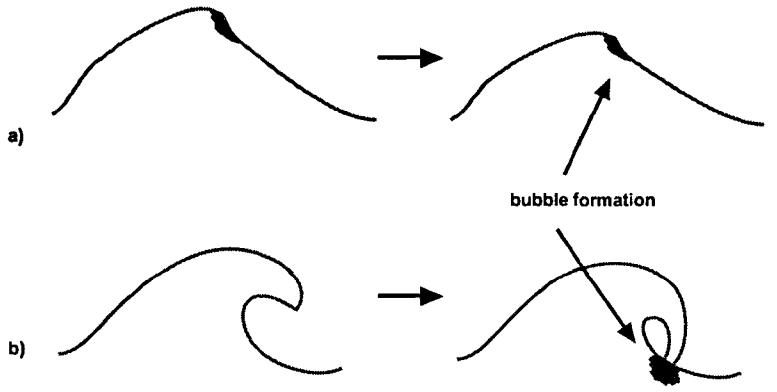

Figure 4.6: *Sketch of a) spilling breaker and b) plunging breaker.*

The following considerations will be limited to the case of spilling breakers by assuming that the currents change only slowly, although it is quite possible that waves with a small initial steepness break in a convergence zone as plunging breakers or some intermediate type of breaker. This is suggested by the gray curves in Figure 4.5 which show that the amplitude increases more quickly for waves with a small initial steepness as they reach their critical steepness than for waves with a high initial steepness.

Waves can either break continuously – i.e. for a period of time longer than the wave period – or intermittently – i.e. the wave breaks only for a short time without losing all its energy and breaks again at a later time. The energy distribution of a breaking wave will therefore be different for an intermittently or a continuously breaking wave. This affects the number of generated gas bubbles and the location where they are generated. To determine how a wave breaks, we will have to look at a group of waves rather than a single monochromatic wave. This will also tell us how much energy is dissipated by wave breaking.

Wave packet in an ocean an rest

First of all, let us consider a packet of wind generated deep water waves in an ocean at rest (Figure 4.7). At time $t = 0$, the first wave slightly exceeds the critical steepness of $ka = 1/2$ and breaks (see also Donelan *et al.* (1972)). One period later ($t = \tau$), this wave has travelled one wave length λ to the right while the shape of the wave packet has travelled $\lambda/2$ during the same time ($c_g = c/2$), i.e. the wave has travelled $\lambda/2$ relative to the packet. The steepness is therefore reduced, we assume to a value of $ka < 1/2$, and the wave does not break anymore.

At time $t = 2\tau$, the second wave has reached its critical steepness and breaks 2τ later than the first wave and one wave length to the right of the location at which the first wave was breaking.

However, this intermittent breaking can only occur if there is a continuous source of energy (e.g. wind) keeping the wave packet at the same amplitude. In the absence of an energy

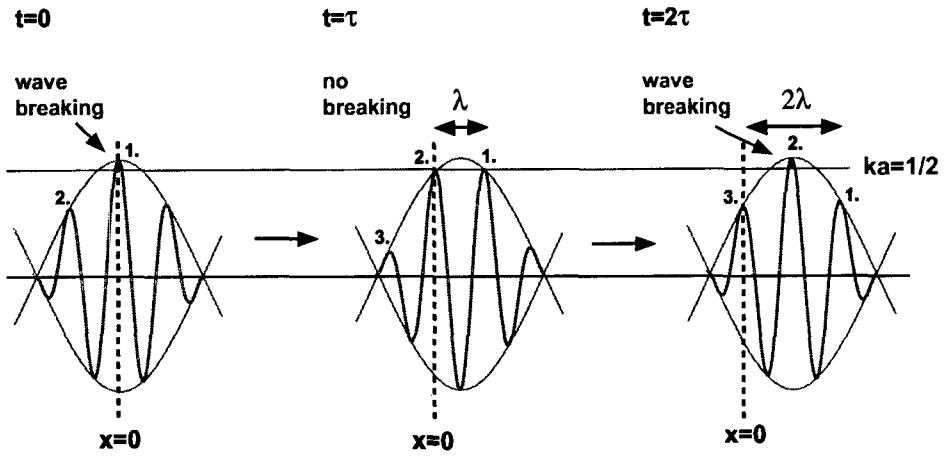

Figure 4.7: *Development of a wave packet of deep water waves in an ocean at rest for times $t=0$, $t=\tau$, and $t=2\tau$. Wave breaking occurs when the waves reach the critical steepness of $ka=1/2$.*

source, the shape of the wave packet would be altered by breaking in such a way that the waves might not reach the critical steepness anymore and would not break. Thus the waves would probably break a few times before the group decays.

Monochromatic wave on a current

With this in mind we can now look at the behaviour of a quasi-monochromatic wave on a current, i.e. a wave packet which consists for any current speed u/c_0 only of one monochromatic component. Although amplitude, wave number, and wave length change due to the effect of the currents, it can be treated as a monochromatic wave, if the current speed changes only little over a wave length.

For the calculation of energy dissipation by wave breaking, the shape of the wave packet has to be considered, as the wave energy is transported with the group speed c_g and not with the phase speed c. As already discussed, amplitude and wave number increase as the wave encounters an opposing current (energy given by Γ_1 in Figure 4.8) until it reaches its

critical steepness $ka = 1/2$ (curve Υ_1) and breaks. Γ_1 and Υ_1 mark the shape of the wave packet at time $t = 0$.

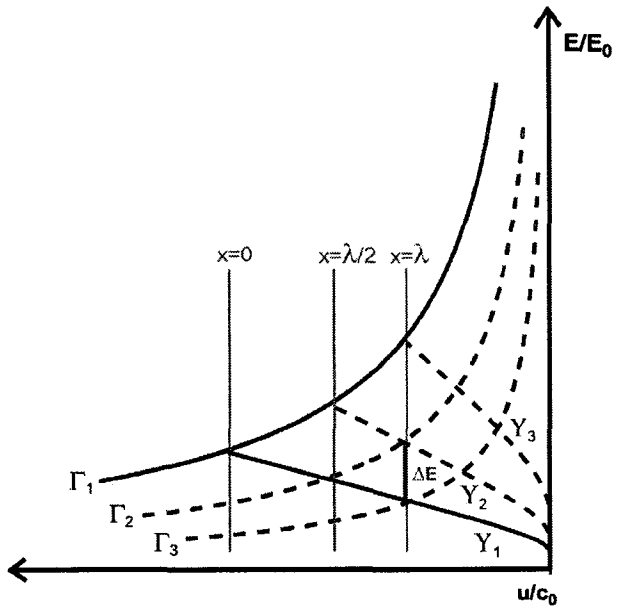

Figure 4.8: *Behaviour of a quasi-monochromatic wave on an opposing current for time $t = 0$ and $t = 2\tau$. The normalized energy is given for the case with breaking (red curves Υ_j) and without breaking (blue curves Γ_i).*

As the waves travel further against the opposing current (left to the right in Figure 4.8), their amplitudes would increase, if they were not reduced by breaking. The energy the waves would have had without breaking is given by the curves Γ_i, with $\Gamma_i/\Gamma_1 = \text{const}$. At the same time, also the shape of the wave packet would change as indicated by the curves Υ_j.

Let us now consider a wave which is at location $x = 0$ at time $t = 0$ (on curve Γ_1). One period τ later it has moved λ and the wave packet $\lambda/2$ to the right. Υ_2 indicates the shape of the wave packet at that time in the absence of breaking, so that the normalized energy of the wave is given by $\Upsilon_2(\lambda)$. But because of breaking, the "excess" energy $\Delta\hat{E} = \Upsilon_2(\lambda) - \Upsilon_1(\lambda)$ is

lost between $x=0$ and $x=\lambda$. From Figure 4.8 it also follows that $\Upsilon_2(\lambda)=\Gamma_2(\lambda)$. Together with

$$\frac{\Gamma_2(\lambda)}{\Gamma_1(\lambda)} = \frac{\Gamma_2(\lambda/2)}{\Gamma_1(\lambda/2)} = \text{const.}, \quad \text{and} \quad \Gamma_2(\lambda/2) = \Upsilon_1(\lambda/2) \tag{4.20}$$

we yield an equation for the energy loss by wave breaking

$$\Delta\hat{E} = \frac{\Upsilon_1(\lambda/2)\,\Gamma_1(\lambda)}{\Gamma_1(\lambda/2)} - \Upsilon_1(\lambda) \quad . \tag{4.21}$$

In these idealized conditions, the wave crest is continuously pushed into the region of critical steepness, so that the wave breaks continuously (and not intermittently) in order to satisfy the stability criteria. However, this is not necessarily true if the magnitude of the currents does not increase linearly or if we are looking at the more realistic case of a group of waves rather than a monochromatic wave train.

Wave packet on a current

Figure 4.9 shows a sketch of the break behaviour of a group of waves on a current. At $t=0$ (a), the first wave has a steepness of $ka > 1/2$ and breaks, which also changes the form of the wave packet (b). At $t=\tau$ (c), the first wave has moved $\lambda/2$ to the right (relative to the wave packet) so that its amplitude is reduced and has a steepness which is less than the critical value. It stops breaking. At $t=2\tau$ (d), the next wave has reached its critical steepness and breaks – with an amplitude which is smaller than the first wave. Because of the altered shape of the wave packet at a later stage (e), the waves are continuously pushed into the region of critical steepness and hence break continuously.

However, depending on the initial shape of the wave packet and the gradient in current speed, there might be no phase of intermittent breaking. It is also possible that the waves "overshoot" when they break, i.e. the amplitude is reduced more than necessary in order to satisfy the stability criteria, and break again when they are getting too steep. The energy loss is step-like instead of continuous.

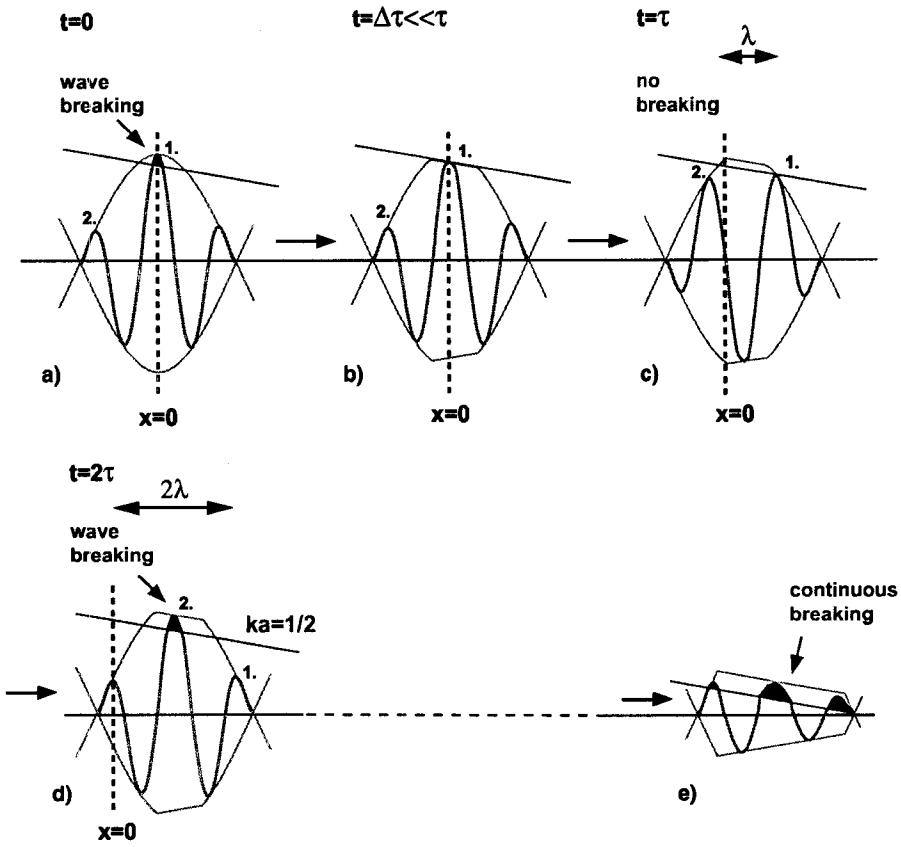

Figure 4.9: *Sketch of the break behaviour of a group of waves on a current. For explanations see text.*

Observations of breaking waves in tidal fronts (Figure 4.1) show, that most waves within the convergence zone are whitecaps, indicating that continous breaking is predominant.

4.4 Influence of wind

So far we have ignored the generation of waves. As this helps us to estimate the initial height of a wave before it encounters a current, a simple model for the generation of waves by wind will be introduced in this Section.

For the prediction of wave generation by wind, some sophisticated models have been pub-

lished. However, for estimating the expected range of waves in the study area, one of the first wind-wave models – the Sverdrup-Munk-Bretschneider (SMB) model (Bretschneider, 1958; Sverdrup & Munk, 1947) – is sufficient. It describes deep water waves under stationary conditions created by a homogeneous wind field.

The wave height depends on the wind speed u_* as well as on the fetch $\mathcal{F}$ (the distance over which the wind has blown) and duration t_* of the wind. The wave generation is limited by the fetch, if

$$\mathcal{F} < \mathcal{F}_{\text{lim}} = 0.015\,(\mathcal{S}\,g)^{1/2}\,t_*^{3/2} \quad , \tag{4.22}$$

where $\mathcal{S}$ is the wind stress factor given by $\mathcal{S}=0.71u_*^{1.23}$ and g the gravitational acceleration. u_* is given in $\mathrm{m\,s^{-1}}$, t in s, and $\mathcal{F}$ in m.
The significant wave height H_s, which is defined as the average height of the highest 1/3 of the waves, is calculated with

$$H_s = 1.6 \cdot 10^{-3}\,\mathcal{S}\left(\frac{\mathcal{F}}{g}\right)^{1/2} \quad . \tag{4.23}$$

The waves which travel into the tidal front at Boundary Pass are created by wind either in the Strait of Georgia or to the west of the front, in Boundary Pass (depending on the wind direction).

Figure 4.10a shows the limiting fetch $\mathcal{F}_{\text{lim}}$ plotted as function of wind speed and for different wind durations. The conditions in the Strait of Georgia are fetch-limited, if $\mathcal{F}_{\text{lim}}$ is bigger than the fetch in the Strait of Georgia ($\mathcal{F}<20\,\mathrm{km}$; gray box). This is only the case for low wind speeds or short wind durations.

In the Strait, the wind speed is usually less than $15\,\mathrm{m\,s^{-1}}$ (Figure 7.4). The corresponding wave height calculated with equation (4.23) for a fetch of 20 km is plotted in Figure 4.10b showing that the initial wave height reaches up to 1.5 m although is it usually less than 0.6 m as winds with $u_*<7\,\mathrm{m\,s^{-1}}$ prevail.

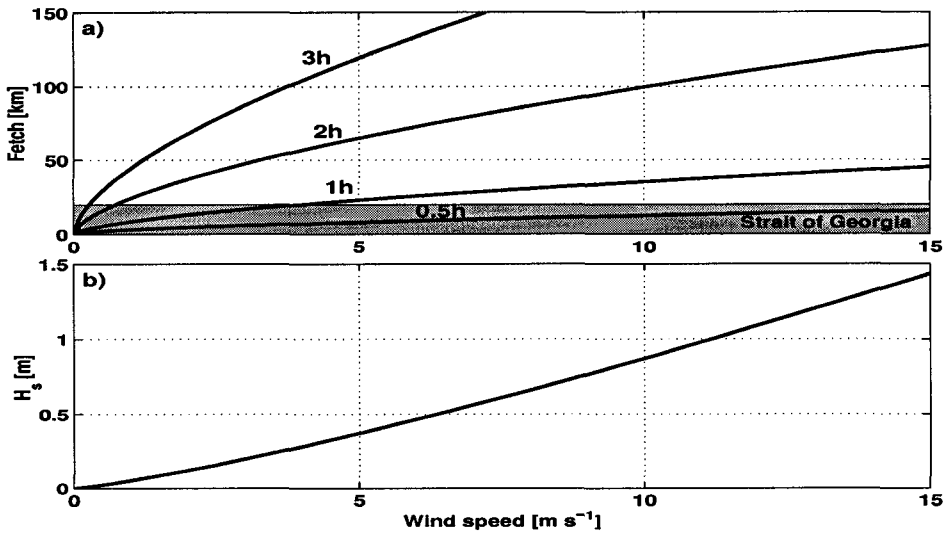

Figure 4.10: *a) Limiting fetch $\mathcal{F}_{\text{lim}}$ (equation 4.22) for a wind duration of 0.5 h, 1 h, 2 h, and 3 h. The fetch in the Strait of Georgia (20 km) is shown by the gray box. b) Significant wave height H_s for a fetch $\mathcal{F} = 20$ km.*

4.5 Bubble injection by breaking waves

We have seen that a wave encountering an opposing current steepens and finally breaks when it reaches its critical steepness. The energy which is lost during wave breaking goes into turbulence and the generation of gas bubbles. The size distribution of these bubbles, their injection depth, and the location where the wave breaks are important parameters for quantifying the air-sea gas exchange in tidal fronts and will therefore be studied in this section.

A certain percentage of energy lost by wave breaking goes into the subduction of newly formed gas bubbles as suggested by observations of open ocean whitecaps by Thorpe (1982), Vagle (1989), and Crawford & Farmer (1987) showing that the overall number of bubbles and their penetration depth increases with wind speed and hence with wave height/energy. By linking this energy to a general description of the bubble size distribution as a function of depth and bubble radius, we can finally derive the total number of bubbles as a function

of energy loss by breaking waves. This directly yields the void fraction, which is defined as the volume ratio of undissolved air to water. It is an important parameter for determining the amount of air which is transfered into the ocean.

General equations

Bubbles are formed by a breaking wave by two different mechanisms: by a jet of water which forms as the wave curls over and plunges into the sea surface, and by enclosing a pocket of air, which quickly breaks up into gas bubbles due to pressure fluctuation exerted by turbulence (the time scale of bubble formation is $< 90\,\mathrm{ms}$; Deane & Stokes (1999)). These bubbles of different radii r form a size distribution $N(r)$, which describes the number density of gas bubbles in a unit volume of water for each radius increment $r{-}dr/2$ to $r{+}dr/2$ between the cut-off radii r_1 and r_2, where $r_1 < r_2$.

Numerous measurements (for a list of references see Table 4.1) have shown that the size distribution of gas bubbles can be adequately described by a power law of the form

$$N(r) = \beta r^{\alpha} \quad , \tag{4.24}$$

where β is a scaling factor which depends on the total number of bubbles. α is the slope of the size distribution (in double-logarithmic space) and has negative values as small bubbles are more numerous than big bubbles.

The number of gas bubbles per unit volume decreases with depth. It has been suggested by various authors (Table 4.1) that this decay is exponential, so that the bubble size distribution can be described as a function of depth z and radius r as

$$N(r,z) = \beta_0 r^{\alpha} e^{z/\gamma} \quad , \tag{4.25}$$

where γ is the entrainment depth of the gas bubbles ($z = 0$ at the surface, with negative

values downwards) and β_0 is the scaling factor at the sea surface. As discussed below it is assumed that the slope α is constant with depth.

A wave loses a certain amount of energy E_w during breaking. Part of this energy E_b goes into the subduction of gas bubbles. Their ratio $\mathcal{E}$ is given by

$$\frac{E_b}{E_w} \equiv \mathcal{E} \quad . \tag{4.26}$$

The energy required to submerge a single bubble of radius r is

$$E_{b1} = -\frac{4}{3}\pi r^3 \rho g z \quad , \tag{4.27}$$

where ρ is the water density, which can be considered to be constant here as variations in density have a negligible effect on the buoyancy of gas bubbles. This yields the energy, which is required to submerge all bubbles of a size distribution $N(r,z)$, by integrating between the cut-off radii r_1 and r_2 and over the whole water column

$$E_b = -\int_{-\infty}^{0}\int_{r_1}^{r_2} N(r,z)\frac{4}{3}\pi r^3 \rho g z \, dr \, dz \quad . \tag{4.28}$$

If we insert the equation for the size distribution (4.25), we obtain

$$E_b = -\frac{4}{3}\pi \rho g \beta_0 \int_{-\infty}^{0} z\, e^{z/\gamma}\, dz \int_{r_1}^{r_2} r^{\alpha+3}\, dr \quad . \tag{4.29}$$

Reference	Type	u_* [m/s]	H_s [cm]	z/H_s	r [μm]	$-\alpha$	γ [cm]	void fr.
Baldy & Bourguel (1987)	tank	14	9.2-23.8	< 0.5 1-2.5	60-3000	2-2.3 4	1.3	–
Baldy (1988)	tank	14	–	0.25 2.5	60-3000	2.5 3.9	~ 3	–
Crawford & Farmer (1987)	obs.	3-11	–	–	58-250	4	70-150	–
Deane (1997)	obs.	3-5	90	< 0.55	300-1000 > 1000	2.5 4.5	–	0.3-0.4
Deane & Stokes (1999)	obs.	–	–	(5cm)	200-1000 > 1000	2.5 4.5	–	–
Deane & Stokes (2002)	tank	–	10	–	50-1000 > 1000	3/2 10/3	–	–
	obs.	7-10	250-350	~ 0.1	250-1000 > 1000	1.8-2.9 4.9-5.5	–	–
Garrett *et al.* (2000)	theory	–	–	–	–	10/3	–	–
Hwang *et al.* (1990)	tank	10-15	8-11	0.5-1.2 1.2-2.1	800-3000	$2.8z/H_s$+0.7 4	$\sim H_s$	–
Johnson & Cooke (1979)	obs.	8-13	~ 200	~ 0.75	51-128	4.5	–	–
Lamarre & Melville (1994)	tank	–	> 50	< 1.2	–	–	$< 0.35\,H_s$	0.003-0.54
Loewen *et al.* (1996)	tank	–	–	(0-6cm)	200-5000	3.7	1	$1.5\text{-}2.6\cdot10^{-3}$
Medwin (1970)	obs.	–	–	(2-15m)	18-60 60-180	4 2	500-900 $(z^{-1/2})$	–
Medwin (1977*a*)	obs.	3.3-6.1	–	(4m)	15-50 50-300	4-4.5 2-2.3	–	–
Medwin & Breitz (1989)	obs.	12-15	260	0.18	30-50 60-240	4 2.6	–	–
Vagle (1989)	obs.	4-15	–	(0.1-15m)	20-152	3.3-6	–	–
Vagle (2001)	obs.	–	30-100	3-20	18-250	2.7	–	–
Wu (1981)	lit.	6-13	–	(3-9m)	17-176	0-3.5 3.5-5	100 $(0.9z^{-2.6})$	–

Table 4.1: *Important parameters from the literature for bubble entrainment by breaking waves: type of study (obs.=observations), wind speed u_*, significant wave height H_s, normalized depth of measurement z/H_s (values in brackets are absolute values), range of radii r, spectral slope $-\alpha$, entrainment depth γ (other than exponential depth dependences are given in brackets), and void fraction.*

The integrals in this equation are

$$\int_{-\infty}^{0} z\, e^{z/\gamma}\, dz = -\gamma^2 \quad , \tag{4.30}$$

$$\text{and} \quad \int_{r_1}^{r_2} r^{\alpha+3}\, dr = \frac{1}{\alpha+4}\left[r_2^{\alpha+4} - r_1^{\alpha+4}\right] \quad \text{for} \quad \alpha \neq -4 \quad ,$$

$$= \ln \frac{r_2}{r_1} \quad \text{for} \quad \alpha = -4 \quad , \tag{4.31}$$

so that the equation for the energy which goes into the subduction of gas bubbles E_b (4.29) can be rewritten as

$$E_b = \frac{4\pi\rho g \beta_0 \gamma^2}{3(\alpha+4)}\left[r_2^{(\alpha+4)} - r_1^{(\alpha+4)}\right] \quad \text{for} \quad \alpha \neq -4 \quad ,$$

$$= \frac{4}{3}\pi\rho g \beta_0 \gamma^2 \ln \frac{r_2}{r_1} \quad \text{for} \quad \alpha = -4 \quad . \tag{4.32}$$

By combining this equation with the one for the energy ratio $\mathcal{E}$ (4.26) this finally yields a solution for the scaling factor β_0 which describes the total number of gas bubbles at the sea surface (for simplicity we ignore the case $\alpha = -4$ for now)

$$\beta_0(x) = \frac{3(\alpha+4)\mathcal{E} E_w(x)}{4\pi g \rho \gamma^2}\left[r_2^{\alpha+4} - r_1^{\alpha+4}\right]^{-1} \quad . \tag{4.33}$$

In a convergence zone, the energy loss by wave breaking E_w is a function of horizontal distance x, because the current speed changes and therefore also the amplitude of the wave. Hence, the size distribution of new bubbles injected is a function of horizontal and vertical distance

$$N(x, z, r) = \beta_0(x) e^{z/\gamma(x)} r^{\alpha} \quad . \tag{4.34}$$

Calculation of scaling factor β_0

To calculate the scaling factor $\beta_0(x)$, the values for the slope of the size distribution α (with the corresponding cut-off radii r_1 and r_2), the bubble entrainment depth γ, and the portion of energy which goes into the subduction of bubbles $\mathcal{E}$ are taken from the literature and will be discussed in the following. The density $\rho = 1023.5\,\mathrm{kg\,m^{-3}}$ is derived from measurements and $E_w(x)$ is calculated with the model of wave-current interaction introduced at the beginning of this section.

The slope of the bubble size distribution α has been subject of numerous publications (Table 4.1) with values ranging between -1.8 and -5.5. Unfortunately it is difficult to compare these measurements as they were taken in different environments (tank, surf zone, open ocean), different wind and wave conditions (spilling or plunging breakers), measurement depths, or at different times relative to the time of initial bubble generation (plume age). Also surfactants may influence the spectral slope.

The bubble size distribution changes with time due to the effects of dissolution which flattens the spectrum for small bubbles and buoyancy which steepens the spectrum for larger bubbles (Garrett *et al.*, 2000). This was, for example, observed by Baldy & Bourguel (1987) as well as Baldy (1988), who found a bubble generation zone at the surface and a depletion zone beneath it, with spectral slopes increasing with depth as buoyancy becomes more important (see also Hwang *et al.* (1990)).

For our considerations, i.e. the calculation of the scaling factor β_0 and the subsequent modeling of bubble behaviour (Section 5), we are interested in the initial bubble size distribution. It is defined as the size distribution which is established immediately after bubble formation and before it is altered by buoyancy or dissolution (the time scale for bubble injection and formation is short in comparison to those for dissolution and buoyancy (Garrett *et al.*, 2000)).

Measurements during CCGS Vector cruises 9914 and 0032 (Section 2) were taken at some depth well below the sea surface ($z > 10\,\mathrm{m}$) and can therefore not be used for describing

the initial bubble size distribution at the surface. As it is also difficult to find a suitable value for α from the literature, we adapt the theoretical considerations from Garrett *et al.* (2000), who argue on dimensional grounds that the bubble breakup by turbulence results in an initial bubble size distribution $N(r)$ which is proportional to $r^{-10/3}$. After this initial bubble formation, surface tension prevents further bubble breakup, so that their number only changes when a bubble completely dissolves or when it rises back to the surface.

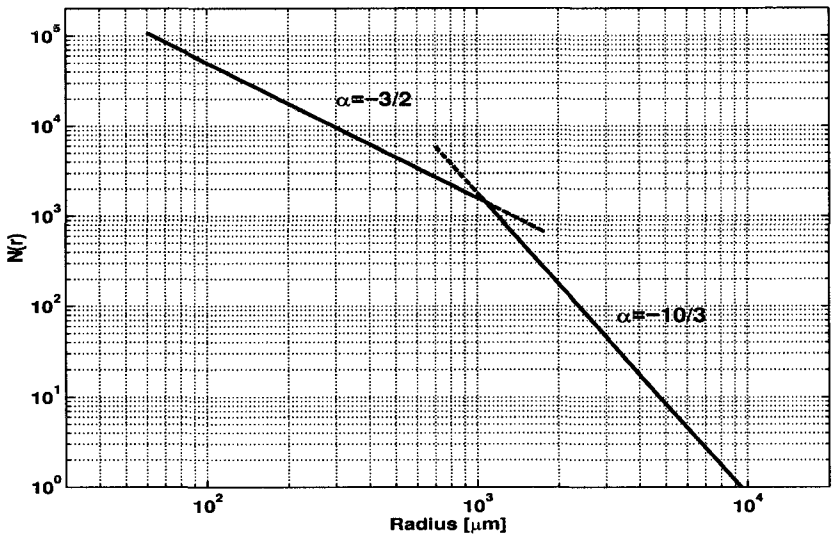

Figure 4.11: *Sketch of the initial bubble size distribution (Garrett* et al. *(2000); Deane & Stokes (2002)).*

A spectral slope of $\alpha = -10/3$ was also observed by Deane & Stokes (2002) for bubbles with radii $> 1000\,\mu$m generated in the surf zone. For $r < 1000\,\mu$m the slope was $\alpha = -3/2$, which is supported by dimensional considerations for bubble entrainment by a jet of water. This implies that most of the small bubbles are formed when the wave curls over and plunges into the sea surface. Although this scenario seems to be more likely for plunging than for spilling breakers and the separation point between both slopes may not be constant under different conditions, we will use the following description for the initial bubble size distribution due

to the lack of measurements in more suitable conditions

$$\begin{aligned} \alpha &= -3/2 \quad \text{for} \quad r \leq 1000\,\mu\text{m} \quad , \\ \alpha &= -10/3 \quad \text{for} \quad r > 1000\,\mu\text{m} \quad . \end{aligned} \tag{4.35}$$

The resulting bubble size distribution is plotted in (Figure 4.11).

The spectral slope α is considered to be invariant with depth. However, the overall number of gas bubbles decreases with depth and is described by the bubble entrainment depth γ (see Equation 4.25).

It seems plausible that γ depends on the amplitude a of a breaking wave: the higher the wave, the greater the bubble penetration depth. We have seen that the wave energy is proportional to a^2 (Equation 4.7) and that a portion of this energy goes into the subduction of bubbles when the wave breaks. As this energy E_b is proportional to γ^2, the bubble penetration depth γ is likely to be proportional to the wave height a.

This is supported by tank experiments by Chanson & Jaw-Fang (1979), which showed that bubbles injected by a jet or plunging breaker penetrate to a depth of about 1.2–2 times the wave amplitude. These values are slightly higher than the ones by Hwang *et al.* (1990), who found a quasi-linear relationship between significant wave height and bubble penetration depth ($\gamma \approx H_s$) for waves generated in a tank ($H_s = 0.08 - 0.11$ m). Loewen *et al.* (1996) measured in a tank $\gamma = 0.11 - 0.34a$, and Thorpe (1986) observed bubbles in the ocean to depths of $2.5 - 3H_s$ for moderate winds and $4 - 5H_s$ for strong winds.

These entrainment depth may overestimate the initial entrainment depth as bubbles are carried further down by wave motion or vertical currents associated with Langmuir circulations. As discussed at the end of this Section a value of $\gamma = a/4$ seems to be a suitable value for small spilling breakers.

Measurements of breaking waves show that between 10% and 60% of the wave energy is lost during breaking (Table 4.2). The portion of this energy which goes into the subduction

of gas bubbles is given as $1.5-4.2 \cdot 10^{-3}$ for small spilling breakers (Loewen *et al.*, 1996) or as high as $0.3-0.5$ for small plunging breakers (Lamarre & Melville, 1991).

The appropriate value for a breaking wave on a current is therefore quite uncertain and varies over at least one order of magnitude. It is likely that it depends on the current speed gradient a wave experiences: a sudden current change may result in a plunging breaker, while a gradual change in current speed results in a spilling breaker. For now, we will assume that the ratio $\mathcal{E}$ of energy which goes into the subduction of bubbles to the energy lost by wave breaking is $3 \cdot 10^{-3}$, as for a spilling breaker. However, this value will be discussed in more detail in Section 6.

Reference	Type	E_w/E [%]	E_w [Jm^{-1}]	$\mathcal{E}$
Chanson & Jaw-Fang (1979)	tank	20-60	–	–
Melville & Rapp (1985)	tank	10 [1)], 20-30 [2)]	–	–
Nepf *et al.* (1998)	tank	10-22	–	–
Lamarre & Melville (1991)	tank	< 40	4.3-17.8	0.3-0.5
Loewen *et al.* (1996)	tank	10-25 [1)]	0.48-0.52	$1.5\text{-}4.2 \cdot 10^{-3}$

Table 4.2: *Estimates of energy loss of breaking waves from the literature.* [1)] *Single break event;* [2)] *multiple break events.*

The void fraction is the volume fraction of undissolved air in water and is given by the integral over all gas bubbles in a given volume

$$\mathcal{V}(x,z) = \int_{r_1}^{r_2} \frac{4}{3}\pi r^3 N(x,z,r)\, dr = \frac{4}{3}\pi \int_{r_1}^{r_2} \beta r^{(3+\alpha)} e^{(z/\gamma)}\, dr \quad . \tag{4.36}$$

The calculated value for $\mathcal{V}$ depends on the cut-off radii r_1 and r_2 – the radii of the smallest and biggest bubbles detected by measurements. $\mathcal{V}$ is underestimated, if a part of the bubble spectrum is not detected. The significance of this error depends on the spectral slope of the

bubble size distribution. For $\alpha > -4$, the void fraction is mainly determined by large bubbles and for slopes of $\alpha < -4$ it is determined by small bubbles, which means for example that the cut-off radius for large bubbles r_2 is not critical if $\alpha < -4$, but is significant if $\alpha > -4$.

For our bubble spectrum (4.35), this means that the cut-off radius r_1 for small bubbles is not critical as the spectral slope is $\alpha = -3/2 > -4$. The cut-off radius for big bubbles r_2, however, is important for calculating gas entrained by bubbles as $\alpha = -10/3 > -4$. Hence, the void fraction is dominated by the bigger bubbles. For comparing our model calculations with the measurements published in literature, the values $r_1 = 20\,\mu$m and $r_2 = 10\,000\,\mu$m are chosen covering the whole measurement range of bubble radii.

To summarize: for the calculation of the scaling factor β_0 (Equation 4.33) the following parameter values are taken from the literature: $\alpha = -3/2$ for $r \leq 1000\,\mu$m, $\alpha = -10/3$ for $r > 1000\,\mu$m, $\gamma = 1/4a$, $\mathcal{E} = 0.003$, $r_1 = 20\,\mu$m, and $r_2 = 10\,000\,\mu$m. The density $\rho = 1023.5\,\mathrm{kg\,m^{-3}}$ is derived from measurements.

These values will be applied to a model of wave breaking in a convergence zone as shown below in an example, and in the next Section, a model for the behaviour of gas bubbles after their initial injection due to the effects of dissolution, buoyancy, and vertical currents will be derived.

Example

As an example of bubble generation by a wave breaking on a current, let us consider a wave of initial amplitude $a_0 = 0.04\,$m and wave length $\lambda_0 = 0.6\,$m, which travels into a linearly increasing opposing current given by $u = 0$ for $x \leq 0$ and $u = m\,x$ ($m = -0.01\,\mathrm{s^{-1}}$) for $x > 0$ (Figure 4.12a). The other parameter values used in the calculations are (as discussed above): $\mathcal{E} = 0.003$, $\alpha = -3/2$ for $r \leq 1000\,\mu$m, $\alpha = -10/3$ for $r > 1000\,\mu$m, $r_1 = 20\,\mu$m, and $r_2 = 10\,000\,\mu$m.

The wave steepens as the opposing current increases, reaching its critical steepness at

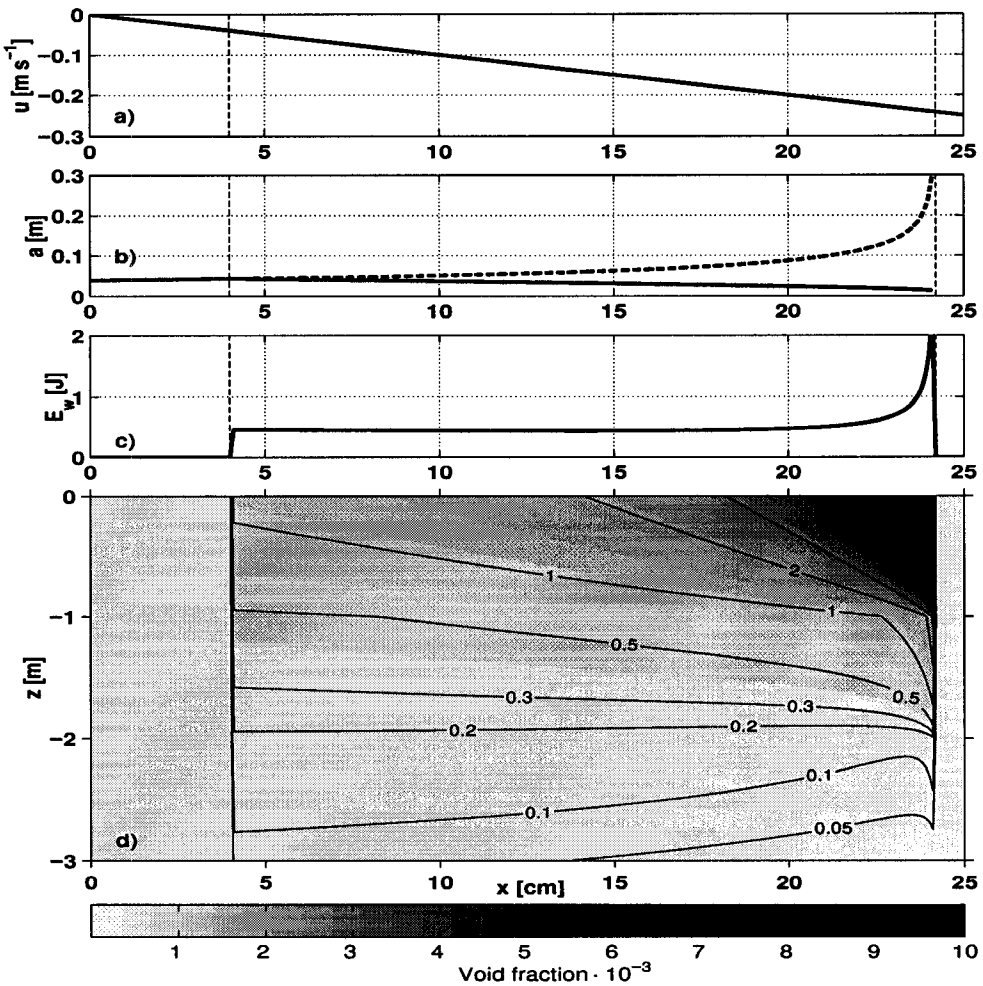

Figure 4.12: *Example of a wave travelling from left to right into a linearly increasing current. a) Current speed; b) wave amplitude with breaking (solid line) and without breaking (dashed line); c) wave energy lost by breaking; d) void fraction of initially injected bubbles.*

$x = 4$ m. From then on, the amplitude is reduced by wave breaking (Figure 4.12b), which is associated with a loss of energy (Figure 4.12c) calculated with equation (4.21). Part of this energy goes into the subduction of gas bubbles, which yields the initial void fraction shown in Figure 4.12d.

These settings are quite comparable to the measurements by Loewen *et al.* (1996), who

found an energy loss by wave breaking of about $0.5\,\mathrm{J\,m^{-1}}$ for spilling breakers of amplitude $a = 2.7 - 8.2\,\mathrm{cm}$. The measured entrainment depth was $\gamma = 0.94\,\mathrm{cm}$ or $\gamma = 0.11 - 0.34a$. Calculations with $\gamma = 0.25a$ yield a void fraction and bubble size distribution (for bubbles with $r > 800\,\mu\mathrm{m}$), which are very similar to the ones derived from the measurements. A entrainment depth $\gamma = a$ for example would yield results which are 16 times smaller than the observations, suggesting that $\gamma = 1/4a$ is a suitable description for the entrainment depth for small spilling breakers. However, it should be kept in mind that the break mechanism of the measurements was a different one ("shore break" in a tank rather than breaking on a current).

Nevertheless, this example shows that the calculated energy dissipation and bubble size distribution are in the right order of magnitude. The uncertainties which arise from errors in determining parameters like bubble entrainment depth or the amount of energy, which goes into the subduction of bubbles, will be discussed in Section 6.2.

5 Model for the behaviour of gas bubbles in a fluid

Gas bubbles are injected into the ocean by breaking waves and rise back to the sea surface due to their buoyancy, or may be pulled further down in the presence of strong downwelling currents. The volume of the bubble decreases with increasing hydrostatic pressure and by dissolution of gas from the bubble into the surrounding water. This decrease in volume has a direct effect on the buoyancy of the bubble and its rise speed.

This behaviour of a gas bubble in a fluid is described in this section with a one-dimensional model from Thorpe (1982). The model is applicable even to the highly complicated flow structure in tidal fronts by calculating the change of gas content and bubble radius along the path of the bubble.

As before, it is assumed that the gas bubbles do not break up any further after they have been injected, so that the size of the bubbles only changes due to dissolution and pressure changes. In addition, bubble-bubble interactions are neglected.

Tidal fronts are usually characterized by high turbulence, which also effects the behaviour of gas bubbles in the frontal zone. Its implementation into the model is described below.

5.1 Model equations

The total pressure P in a gas bubble is given by the sum of atmospheric pressure at the sea surface p_{atm}, the hydrostatic pressure $p=-\rho g z$, and the surface tension of the bubble

$$P = p_{atm} + p + \frac{2\gamma}{r} \quad , \tag{5.1}$$

where γ is the surface tension coefficient and r the radius of the bubble. Gas bubbles usually contain a mixture of different gases j. The sum of the partial pressure of the single gases P_j equals the total pressure according to Dalton's law $P = \sum_j P_j$. It is directly related to the mole fraction of the gas χ_j by $P_j = \chi_j P$, so that the ideal gas law is given by $\chi_j PV = n_j RT$, where $V = (4/3)\pi r^3$ is volume, T temperature in Kelvin (considered to be constant), R the universal gas constant, n_j the number of moles, and $\sum_j \chi_j = 1$. The time derivative of the ideal gas law (see also Merlivat & Memery (1983)) is

$$\frac{dn_j}{dt} = \frac{4\pi r^2}{3RT}\left(rP\frac{d\chi_j}{dt} + r\chi_j\frac{dP}{dt} + 3\chi_j P\frac{dr}{dt}\right) \quad . \tag{5.2}$$

If the sum over all gases $\sum_j dn_j/dt$ is combined with the time derivative of the expression for the total pressure (Equation 5.1)

$$\frac{dP}{dt} = \frac{dp}{dt} - \frac{2\gamma}{r^2}\frac{dr}{dt} \quad , \tag{5.3}$$

we get a differential equation for the bubble radius

$$\frac{dr}{dt} = \left[\frac{3RT}{4\pi r^2}\sum_j \frac{dn_j}{dt} - r\frac{dp}{dt}\right]\left(3p + 3p_{atm} + \frac{4\gamma}{r}\right)^{-1} \quad . \tag{5.4}$$

The diffusive gas exchange between bubble and water is driven by the difference between the partial pressure of gas in the bubble P_j and in the water far from the bubble $P_{w_j} = (1+0.01\sigma_j)\,\chi_j\, p_{atm}$, yielding (Thorpe, 1982, 1984)

$$\frac{dn_j}{dt} = -4\,\pi\, r\, D_j\, S_j\, Nu_j\,(\chi_j P - P_{w_j}) \quad . \tag{5.5}$$

σ_j, D_j, χ_j, S_j, and Nu_j are the percentage oversaturation of gas in water, the coefficient of diffusion, the mole fraction in dry air, the solubility, and the Nusselt number.

The gas transfer from the bubbles into the water is enhanced by the flow relative to the bubble (by the bubble rise speed w_b or turbulence). The Nusselt number Nu is a dimensionless measure of gas transfer and is given by the ratio of the total gas exchange and the gas exchange caused by diffusion alone and is calculated with the following formulas (Woolf & Thorpe, 1991)

$$\begin{aligned} Nu &= 1.292\, Pe^{1/9} && \text{for} && Pe < 24.17 \quad , \\ Nu &= 2/\pi\, Pe^{1/3} && \text{for} && Pe \geqq 24.17 \quad \text{and} \quad Re < 8.017 \quad , \\ Nu &= 0.45\, Re^{1/6} Pe^{1/3} && \text{for} && Pe \geqq 24.17 \quad \text{and} \quad Re \geqq 8.017 \quad , \end{aligned} \tag{5.6}$$

where the Peclet number is defined as $Pe = r\, w_b\, D_j^{-1}$, and the bubble Reynolds number as $Re = 2\, w_b\, r \nu^{-1}$. ν is the water kinematic viscosity.

By combining equations (5.1), (5.4), and (5.5), the change of radius r with time t can be finally written as

$$\frac{dr}{dt} = -\left[\frac{3RT}{r}\sum_j D_j\, S_j\, Nu_j \left(\chi_j \left(p + p_{atm} + \frac{2\gamma}{r}\right) - P_{w_j}\right) + r\frac{dp}{dt}\right]\left(3p + 3p_{atm} + \frac{4\gamma}{r}\right)^{-1} \quad . \tag{5.7}$$

The change of the hydrostatic pressure dp/dt in this equation is determined by the sum of the vertical current speed w, the rise speed of the gas bubble w_b (see next section), and the turbulent current speed w_{turb}

$$\frac{dp}{dt} = g\,\rho\,(-w - w_b + w_{turb}) \quad . \tag{5.8}$$

Bubble rise speed

Gas bubbles rise in a fluid due to their buoyancy. The rise speed is significantly affected by surface-active material which is absorbed into their surface. Bubbles with such a layer of surfactants are called dirty bubbles or, if they do not have such a layer, clean bubbles.

In the ocean or other natural bodies of water, gas bubbles can be considered to be dirty bubbles (Thorpe, 1982). Formulae for their rise speed are given by various authors (Thorpe, 1982; Woolf & Thorpe, 1991; Keeling, 1993). In the following, the description from Fan & Tsuchiya (1990) is used. In figure 2.10 of their book, they merged the results from different studies covering a wider range of radii. This figure is redrawn here (Figure 5.1) and is used to determine the rise speed of a bubble as function of its radius.

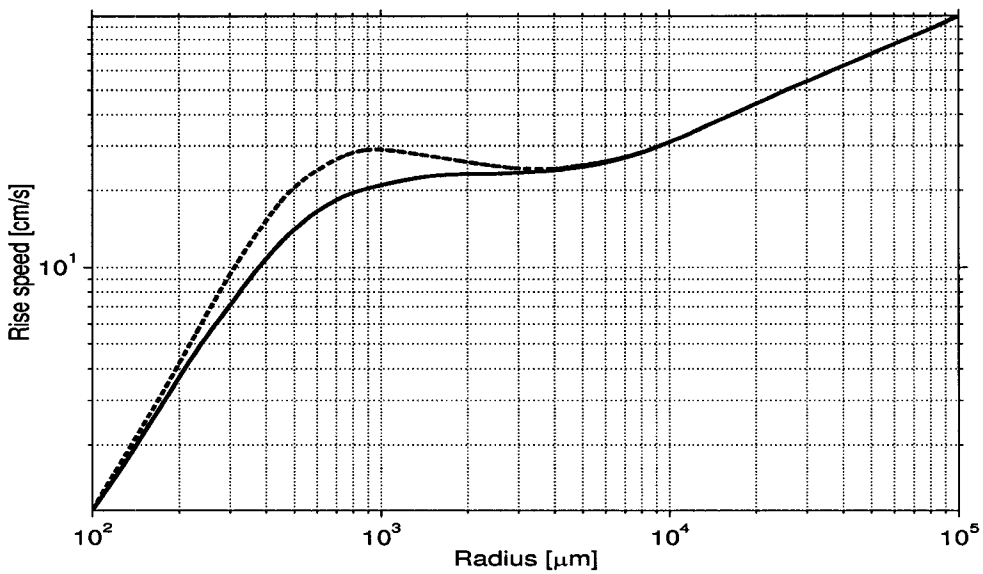

Figure 5.1: *Rise speed w_b of dirty (solid line) and clean (dashed line) gas bubbles.*

The pressure effect on the rise speed is only about 10% for a pressure as high as 19.4 MPa (Fan *et al.*, 1999) and the effect of density changes in the water column is smaller than 1% and can therefore be ignored.

Solving the equations

The coupled ordinary differential equations (5.7) and (5.8) were solved with an explicit Runge-Kutta formula in MATLAB. This one-step solver only needs the solution at the

immediately preceding time point, so that the vertical current speed can be described by an arbitrary function of time and also turbulence can be implemented in the model.

Turbulence is described by using typical scales for the vertical current speed $w^* = 0.05\,\mathrm{m\,s^{-1}}$ and for the vertical displacement of a parcel of water due to turbulence $z^* = 3\,\mathrm{m}$. These were estimated from observations in a similar environment of a tidal front in Haro Strait (Gargett & Moum, 1995). These values were multiplied with a random value chosen from a normal distribution with mean zero and standard deviation one, yielding the turbulent vertical current speed w_{turb} which is used in equation (5.8). The increased gas flux due to small scale pressure fluctuations is incorporated in the description of the Nusselt Number (Equation 5.6).

For the model calculations, the gas mixture in the bubbles contains the four gases O_2, N_2, CO_2, and Ar (indices $j = 1, 2, 3, 4$ in equation (5.7)). It is assumed that the injection time of the bubbles is short in comparison to the time scale of diffusion, so that the initial molefraction χ_j at time $t = 0$ is equivalent to the one in the atmosphere. Later, the molefraction (and gas content) changes due to diffusion and one of the gases may go completely into solution while others are still present. Typical parameter values (Woolf & Thorpe, 1991), used in the model runs, are listed in Table 5.1.

5.2 Model application

The bubble model described above provides a useful tool for the interpretation of our bubble measurements. In the following, two examples of how it can be applied to echo sounder or acoustical resonator observations are shown.

Echo sounder measurements

Most of the high acoustic backscatter intensity within the water column measured with an echo sounder can be attributed to gas bubbles (Section 2.1). The echo sounder can only detect bubbles with a radius equivalent to the resonance radius r_{res}, which is primarily

Variable	Symbol	Values for				Units
		O_2	N_2	CO_2	Ar	
Coeff. of diffusion	D_j	1.7	1.8	1.3	1.7	$10^{-9}\,\mathrm{m^2\,s^{-1}}$
Molefraction in dry air	χ_j	209.5	780.9	0.0035	9.2	10^{-3}
Solubility	S_j	13	6.29	445	14.2	$10^{-6}\mathrm{mol\,m^{-1}Pa^{-1}}$
Water oversaturation	σ_j	0	0	0	0	%
Temperature	T	283				K
Density of sea water	ρ	1020				$\mathrm{kg\,m^{-3}}$
Atm. surface pressure	p_{atm}	$1 \cdot 10^5$				Pa
Surface tension coeff.	γ	0.036				$\mathrm{N\,m^{-1}}$
Water kin. viscosity	ν	$1 \cdot 10^{-6}$				$\mathrm{m^2\,s^{-1}}$
Turb. length scale	z^*	3				m
Turb. current scale	w^*	0.05				$\mathrm{m\,s^{-1}}$

Table 5.1: *Typical values for the parameters used in the model calculations.*

determined by pressure (depth) and the frequency f of the instrument (here 100 kHz). It is given to a good approximation by Medwin (1977*a*)

$$r_{res} \approx 3.25 \cdot 10^6 \frac{1}{f}\sqrt{1 + 0.1\,z} \quad , \tag{5.9}$$

and is plotted in Figure 5.2. The frequency is given in Hz, the depth in m, and the bubble radius in μm.

The strength of the measured signal yields the number of bubbles of that particular radius r_{res}. However, because the echo sounder was not calibrated during the experiment, this information does not provide any relative quantitative information.

The gas bubbles which are detected by the echo sounder (Figure 5.2) were injected into the ocean by breaking waves somewhere close to the sea surface. Based on the sounder measurements and some assumption of the vertical current speed, the bubble model can

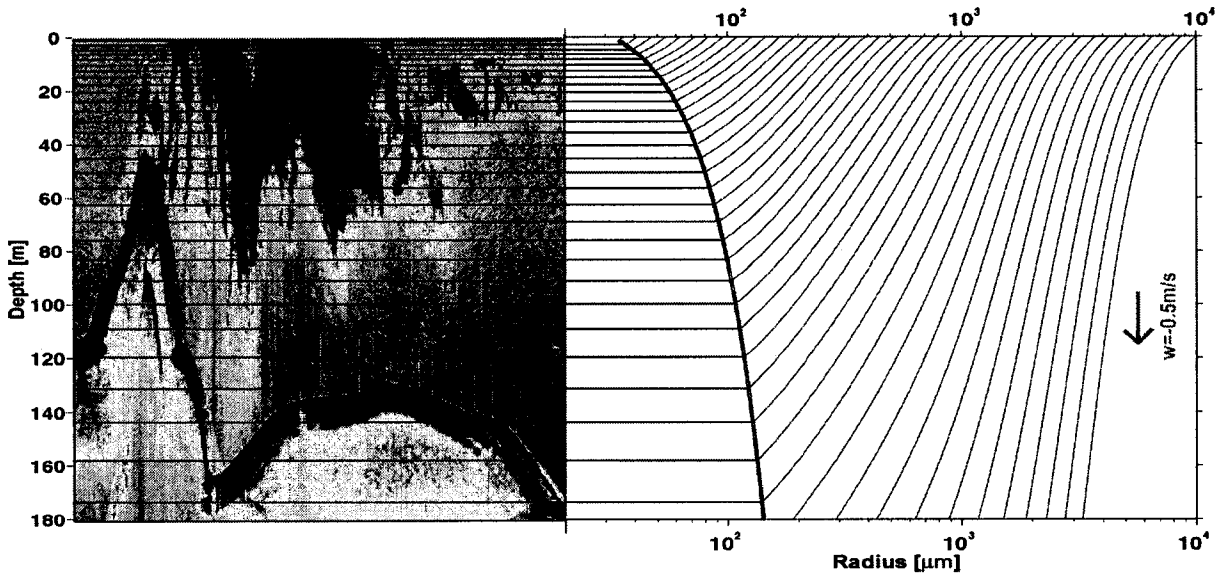

Figure 5.2: *The color image shows acoustic backscatter intensity measured with a 100 kHz echo sounder on September 24, 2000, at Boundary Pass. The corresponding resonance radius is indicated by the red curve and the blue lines show the "path" of the injected bubbles for a vertical current speed of* $-0.5\,\mathrm{m\,s^{-1}}$.

be used to calculate the size these bubbles had right after their initial injection. This information is important for estimating the amount of air which is entrained into the ocean in form of gas bubbles.

A model run with a constant vertical current speed $w = -0.5\,\mathrm{m\,s^{-1}}$ and no turbulence was carried out for different initial bubble sizes. The radii of the bubbles are shown as a function of depth in Figure 5.2 by the blue lines. For back-tracing a bubble from the depth of measurement to the surface, the appropriate black line is followed to the right where it meets the red curve, indicating the resonance radius of the echo sounder. From there the blue curve is taken to the surface showing the initial bubble radius of the bubble.

This value depends of course on the assumed vertical current speed. In the present example ($w = -0.5\,\mathrm{m\,s^{-1}}$), the gas bubbles measured at 160 m depth had a radius of 2 mm at the sea surface. This assumed current speed is certainly at the upper limit of the actual currents, so

that the calculated initial bubble radius can be considered as a minimal value. For a current speed of $w = -0.4\,\mathrm{m\,s^{-1}}$ the initial radius increases to 2.5 mm, and for $w = -0.3\,\mathrm{m\,s^{-1}}$ it is 5 mm.

The bubble model can be also used to determine the minimal vertical current speed which is necessary to pull down a bubble from the sea surface, so that it finally ends up with a certain size at a given depth. In particular, we are interested in finding this minimal current speed for the echo sounder measurements, i.e. the radii and depths given by the curve showing the resonance radius (Figure 5.2).

For our considerations we assume a constant vertical current speed w, so that bubbles with initial radii above a certain cut-off radius r_c corresponding to a rise speed greater than the vertical currents $|w_{b0}| > |w|$ rise back to the surface. Bubbles with radii $r_0 \leq r_c$ and $|w_{b0}| \leq |w|$ are pulled down. Of the bubbles which are pulled down, the ones with the biggest initial radius $r_0 = r_c$ go deepest (the bubble path furthest to the right in Figure 5.2). At depth z_{res} where the bubble has a radius equal to the resonance radius r_{res} (the location where the bubble path intersects the curve of the resonance radius), the echo sounder can detect the bubble. This means that the strength of the minimal currents, which are required to explain the presence of a bubble of radius r_{res} at depth z_{res}, is equal to the initial rise speed of that bubble w_{b0}, which it had at the injection depth.

In Figure 5.3a, several of these bubble paths are plotted. They are calculated for the corresponding minimal current speed $|w| = |w_{b0}|$ of that particular bubble and an injection depth of 0.1 m. In Figure 5.3b, the resulting relationship between bubble depth measured with a 100 kHz echo sounder and the minimal vertical current speed is shown. Hence, a vertical current speed of $|w| \geq 0.27\,\mathrm{m\,s^{-1}}$ is necessary to pull down gas bubbles as deep as 160 m depth (Figure 5.2). This is consistent with current measurements showing values between $-0.3\,\mathrm{m\,s^{-1}}$ and $-0.7\,\mathrm{m\,s^{-1}}$ in the bubble cloud.

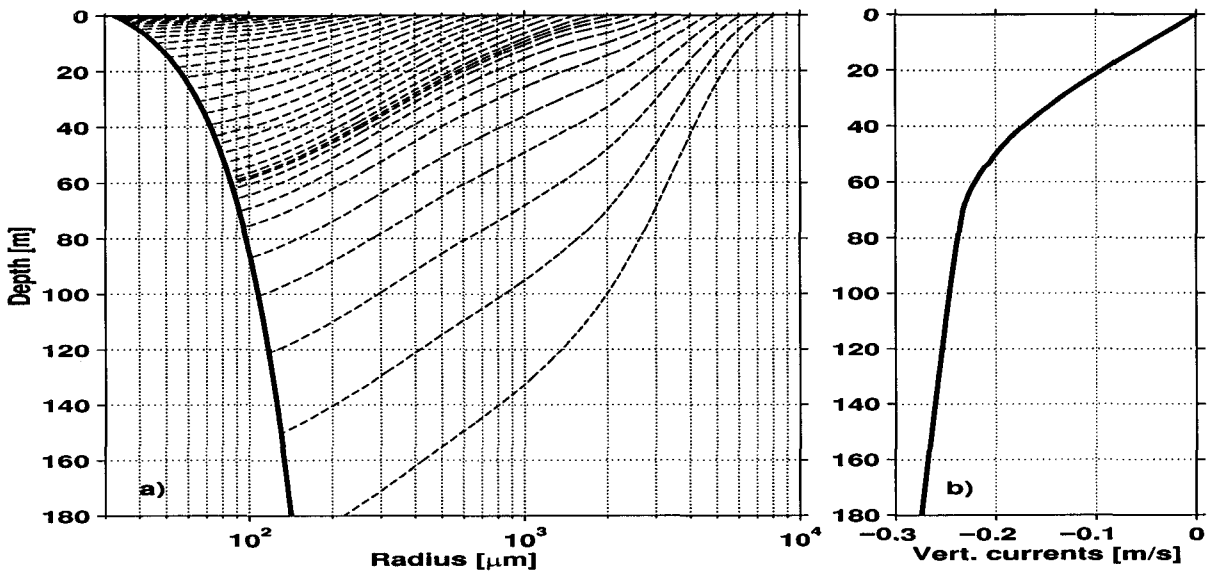

Figure 5.3: *a) Resonance radius of a 100 kHz echo sounder (solid line) and "bubble paths" (dashed lines) for gas bubbles of different initial radius r_c and corresponding minimal vertical current speed $|w| = |w_{b0}|$. b) Resulting relationship between minimal current speed and depth of the observed bubbles.*

Acoustical resonator measurements

Measurements with an acoustical resonator provide bubble size distributions for bubble radii between 15 and 550μm at some depth well below the sea surface (Section 2.1). However, for an estimate of the gas flux from the atmosphere into the ocean, it is essential to know the bubble size distribution at the sea surface.

Also here, the bubble model can be used. As an example a bubble size distribution measured in the tidal front at Boundary Pass at a depth of 20 m (Figure 2.8) is taken. As before, the bubble model is used to calculate the initial radii of the bubbles at the sea surface, assuming different constant vertical current speeds of $-0.1\,\mathrm{m\,s^{-1}}$, $-0.3\,\mathrm{m\,s^{-1}}$, and $-0.5\,\mathrm{m\,s^{-1}}$, with no turbulence. The resulting initial bubble size distributions are plotted together with the one at 20 m depth in Figure 5.4.

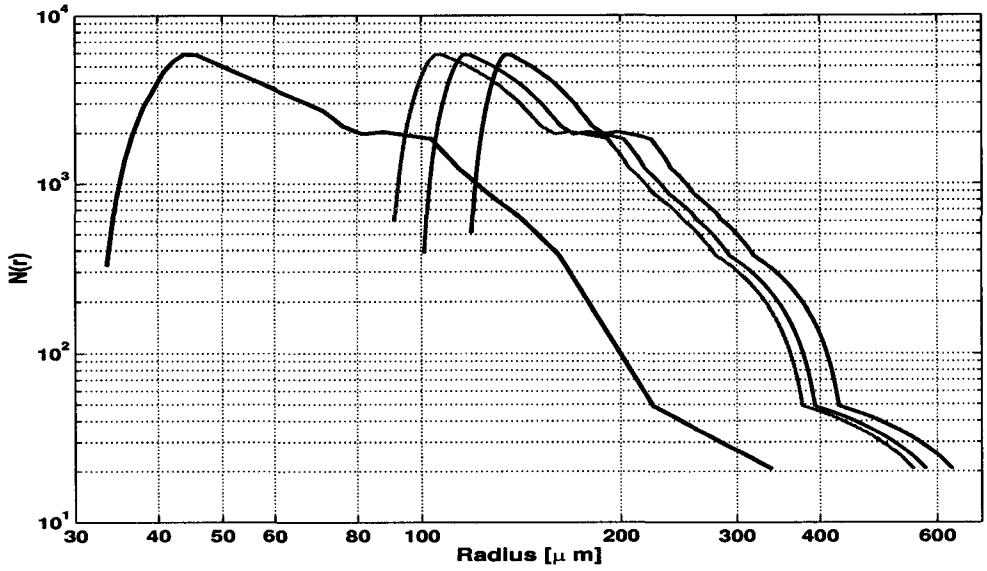

Figure 5.4: *Bubble size distribution measured in the tidal front at Boundary Pass on September 29, 2000, at 20 m depth (black). The bubble model was used to back-trace the size distribution to the surface assuming different vertical current speeds of* $-0.1\,\mathrm{m\,s^{-1}}$ *(blue),* $-0.3\,\mathrm{m\,s^{-1}}$ *(green), and* $-0.5\,\mathrm{m\,s^{-1}}$ *(orange).*

The integral over all bubbles yields the initial void fraction. Because not all bubble sizes were measured, the calculated values, which are listed in Table 5.2, can be considered as lower estimates. The results depend on the assumed current speed: a decrease in current speed from $-0.5\,\mathrm{m\,s^{-1}}$ to $-0.1\,\mathrm{m\,s^{-1}}$ results in an increase of the void fraction by about 65%. Implementing turbulence into the model only has a minor effect on the estimated void fraction and will therefore be neglected in the following.

For an estimate of the air-sea gas exchange in a tidal front due to gas bubbles, the void fraction at the sea surface is multiplied with the vertical current speed and integrated over the surface area of the front. This is discussed in detail in Section 7.1.

w [ms^{-1}]	Turbulence	Void fraction
-0.1	no	$2.11 \cdot 10^{-5}$
-0.1	yes	$2.04 \cdot 10^{-5}$
-0.3	no	$1.49 \cdot 10^{-5}$
-0.3	yes	$1.51 \cdot 10^{-5}$
-0.5	no	$1.23 \cdot 10^{-5}$
-0.5	yes	$1.22 \cdot 10^{-5}$

Table 5.2: *Void fraction at the sea surface calculated with the bubble model for different vertical current speeds w. As a comparison, the void fraction at the measurement depth of 20 m depth was only* $1.3 \cdot 10^{-7}$.

6 Air-sea gas exchange in a convergence zone

The influence of vertical currents on the penetration depth of bubble plumes was observed by Thorpe & Stubbs (1979) and Thorpe (1982). The authors found bubbles reaching depths much greater than twice the wave height suggesting that they must be carried down by other mechanisms than waves, like the currents associated with Langmuir circulations.

Strong vertical currents in a tidal front can also pull down gas bubbles to significant depths of up to 160 m as observed at Boundary Pass (Figure 5.2). This requires current speeds exceeding the rise speed of the bubbles throughout the water column.

It will be shown in this section that downwelling currents increase the amount of gas which dissolves from bubbles before they rise back to the sea surface. A bulk description of bubble behaviour is introduced and is used to calculate the total amount of dissolved gas. It is combined with a model of wave-current interaction (Section 4) and applied to the conditions at the flood tidal front at Boundary Pass in order to estimate the air-sea gas exchange in the tidal front.

6.1 Gas entrainment in a spatially varying flow field

The effect of downwelling currents on bubble induced gas entrainment will be discussed on the basis of two simple scenarios: bubble entrainment with no vertical currents and with constant vertical currents. The case of temporally changing currents is equivalent to a steady but horizontally changing flow field - a situation like the one at Boundary Pass. It will be described in Section 6.2.

6.1.1 Case with no currents

Let us first consider the case of gas entrainment with no vertical currents, i.e. all injected gas bubbles rise back to the surface due to their buoyancy and are not pulled further down by the currents. On their way up, the bubbles lose gas to the surrounding water by dissolution.

The percentage of gas $d(r,z)$, which dissolves from a bubble while it rises to the surface, is computed by using the formulas introduced in Section 5. It is shown in Figure 6.1 for the four gases O_2, N_2, CO_2, and Ar as a function of initial bubble radius r and injection depth z. The smaller bubbles dissolve completely before they reach the sea surface (marked by the gray shaded area), while the bigger ones rise all the way back to the surface where the remaining gas is released to the atmosphere.

The ratio of the total amount of a dissolved gas per 1 μm-increment to injected gas is then given by

$$G_j(r) = \frac{\int_{-\infty}^{0} d_j(r,z)\, N(r,z)\, V_0(r,z)\, dz}{\int_{r_1}^{r_2} \int_{-\infty}^{0} N(r,z)\, V_0(r,z)\, dz\, dr} \quad . \tag{6.1}$$

The index j stands for one of the gases O_2, N_2, CO_2, or Ar, with $j=1,2,3,4$.

$$N(r,z) = \beta e^{z/\gamma} r^{\alpha} \tag{6.2}$$

is the initial bubble size distribution with the entrainment depth γ, the spectral slope α, and a scaling factor β (Section 4.5).

$$V_0 = \frac{4}{3}\pi r^3 \left(\frac{-g\rho z}{p_{atm}} + 1 \right) \tag{6.3}$$

is the initial volume of a bubble, which it would have at the sea surface under only atmospheric pressure p_{atm}. g is the gravitational acceleration and ρ the density of water.

G_j is plotted in Figure 6.2 for various choices of the entrainment depth γ and a spectral slope $\alpha = -3/2$ for radii $r \leq 1000\,\mu$m, and $\alpha = -10/3$ for $r > 1000\,\mu$m. The figure shows that the air-sea gas exchange for the gases O_2, N_2, and Ar, is dominated by the smaller

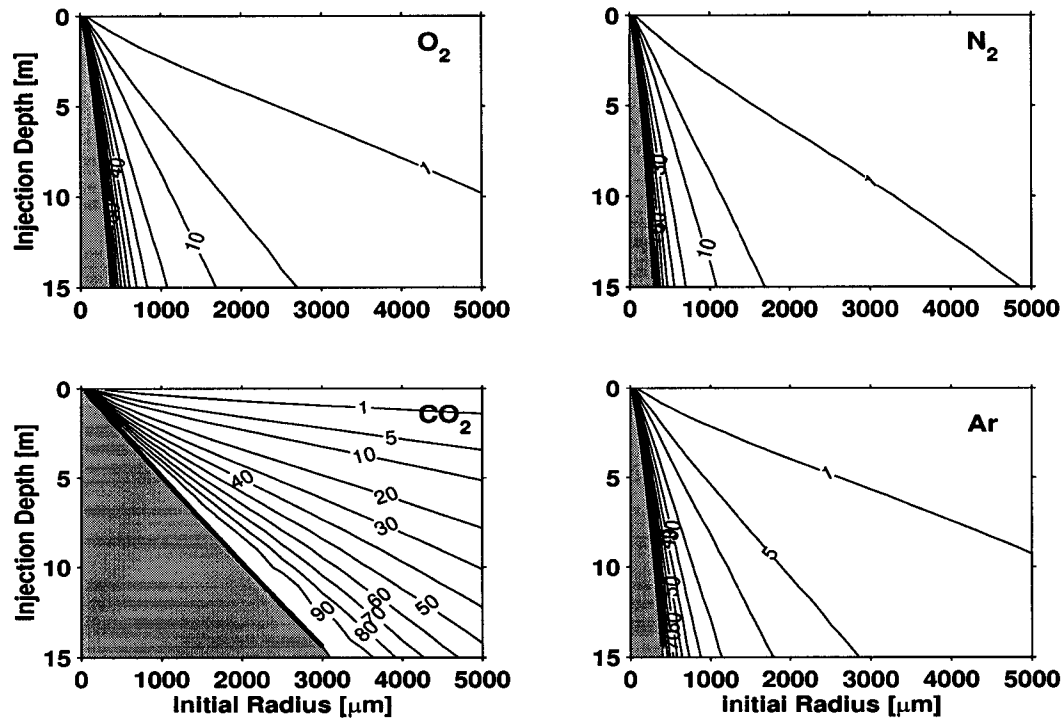

Figure 6.1: *Percentage of gas $d(r, z)$ dissolving from a bubble while it rises back to the surface. It is shown for the gases O_2, N_2, CO_2, and Ar as function of initial bubble radius and depth (d is shown for the upper 15 m, although most bubbles are entrained in the upper 2 m). The gray shaded area marks the bubbles which dissolve completely.*

bubbles with radii $< 400\,\mu$m, while for the highly soluble CO_2, bubbles with radii up to $1500\,\mu$m are the predominant ones (note that the sharp bend of the G_j-curves at $1000\,\mu$m is caused by the change in spectral slope describing the initial bubble size distribution and is therefore somewhat artificial). It is also evident bigger bubbles are increasingly important for bigger entrainment depths. This is especially true for CO_2.

The total percentage of gas lost by dissolution is given by the integral over all gas bubbles $\mathcal{G}_j = \int_r G_j(r)\,dr$ and is listed in Table 6.1. It is calculated for bubble radii between $1\,\mu$m and $5000\,\mu$m and depends strongly on the assumed entrainment depth γ, because bubbles which are injected deeper have a longer way through the water column back to the surface

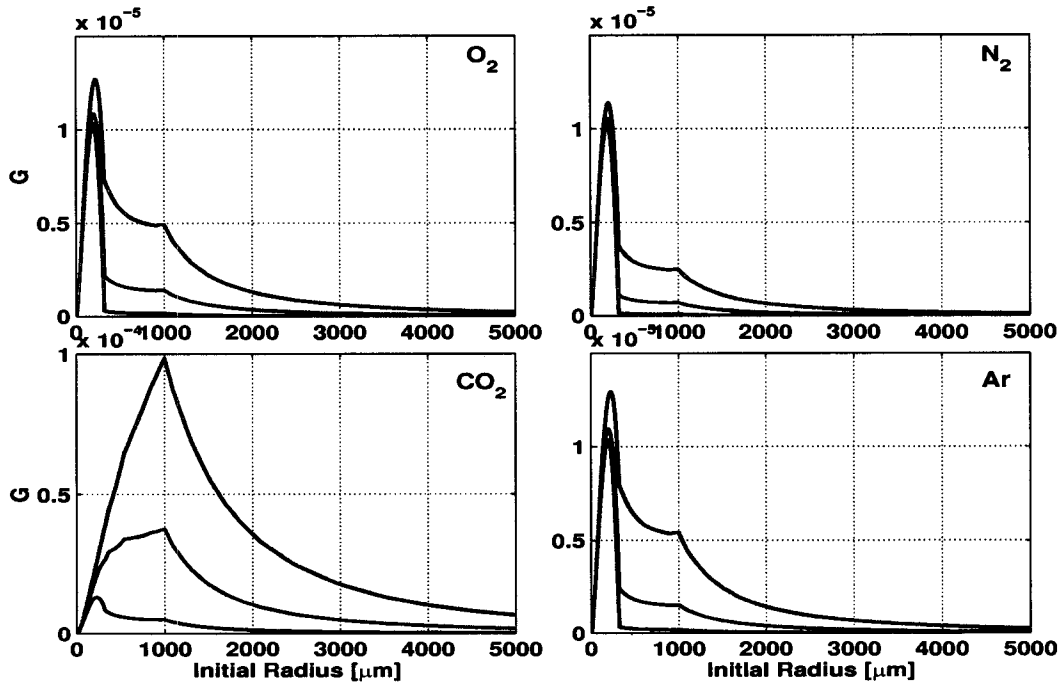

Figure 6.2: *Ratio G_j of the amount of dissolved gas to the total injected gas per 1 μm-increment for O_2, N_2, CO_2, and Ar. The curves are plotted for different entrainment depths: γ=0.1 m (red), γ=1 m (green), and γ=2 m (blue).*

and hence more time to lose gas by dissolution. Also here, the percentage of dissolved gas is higher for CO_2 than for the other gases.

γ [m]	$\mathcal{G}(O_2)$ [%]	$\mathcal{G}(N_2)$ [%]	$\mathcal{G}(CO_2)$ [%]	$\mathcal{G}$(Ar) [%]
0.1	0.2	0.2	0.3	0.2
1	0.4	0.3	5.4	0.4
2	0.6	0.4	10.7	0.7
5	0.9	0.5	15.6	0.9

Table 6.1: *Total percentage of gas dissolved, $\mathcal{G}_j$, for O_2, N_2, CO_2, and Ar as a function of entrainment depth γ.*

The values for G_j and $\mathcal{G}_j$ depend on the saturation of the gases in water, as it determines the rate at which the gases dissolve (Section 5). For our calculations, a saturation of 100% throughout the water column has been used for all four gases. The error of this assumption will be discussed at the end of Section 6.2.

6.1.2 Downwelling currents

Let us now consider the purely 1-dimensional case with a uniform downwelling current w, but no horizontal currents. In the following, we will compute the percentage of dissolved gas per $1\,\mu$m-increment G_j and the total percentage of dissolved gas $\mathcal{G}_j$, as discussed above. The corresponding formulas for calculating the bubble behaviour due to dissolution and compression are described in Section 5.

The injected gas bubbles are kept under water for longer by the currents, increasing the time during which gas dissolves. A bubble dissolves completely, if the vertical currents are stronger than its (initial) rise speed. This is obvious in Figure 6.3 where the dissolution coefficient $d(r,z)$ is plotted for a current speed of $w=-0.2\,\mathrm{m\,s^{-1}}$. It shows that all bubbles which are smaller than a certain cut-off radius dissolve completely as marked by the gray shaded area. Also the bigger bubbles lose more gas than in the case without currents, but they still reach the sea surface.

Consequently, the amount of dissolved gas increases with the strength of the downwelling currents. The portion of dissolved gas per $1\,\mu$m-increment G_j is plotted in Figure 6.4 for a current speed of $w=-0.2\,\mathrm{m\,s^{-1}}$. The values of G_j are significantly higher than the previous ones for the case with no currents (Figure 6.2) and the peak is shifted to higher radii. It reaches its maximal value at $900\,\mu$m. For radii $< 900\,\mu$m, the bubble rise speed is less than the current speed (Figure 5.1), so that the bubbles dissolve completely.

The relationship between the percentage of total dissolved gas $\mathcal{G}_j$ and current speed is plotted in Figure 6.5 . $\mathcal{G}_j$ increases slowly for currents up to $-0.2\,\mathrm{m\,s^{-1}}$. Between $-0.2\,\mathrm{m\,s^{-1}}$ and $-0.3\,\mathrm{m\,s^{-1}}$, $\mathcal{G}_j$ increases much more rapidly. This sudden increase can be explained

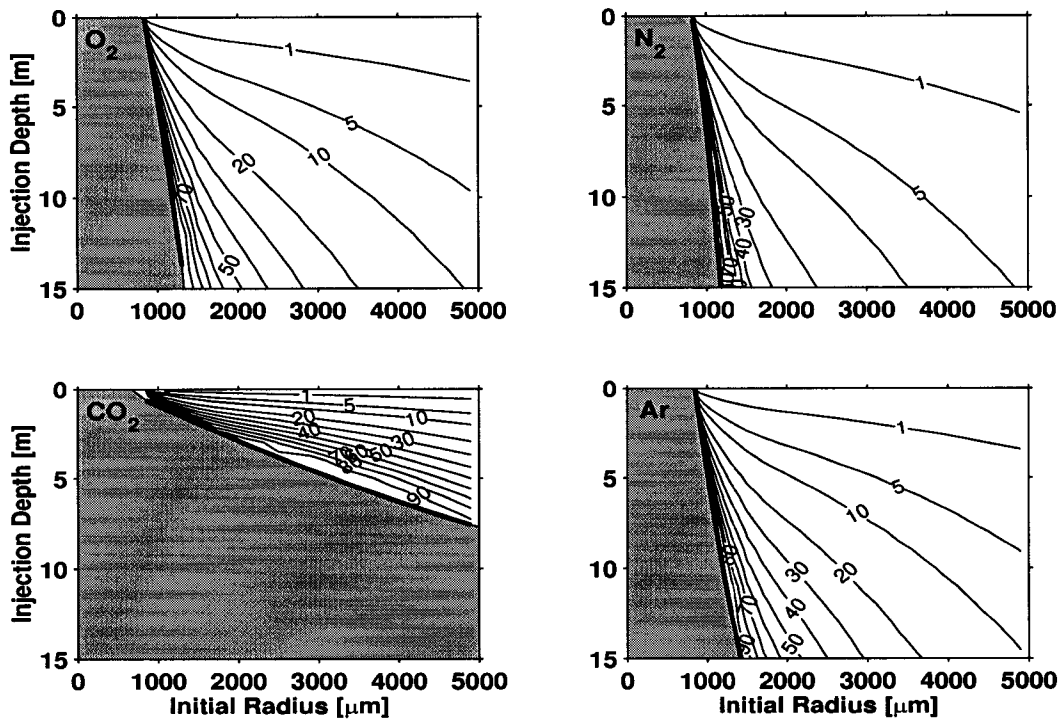

Figure 6.3: *Percentage $d(r,z)$ of gas dissolving from a bubble while it rises back to the surface. It is shown for the gases O_2, N_2, CO_2, and Ar as a function of initial bubble radius and depth and for a current speed of $w=-0.2\,\mathrm{m\,s^{-1}}$. The gray shaded area marks the bubbles which dissolve completely.*

by the function describing the rise speed of gas bubbles (Figure 5.1). For bubble radii between $700\,\mu$m and $7000\,\mu$m, the bubble rise speed increases only gradually from $0.2\,\mathrm{m\,s^{-1}}$ to $0.3\,\mathrm{m\,s^{-1}}$. Therefore, only a slight increase in current speed greatly increases the number of bubbles which are pulled down by the currents and dissolve completely.

The differences in the curves for the four gases result from the different coefficients of diffusion. CO_2 dissolves more quickly than the other gases, and for currents stronger than $-0.25\,\mathrm{m\,s^{-1}}$ all CO_2 is lost. N_2 has a low diffusion rate, so that "old" bubbles basically contain only N_2, but no other gases.

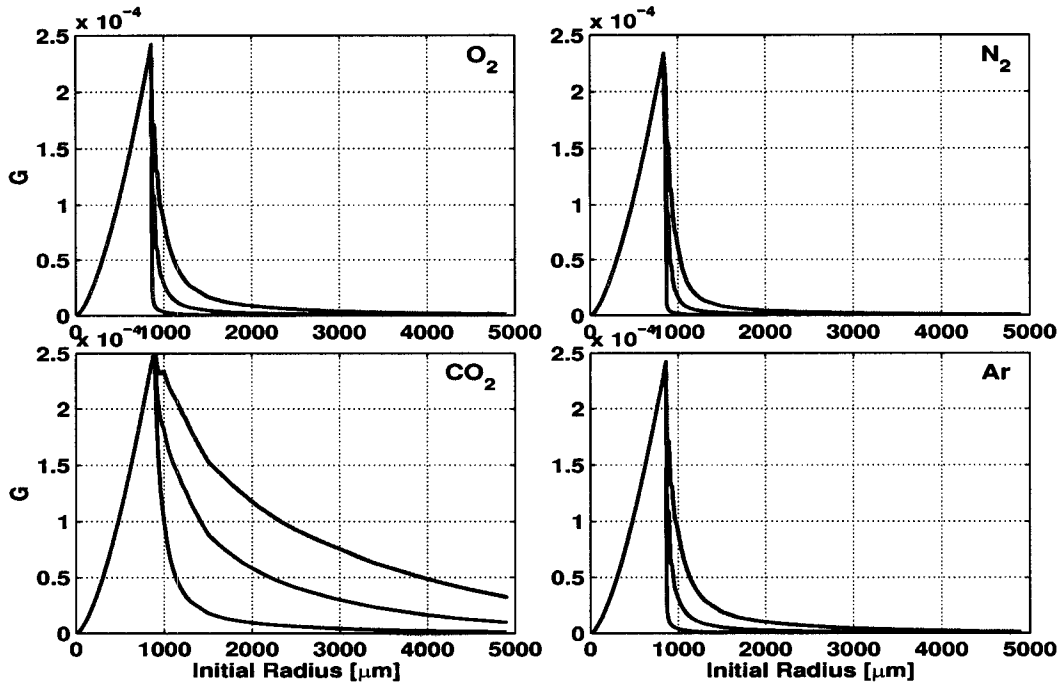

Figure 6.4: *Ratio of the total amount of dissolved gas G_j to the total injected gas per 1 μm-increment for O_2, N_2, CO_2, and Ar for a current speed of $w = -0.2\,\mathrm{m\,s^{-1}}$. The curves are plotted for different entrainment depths: $\gamma = 0.1\,m$ (red), $\gamma = 1\,m$ (green), and $\gamma = 2\,m$ (blue).*

6.2 Application to the sill flow at Boundary Pass

We will now look at the processes which are responsible for the enhancement of air-sea gas exchange in the flood tidal front at Boundary Pass. In general, the gas exchange in a convergence zone is determined by the combination of two mechanisms: gas bubble injection by breaking waves due to wave-current interaction and the subduction of bubbles by downwelling currents.

In this section, the size distribution and location of injected bubbles will be calculated with the model of wave-current interaction (Section 4). We will then apply the bubble model (Section 5) as above in order to determine how much of the injected gas is dissolved in the

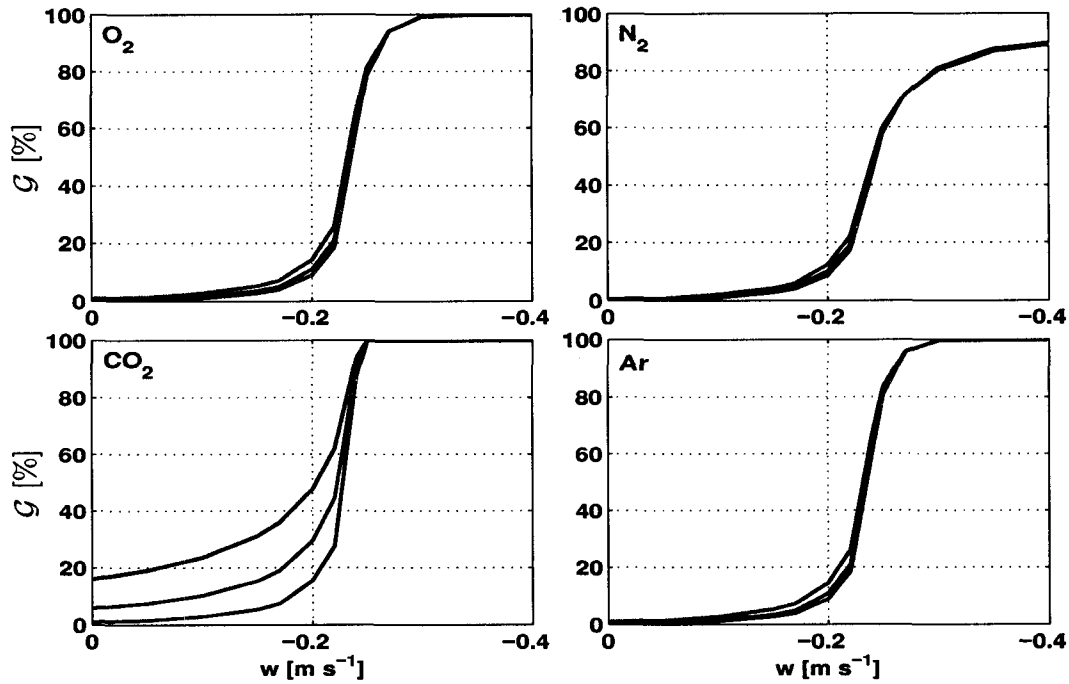

Figure 6.5: *Percentage of the total amount of dissolved gas $\mathcal{G}$ for* O_2, N_2, CO_2, *and* Ar *as function of current speed w. It is plotted for different entrainment depths: $\gamma = 0.1\,m$ (red), $\gamma = 1\,m$ (green), and $\gamma = 2\,m$ (blue).*

ocean. Finally, the sensitivity of the results is investigated in order to estimate the error of the model calculations due to the uncertainties of the used parameter values.

Energy dissipated by wave breaking

Waves, which travel into the flood tidal front at Boundary Pass, are either generated in the Strait of Georgia (approaching from the East) or in the Haro Strait/Boundary Pass region to the West of the sill. In the first case, the horizontal currents (Figure 6.6a) change from still water to fast opposing current, while in the second case the transition is the other way around.

The horizontal currents u are used to determine the amplitude and steepness of the approaching waves with the model of wave-current interaction described in Section 4. In the

following, three different waves are chosen as examples. They may represent wind/wave conditions on a calm, average, and windy day (the initial steepness for all waves is below the critical value for breaking though). In particular, the following values for the initial amplitude a_0 and wave length λ_0 are chosen: $a_0 = 0.05\,\mathrm{m}$, $\lambda_0 = 1.5\,\mathrm{m}$ (wave I, calm day; see Figure 4.10b), $a_0 = 0.2\,\mathrm{m}$, $\lambda_0 = 8\,\mathrm{m}$ (wave II, average day), and $a_0 = 1\,\mathrm{m}$, $\lambda_0 = 15\,\mathrm{m}$ (wave III, windy day). The change in amplitude and the energy dissipated by wave breaking are calculated for waves approaching from the East and from the West. The results are plotted in Figures 6.6 and 6.7, respectively.

The initial wave length λ_0 determines the phase speed $c_0 = \sqrt{\lambda_0 g/2\pi}$ of the wave (g is the gravitational acceleration) and hence how far the wave can approach against the current before it reaches the critical value of $u/c_0 = -1/4$ where it is stopped (see also Section 4). This is obvious in Figures 6.6b and 6.7a, showing that wave III advances farther against the currents than the shorter waves.

The initial steepness of the wave $a_0 k_0$ determines how soon the wave starts to break and is therefore also an important parameter for determining where gas bubbles are generated. Waves with a high initial steepness break earlier than the waves which are not so steep (Figure 4.3). Hence, the initial steepness determines the beginning, and the wave length the end of the break region.

Bubble injection and dissolution

The breaking waves inject gas bubbles into the ocean. Their initial size distribution is calculated as function of horizontal distance and depth, as described in the Section 4.5. The resulting vertically averaged void fraction is shown in Figures 6.7d and 6.7c. The parameter values used in the calculations are listed in Table 6.2.

In order to calculate how much of the injected gas is dissolved, a similar approach to the one in Section 6.1.2 is chosen. The amount of dissolved gas depends on the strength of the vertical flow component w. As w changes horizontally, also the injection location of the bubbles has to be taken into account. The horizontal currents carry the bubbles from

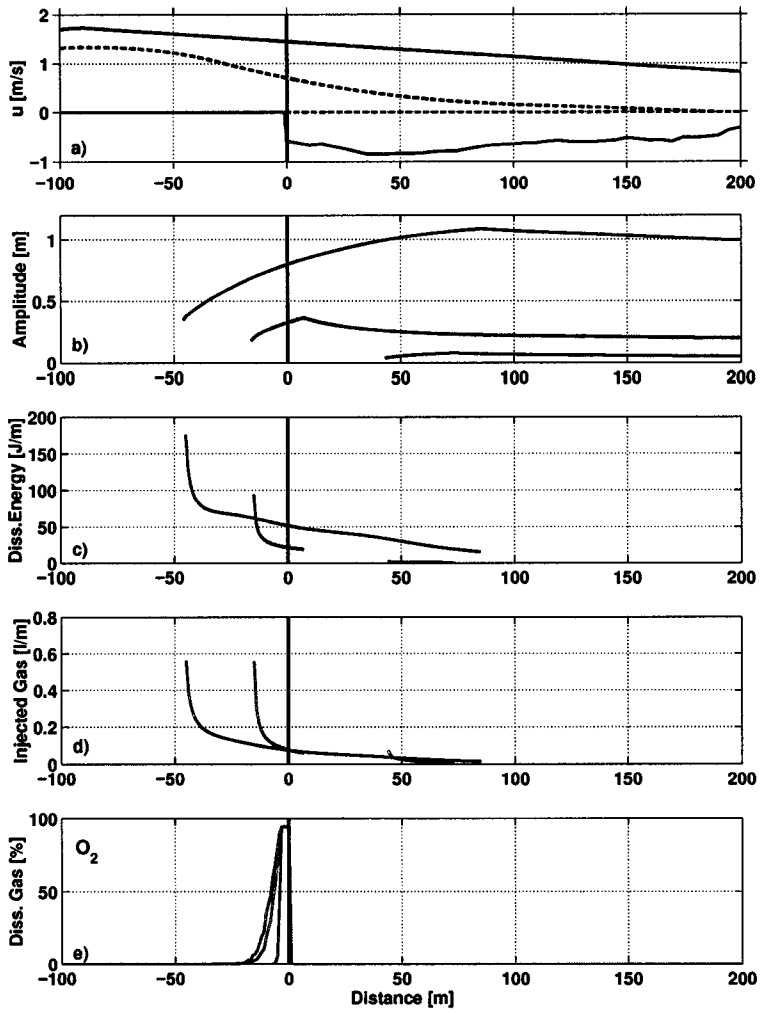

Figure 6.6: *a) Horizontal (blue) and vertical (red) flow component in the tidal front at Boundary Pass. Surface currents are shown by dashed lines, vertically averaged lower layer currents by solid lines. b)-c) Amplitude and dissipated energy for waves I (red), II (blue), and III (green) approaching the front from the East (Strait of Georgia); d) amount of gas injected by the three waves; e) percentage of oxygen dissolved for detrainment depths 0.05 m (green), 0.5 m (magenta), and 1 m (cyan).*

there into regions of different w, so that for each injection location, the vertical currents are described as a function of time (in a reference frame moving horizontally with the

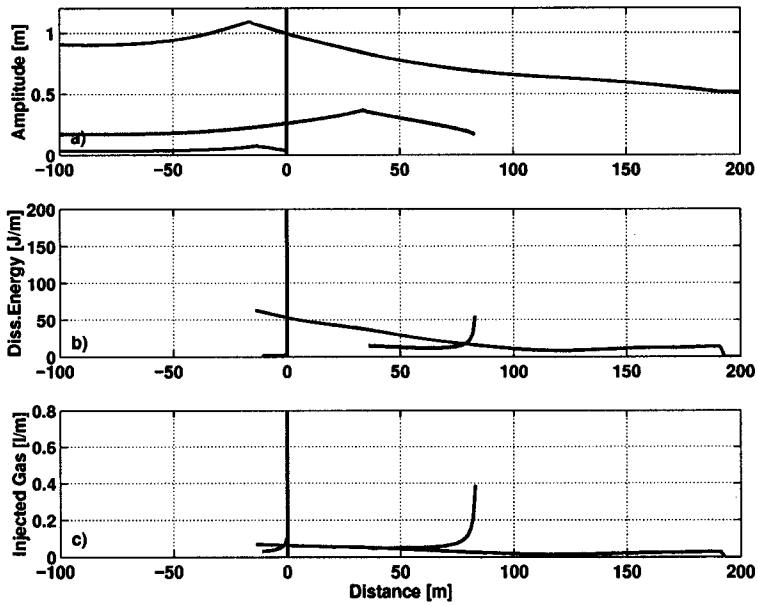

Figure 6.7: *a)-b) Amplitude and dissipated energy for waves I (red), II (blue), and III (green) approaching the front from the West; c) amount of gas injected by the three waves.*

currents/bubbles). It is assumed that the vertical currents are zero to the east of the frontal location, and that the bubbles which are injected at a location to the west of the front are carried downward by the vertically averaged lower layer currents as soon as they are advected horizontally past the lower layer plunge point (Figure 6.6a; for a detailed description of the flow field see Section 3 or Figure 1.7).

For each injection location, it can now be calculated how much gas of a bubble of a certain radius and injection depth is dissolved, yielding diagrams similar to the ones in Figure 6.3. The total portion of gas dissolved $\mathcal{G}$ (derived by a depth integral over all bubbles) depends then on the initial bubble entrainment depth γ. $\mathcal{G}$ is plotted in Figure 6.6d for O_2 and for the entrainment depths 0.05 m, 0.5 m, and 1 m, assuming a horizontally constant initial bubble size distribution.

Bubbles injected within 3-5 m to the west of the tidal front dissolve almost completely due to the very strong vertical currents exceeding the rise speed of even the bigger bubbles. In

this zone, the total amount of gas dissolved does therefore not depend on γ. Farther to the west, $\mathcal{G}$ decreases, as some of the bubbles have time to rise back to the sea surface before they are advected into the region of strong downwelling currents. Between $x = -3\,\mathrm{m}$ and $x = -17\,\mathrm{m}$, $\mathcal{G}$ drops to values of $< 3\%$ for all relevant entrainment depths. To the east of the front, $\mathcal{G}$ is not influenced by the currents, because the bubbles remain in the stagnant water mass. Also here, the results depend on the bubble entrainment depth γ.

With this in mind, we can now go back to the plots showing the initially injected amount of gas as function of horizontal distance (Figures 6.6d and 6.7c). For our considerations, i.e. the contribution of the front to the aeration of the subsurface water in the Strait of Georgia, we are only interested in the dissolved gas which is finally carried to these depths. The gas injected to the east of the front stays in the surface layer and will therefore be neglected, although the air-sea gas exchange in that region is increased by enhanced wave breaking. Wave breaking due to wave-current interaction also takes place within 50 m to the west of the front. But as shown above, only within 317 m of the front a significant portion of the entrained gas is dissolved, so that only the bubbles injected in that area contribute to the aeration of intermediate water.

The waves which contribute most to the aeration of the intermediate water have short initial wave lengths, if they approach from the West, so that they break before they reach the tidal front (wave I). Waves approaching from the East can only contribute, if they are fast enough to travel past the front. This is the case for waves with an initial wave length of more than 5 m (waves II, III). Their contribution to the aeration is highest if their energy is dissipated (and bubbles are injected) within the zone of high dissolution close to the front, i.e. if they are not too fast to travel past that zone (this depends of course on the horizontal flow field in the convergence zone).

Oxygen flux

We will now calculate the oxygen flux in the entire tidal front at Boundary Pass. For this, the total amount of gas injected by one wave is multiplied by the mole fraction of oxygen

$\chi = 0.21$ and the width of the front (2200 m). It is then divided by the wave period and averaged over 1 d, assuming that the investigated processes take place twice a day for a 2 h-period during flood tide.

The results are listed in Table 6.2 for waves I, II, and III approaching the tidal front from both directions. The amount of dissolved gas injected by the waves to the east of the front is omitted.

Sensitivity of model results

The given values for the oxygen flux should not be taken as absolute numbers as they are based on a greatly simplified scenario. The presented model, however, can give some useful insight into the physical processes, which are responsible for air-sea gas exchange in a convergence zone. A sensitivity study of the model results can help in particular to understand the importance of single parameters (e.g. wave length, entrainment depth) for the gas exchange.

As reference runs, we will take wave II approaching from the east and wave I approaching from the west. New model runs are carried out with one parameter changed at a time, so that the sensitivity to that particular parameter can be studied. The results are listed in Table 6.2.

The diffusion of gas between bubble and water depends on the gas pressure inside and outside of the bubble (Section 5). However, the saturation levels of gas have little effect on the gas flux in this particular front. Due to the small entrainment depths, the bubbles either rise quickly back to the surface, so that an increased diffusion speed hardly has any effect, or they dissolve completely anyway. For example, if the saturation σ of O_2 in the water drops from 100% to 80%, the total gas flux in the front increases by less than 3%.

The spectral slope of the bubble size distribution α determines the relative importance of small versus big bubbles. In the reference runs, α has been -3/2 for $r \leq 1000\,\mu$m and -10/3 for $r < 1000\,\mu$m. If instead we chose $\alpha = -2$ for the whole spectrum, so that there are more

big bubbles in the water, the gas flux decreases by about 9% as the bubbles rise quicker to the surface. If there are on the other hand more small bubbles ($\alpha = -4.5$), the gas flux increases significantly by a factor of 2-7.

As shown above, the amount of dissolved gas depends on the location where it is injected. The break location again is determined by the wave length and initial steepness of the wave. Due to the many different possible wind/wave conditions, the model results should not be seen as an attempt to get a reliable estimate of the gas flux in the front, but can help to understand the bubble injection by breaking waves.

Intuitively, one might think that bigger waves inject more bubbles. However, the dissipated wave energy is, to first order, proportional to a^2 (if the effect of the currents is ignored); and the energy, which goes into the subduction of gas bubbles, is proportional to γ^2 (Equation 4.32), and hence also to a^2 (within the upper meter of the water column, where bubble compression can be neglected). This means that a bigger wave does not inject more bubbles, but injects them deeper. If we increase the detrainment depth without increasing the amplitude, less bubbles are injected and the gas flux decreases. An increase of γ by a factor of 4 reduces the gas flux by 75%.

On the other hand, the portion of energy $\mathcal{E}$, which goes into the subduction of gas bubbles, might increase with wave height. The relationship to the total amount of injected gas is linear (Equation 4.33), so that an increase in $\mathcal{E}$ would lead to an increase in gas flux.

This also shows that the big range of $\mathcal{E}$ determined from only a few measurements (Table 4.2) leads to big uncertainties in the calculated oxygen flux. For our model runs, we have so far assumed a very low value of $\mathcal{E} = 0.003$, which may be suitable for waves with amplitudes of a few centimeters. For bigger waves – or if the breaking waves are plunging, not spilling breakers – a higher value for $\mathcal{E}$ may be more appropriate. If we take a value at the other end of the range ($\mathcal{E}$=0.3), the resulting oxygen flux increases by a factor of 100 (Table 6.2). The implications of this (and the other uncertainties) will be discussed in the next section, where the oxygen input rates will be compared to other oxygen sources in the Fraser Estuary.

← Waves from the Strait of Georgia

Wave	a_0 [m]	λ_0 [m]	$a_0 k_0$	Break Region	α	γ [m]	σ [%]	$\mathcal{E}$ [%]	O_2-flux [m^3/s]
I	0.05	1.5	0.32	74m to 42m	-1.5/-3.3	$a/4$	100	0.3	0
II	0.2	8	0.13	7m to -17m	-1.5/-3.3	$a/4$	100	0.3	0.012
III	1	15	0.42	85m to -47m	-1.5/-3.3	$a/4$	100	0.3	0.009
II	0.2	8	0.13	7m to -17m	**-2**	$a/4$	100	0.3	0.011
II	0.2	8	0.13	7m to -17m	**-4.5**	$a/4$	100	0.3	0.086
II	0.2	8	0.13	7m to -17m	-1.5/-3.3	**a**	100	0.3	0.003
II	0.2	8	0.13	7m to -17m	-1.5/-3.3	$a/4$	**80**	0.3	0.012
II	0.2	8	0.13	7m to -17m	-1.5/-3.3	$a/4$	100	**30**	1.17

→ Waves from Boundary Pass

Wave	a_0 [m]	λ_0 [m]	$a_0 k_0$	Break Region	α	γ [m]	σ [%]	$\mathcal{E}$ [%]	O_2-flux [m^3/s]
I	0.05	1.5	0.32	-13m to 1m	-1.5/-3.3	$a/4$	100	0.3	0.02
II	0.2	8	0.13	33m to 84m	-1.5/-3.3	$a/4$	100	0.3	0
III	1	15	0.42	> -16m	-1.5/-3.3	$a/4$	100	0.3	0.007
I	0.05	1.5	0.32	-13m to 1m	**-2**	$a/4$	100	0.3	0.018
I	0.05	1.5	0.32	-13m to 1m	**-4.5**	$a/4$	100	0.3	0.045
I	0.05	1.5	0.32	-13m to 1m	-1.5/-3.3	**a**	100	0.3	0.005
I	0.05	1.5	0.32	-13m to 1m	-1.5/-3.3	$a/4$	**80**	0.3	0.021
I	0.05	1.5	0.32	-13m to 1m	-1.5/-3.3	$a/4$	100	**30**	2.03

Table 6.2: *Parameter values for the model calculations of gas entrainment in the tidal front at Boundary Pass. For the given O_2-flux values, only the contribution to the aeration of subsurface water in the Strait of Georgia is considered (see text). The lower part of the tables shows the results from the sensitivity study; values different to the ones of the reference runs (upper part of table) are shown in bold letters.*

7 Air-sea gas exchange in the Fraser Estuary

Oxygen is supplied to an estuary by diffusion through the sea surface, the entrainment of gas bubbles from wave breaking, photosynthesis, or advection. Tidal fronts can be an additional source of oxygen in estuaries with strong flow-topography interaction.

In the Fraser Estuary, several pronounced tidal fronts develop during ebb and flood tide. Their contribution to the aeration of the estuary is estimated in this section and compared with other oxygen-sources. Special attention is given to the supply of oxygen to the subsurface waters in the Strait of Georgia.

7.1 Contribution of tidal fronts

The tidal front at Boundary Pass is the most pronounced front in Haro Strait. The oxygen flux in this front will be calculated from the model results presented in Section 6.2 as well as from measurements of bubble size distribution and current speed. The results will then be used to also estimate the oxygen flux in other fronts in Haro Strait. A minimal value will be given as well as a "best guess".

Estimate from model results

In Section 6.2, the oxygen flux in the tidal front at Boundary Pass has been calculated by applying the model of wave-current interaction (Section 4) and bubble behaviour (Section 5) to the conditions in the front. The model results depend on the chosen wind/wave conditions, since only the bubbles injected by waves breaking within a few meters of the front contribute to the aeration of intermediate water in the Strait of Georgia.

The oxygen flux derived for waves reaching this zone is on the order of $0.02\,m^3s^{-1}$ (Table 6.2). This estimate is based on conservative values for the entrainment depth γ, the gas saturation σ, and the portion of energy which goes into the subduction of bubbles $\mathcal{E}$. The resulting gas flux can therefore be taken as a minimal value (Table 7.1).

	Model		Observations	
	Best Guess	Minimal Value	Best Guess	Minimal Value
Boundary Pass:				
Early stage	0.1	0.02	0.37	0.002
Late stage	–	–	2.3	0.002
Total	> 0.1	> 0.02	2.8	0.004
All fronts (intermediate water)	0.25	0.05	0.9	0.005

Table 7.1: *Average oxygen flux in tidal fronts associated with gas bubbles estimated from model calculations and observations; values are given in m^3s^{-1}. The lower row shows the estimated contribution of all fronts to the aeration of intermediate water in the Strait of Georgia.*

The model results do not change much, if a different gas saturation level or a different spectral slope are chosen. They are, however, quite sensitive to $\mathcal{E}$ and γ. $\gamma = a/4$ and $\mathcal{E} = 0.003$ were used in the model runs. The values are given for small spilling breakers with amplitudes of only a few centimeters (Section 6.2). For higher waves these values may not be valid anymore and γ may increase by a factor of up to 4, $\mathcal{E}$ by a factor of up to 100 (for small plunging breakers). It is therefore reasonable to assume intermediate values of $\gamma = a/2$ and $\mathcal{E} = 0.03$, which would yield a gas flux of $0.1\,m^3s^{-1}$. This value will be taken as a best guess, although it may be even higher if waves of different wave lengths were considered and not just monochromatic waves.

Estimate from observations

Direct measurements of gas bubbles at Boundary Pass provide an alternative way of estimating the gas flux in the tidal front. They provide a value for the void fraction $\mathcal{V}$, which is then multiplied with the mole fraction of oxygen χ, the bubble entrainment depth γ, the current speed u with which the bubbles are carried away, the width $\mathcal{W}$ and length $\mathcal{L}$ of the front, as well as the duration of gas entrainment $\mathcal{T}$ (in h) during a 12 h tidal period. This yields the gas flux in the entire front averaged over a tidal period

$$\text{Gas flux} = \mathcal{V}\chi(O_2)\,\gamma\,u\,\mathcal{W}\,\mathcal{L}\,\mathcal{T}/12 \quad . \tag{7.1}$$

First, we will estimate the gas flux during the early stage of the flood tide (0.5-2.5 h after slack tide). The later stage of the tide (2.5-4.5 h after slack tide) will be discussed below.

An acoustical resonator for measuring bubble size distributions was towed through the tidal front at Boundary Pass. During the transect shown in Figure 2.8, the instrument passed at a depth of 20 m through the bubble plumes entrained in the front. The measured bubble size distribution and corresponding void fraction are shown in Figure 7.1.

The void fraction in the bubble plume is $\mathcal{V}=1.3\cdot10^{-7}$. It is, however, given for a depth of 20 m. In order to get the void fraction at the sea surface – which is needed for calculating the gas flux with Equation (7.1) – the size of the gas bubbles during their injection is calculated by tracking the bubbles back to the surface, using the bubble model described in Section 5. The resulting spectrum is shown in Figure 7.1b for different assumed current speeds. The results vary within a factor of 2 with a mean value of $1.6\cdot10^{-6}$.

The acoustical resonator can only detect gas bubbles within a range of $15-550\,\mu$m. Bubbles outside this range may be present in the water but were not detected. This is indicated by echo sounder measurements taken at the same time showing that gas bubbles were present at a depth of 100 m (Figure 2.8). These bubbles must have had a radius of at least 0.9 mm at the surface (Figure 5.2), which is larger than the largest bubble detected by the resonator. Smaller gas bubbles may have also been present, but were not measured or they dissolved

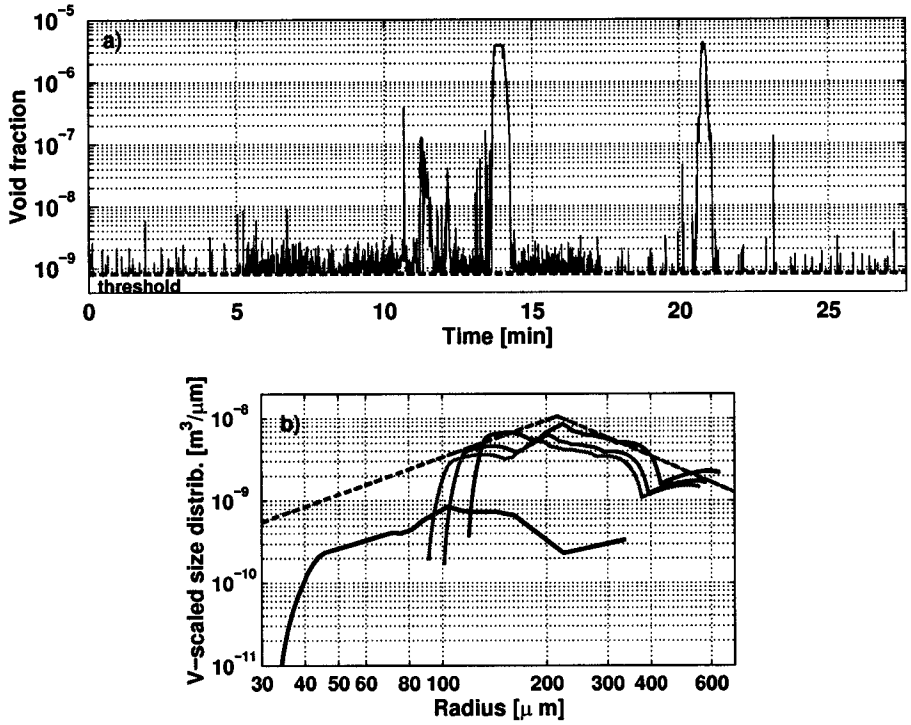

Figure 7.1: *a) The void fraction during the transect shown in Figure 2.8. b) Volume scaled bubble size distribution* $4/3\pi r^3 N(r)$ *(black curve) of the bubble plume in the front in approximately 20 m depth (marked in red in the upper panel and by the black dot in Figure 2.8). The orange, green, and blue curves show the bubble size distribution at the surface, calculated with the bubble model (Section 5) for vertical current speeds of* $0.1\,m\,s^{-1}$, $0.3\,m\,s^{-1}$, *and* $0.5\,m\,s^{-1}$.

completely before they reached the depth of measurement.

To estimate the amount of gas contained in bubbles outside the measurement range, the bubble size distribution is extended to smaller bubbles ($r \leq 220\,\mu m$) with a spectral slope of -1.5, as used in previous model calculations (Section 4.5). For bigger bubbles ($r > 220\,\mu m$), $\alpha = -4.8$ is taken, which matches the slope of the observed surface spectra (Figure 7.1b). The resulting void fraction is $2.9 \cdot 10^{-6}$.

However, even this value is three orders of magnitude smaller than the observations under

small spilling breakers by Loewen *et al.* (1996), and 5 orders of magnitude smaller than the observations under bigger waves (Table 4.1). This seems to be a bit surprising as small spilling breakers are the waves injecting the smallest number of bubbles. It is, however, quite possible that the main bubble plume has been missed by the instrument or that the bubbles have been dispersed over a bigger volume. The measurements may therefore not be representative. Due to the lack of accurate data, we will therefore take the value derived from the observations as a minimal value and the measured void fraction for small spilling breakers of 0.002 as a best guess, assuming that they are injected in the upper 0.15 m of the water column (0.05 m as minimal value).

The gas bubbles are carried downwards with the subducting lower layer. The speed with which the bubbles are advected past the lower layer plunge point and away from the surface is $1.5\,\mathrm{m\,s^{-1}}$ in the horizontal and somewhere between $-0.2\,\mathrm{m\,s^{-1}}$ and $-0.7\,\mathrm{m\,s^{-1}}$ in the vertical. We take a minimal vertical current speed of $-0.2,\mathrm{m\,s^{-1}}$ and an average value $-0.5\,\mathrm{m\,s^{-1}}$ as a best guess, so that the resulting current speed is $1.5\,\mathrm{m\,s^{-1}}$ and $1.6\,\mathrm{m\,s^{-1}}$, respectively.

The width of the front $\mathcal{W}$ is given by the zone in which the injected gas bubbles are subducted by the currents before they rise back to the sea surface. This value is, as estimated in Section 6.2, between 5 m and 17 m, with a best guess of 10 m. The length of the front $\mathcal{L}=2200\,\mathrm{m}$ is given by the geometry of the sill.

To summarize, the values used to calculate the minimal gas flux in the front are $\mathcal{V}=3\cdot10^{-5}$, $\chi=0.21$, $\gamma=0.05\,\mathrm{m}$, $u=1.5\,\mathrm{m\,s^{-1}}$, $\mathcal{W}=5\,\mathrm{m}$, $\mathcal{L}=2200\,\mathrm{m}$, and $\mathcal{T}=2\,\mathrm{h}$. The resulting minimal average gas flux is $8.6\cdot10^{-4}\,\mathrm{m^3s^{-1}}$ (Table 7.1). The values for the best guess are $\mathcal{V}=2\cdot10^{-3}$, $\chi=0.21$, $\gamma=0.15\,\mathrm{m}$, $u=1.6\,\mathrm{m\,s^{-1}}$, $\mathcal{W}=10\,\mathrm{m}$, $\mathcal{L}=2200\,\mathrm{m}$, and $\mathcal{T}=2\,\mathrm{h}$, which yields an average gas flux of $0.37\,\mathrm{m^3s^{-1}}$.

These results are given for the early stage of the tide. The later stage probably does not contribute to the aeration of intermediate water in the Strait of Georgia as the water coming from Haro Strait may be too diluted to reach intermediate depths and is therefore not of

immediate interest for our considerations. Its contribution to the aeration of the surface water can be estimated on the base of similar arguments as before. At that stage, the area of bubble injection is spread over an average distance of about 1000 m. The area over which downwelling occurs was estimated from vertical currents measured with an ADCP as well as from observations with an echo sounder showing bubble plumes drawn down by the currents. The downwelling area is between 1% and 10% of the total area of the front, with vertical velocities between $-0.1\,\mathrm{m\,s^{-1}}$ and $-0.15\,\mathrm{m\,s^{-1}}$, yielding a minimal oxygen flux of $0.002\,\mathrm{m^3 s^{-1}}$ and a best guess of $2.3\,\mathrm{m^3 s^{-1}}$.

It should be kept in mind though that the values derived for the oxygen flux in the tidal front at Boundary Pass are – due to the many uncertainties – only rough estimates. In addition, seasonal and spring neap tidal variations have not been considered.

Contribution of all tidal fronts in Haro Strait

The results from the tidal front at Boundary Pass can now be used to estimate how much the other tidal fronts in Haro Strait contribute to the aeration of water. A parcel of water may be advected past several of the tidal fronts and may therefore gain oxygen more than once.

About 9 ebb and 6 flood tidal fronts are located in the estuary (Figure 1.6). We will ignore the weaker fronts and only look at the ebb tidal fronts at Stuart Island (0.5), Battleship Island (0.3), Gooch Island (0.2), and Discovery Island (0.2), as well as the flood tidal fronts at Boundary Pass (1) and Stuart Island (0.2).

Aerial photos and measurements during the research cruises 9934 and 0023 (Section 2.1) were used to map the extent of the fronts and to get some idea of the amount of entrained gas. The values in parenthesis behind the fronts provide a rough – and somewhat subjective – estimate of the relative importance of these fronts for the aeration of water. The oxygen flux in all fronts in Haro Strait is therefore about 2.5 times the one at Boundary Pass,

yielding about $0.92\,\mathrm{m^3 s^{-1}}$ ($0.005\,\mathrm{m^3 s^{-1}}$ as minimal value; Table 7.1).

7.2 Comparison with other oxygen sources

The oxygen flux calculated for the tidal fronts will now be compare with other sources supplying oxygen to the Fraser Estuary. These possible sources are diffusion through the sea surface, bubble injection by breaking waves outside tidal fronts, advection by currents, as well as photosynthesis.

7.2.1 Diffusive gas flux

Gases are exchanged between ocean and atmosphere by diffusion through the sea surface. The direction and strength of diffusion depends on the difference between the partial pressure of gas in atmosphere P_j and water P_{w_j} (Keeling (1993), Section 5)

$$Q_{mol_j} = k_j S_j \left(P_j - P_{w_j}\right) \quad , \tag{7.2}$$

where Q_{mol_j} describes the gas flux between ocean and atmosphere in number of moles per square meter and second. k_j is the gas transfer velocity and S_j the solubility. With $P_{w_j} = (1+0.01\sigma_j)\,\chi_j\,p_{atm}$ and $P_j = \chi_j\,p_{atm}$ (Section 5), we get

$$Q_{mol_j} = -0.01\sigma_j\,k_j S_j \chi_j\,p_{atm} \quad , \tag{7.3}$$

where p_{atm} is the atmospheric pressure, χ_j the molefraction in dry air, R the universal gas constant, T the temperature in Kelvin, and σ_j the percentage oversaturation in water. The equivalent volume under atmospheric pressure is given by the ideal gas law as

$$Q_{vol_j} = \frac{Q_{mol_j} R T}{p_{atm}} \quad . \tag{7.4}$$

Observations suggest that the gas transfer velocity k_j in equation (7.2) depends on the wind speed u_*. It is given by Liss & Merlivat (1986) for three different wave regimes: for smooth

water, rough water (without wave breaking), and wave breaking. The latter includes the contribution of bubbles generated by breaking wind waves. For each of these regimes, the authors fitted a linear relationship between wind speed and k_j to observations obtained in tank experiments and field measurements

$$\begin{aligned} k_j &= 0.17 u_* \left(\frac{660}{Sc_j}\right)^{2/3} && \text{for} \quad u_* \leq 3.6\,\mathrm{m\,s^{-1}} \quad , \\ k_j &= (2.85 u_* - 9.65)\sqrt{\frac{660}{Sc_j}} && \text{for} \quad 3.6\,\mathrm{m\,s^{-1}} < u_* \leq 13\,\mathrm{m\,s^{-1}} \quad , \\ k_j &= (5.9 u_* - 49.3)\sqrt{\frac{660}{Sc_j}} && \text{for} \quad 13\,\mathrm{m\,s^{-1}} > u_* \quad . \end{aligned} \tag{7.5}$$

$Sc_j = \nu / D_j$ is the Schmidt number, which is scaled with the Schmidt number $Sc = 660$ for CO_2 in salt water (Wanninkhof, 1992). ν is the water kinematic viscosity and D_j the dissolution coefficient.

Wanninkhof (1992) noted the importance of variable winds for determining the transfer velocity and chose a different description based on a quadratic relationship between k_j and wind speed (for a steady wind)

$$k_j = 0.31 u_*^2 \sqrt{\frac{660}{Sc_j}} \quad . \tag{7.6}$$

These two different descriptions of the transfer velocity will be used in the following to calculate the diffusive air-sea gas exchange in the Fraser estuary (Equations (7.3) and (7.4)). The resulting gas flux is plotted for the gases O_2 and N_2 in Figure 7.2 as function of wind speed and for a saturation of 95%, showing that the description by Wanninkhof (1992) yields higher values of the gas flux.

The saturation of gas in water is important for calculating the gas flux into the estuary, as shown by the linear relationship between (percentage) oversaturation and diffusive gas flux (Equation (7.3)).

The hydrographic observations presented by Crean & Ages (1971) were used to estimate

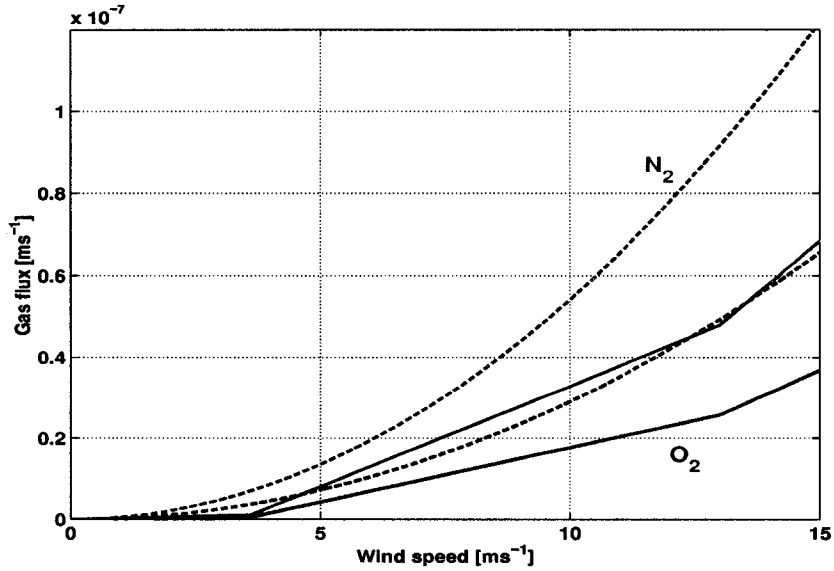

Figure 7.2: *Diffusive gas flux per square meter for O_2 (blue) and N_2 (red) as function of wind speed according to Liss & Merlivat (1986) (solid line) and Wanninkhof (1992) (dashed line) for an assumed saturation of 95%.*

the oxygen saturation of the surface layer in Juan de Fuca Strait and the Strait of Georgia (Figure 7.3). The data show strong regional differences with oxygen saturation levels increasing with distance from the Pacific Ocean. In Juan de Fuca Strait, the seasonal changes are moderate with a yearly mean value of about 83% (station #69 in Crean & Ages (1971)), while in the protected waters of the Strait of Georgia, seasonal effects like the warming or cooling of the surface layer as well as river runoff fluctuations of the Fraser River, are more important. Mean O_2-saturation values change from 94% in winter (station #3 in Crean & Ages (1971)) to oversaturated conditions (~109%) in summer (March to August), which may be caused by input from the Fraser River, oxygen production by algae (Section 7.2.2), or by warming of the water.

The data of both stations are fitted with a polynomial of third order (Figure 7.3), which is then used to describe the seasonal changes of the oxygen saturation levels for the calculation of the diffusive gas flux. For Haro Strait, an average of both stations is taken.

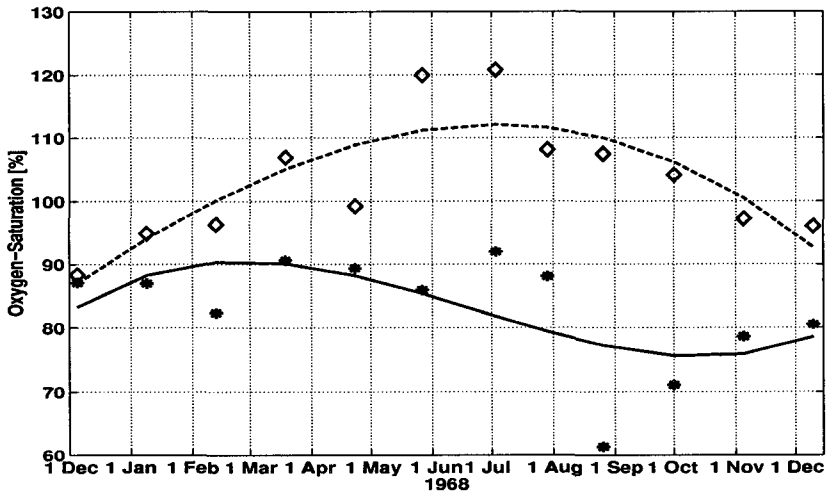

Figure 7.3: O_2*-saturation in 1968 for Juan de Fuca Strait (*, solid line) and the Strait of Georgia (◇, dashed line) estimated from Crean & Ages (1971) and shown together with a fitted polynomial of third order*

Hourly wind speed measurements from 1998 at Sandhead, Strait of Georgia (Figure 7.4a), are taken to compute the transfer velocity k_j according to the parameterizations by Liss & Merlivat (1986) (7.5) and Wanninkhof (1992) (7.6). The data may not be representative for the whole estuary, but still provide an estimate of the present wind conditions. The volume flux of gas per square-meter Q_{vol} is calculated with equations (7.3) and (7.4) and is then multiplied with the surface area of the straits yielding the diffusive gas flux for the whole Fraser Estuary Q_{diff} (Figure 7.4b). The surface area of the Strait of Georgia is about $6\,800\,km^2$, and $3\,700\,km^2$ for Juan de Fuca Strait (Thomson, 1994). The surface area of Haro Strait and the adjacent smaller straits is an estimated $450\,km^2$.

The resulting values are listed in Table 7.2 suggesting that a) the Strait of Georgia loses oxygen by diffusion in summer; b) Juan de Fuca Strait always takes up oxygen by diffusion; and c) the O_2-budget of the whole Fraser Estuary is characterized by 2 distinct seasons: summer (March–August) with no significant O_2-loss or uptake and winter (September–February) with a significant gain of O_2 by diffusion.

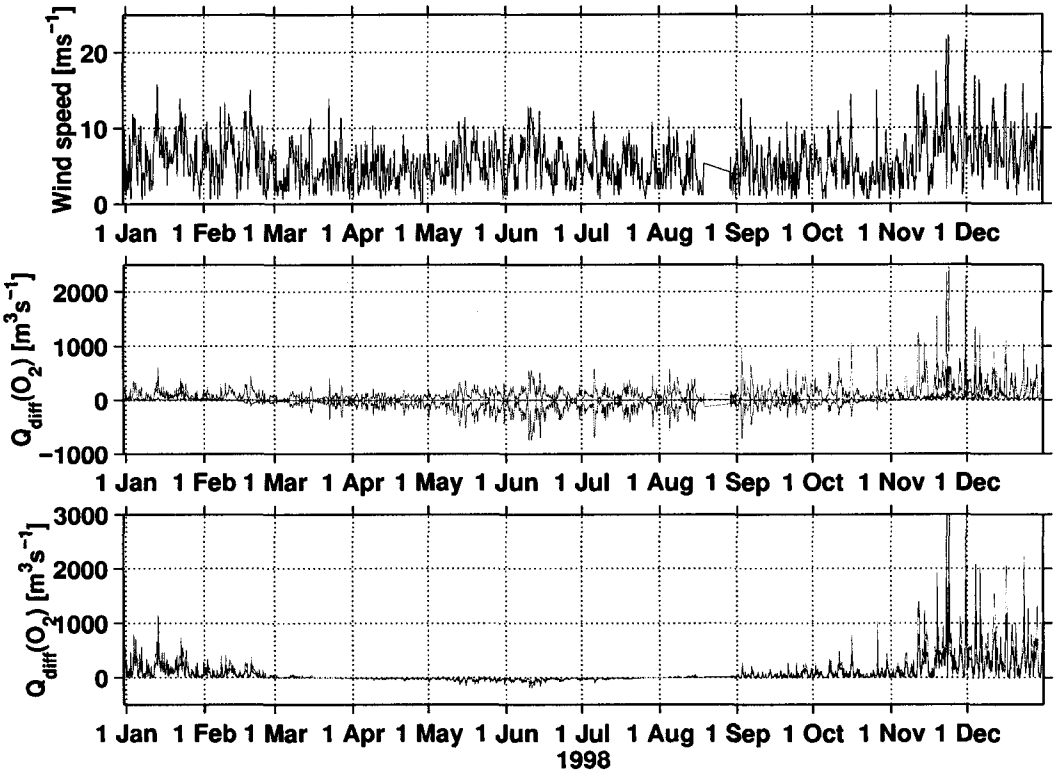

Figure 7.4: *a) Wind speed in the Fraser Estuary measured at Sandhead in 1998. b) Diffusive oxygen flux calculated for Juan de Fuca Strait (red), Strait of Georgia (green), and Haro Strait (blue; positive values are oxygen gain). c) The oxygen flux for the total estuary (blue) is compared to the oxygen flux according to Liss & Merlivat (1986). The corresponding saturation levels are shown in Figure 7.3.*

However, it should be kept in mind that the presented results are only rough estimates of the diffusive oxygen flux. Wind and saturation data are taken from different (possibly untypical) years and at only a few stations, which may not be representative for the conditions of the whole estuary. Nevertheless, the presented numbers give some idea of the order of magnitude of the diffusive gas flux and will later be compared with other oxygen sinks and sources.

	Area [km^2]	$Q_{diff}(O_2)$ [m^{3}s^{-1}] Liss & Merlivat (1986)	$Q_{diff}(O_2)$ [m^{3}s^{-1}] Wanninkhof (1992)
Juan de Fuca Strait	3 700[1)]	87	147
Haro Strait	450[2)]	5	8
Strait of Georgia	6 800[1)]	-23	-40
Total	10 950	68	115

Table 7.2: *Surface area and calculated mean diffusive gas flux for Juan de Fuca Strait, Haro Strait, and Strait of Georgia calculated according to Liss & Merlivat (1986) and Wanninkhof (1992).* [1)] *Taken from Thomson (1994).* [2)] *Estimated.*

7.2.2 Biological oxygen production and consumption

Oxygen production

Algae are known to play an important role in global oxygen production. They produce oxygen through photosynthesis: solar energy is used to remove carbon from CO_2, which is then attached to a water molecule forming a carbohydrate and leaving an O_2-molecule behind (Kirke, 1994)

$$CO_2 + 2\,H_2O + \text{Solar Energy} \rightarrow CH_2O + H_2O + O_2 \quad . \tag{7.7}$$

For every mole of carbon which is stored as carbohydrate about one mole of O_2 is released (the ratio of O_2/CO_2 is not exactly 1, but between 1.1 and 1.2, as CH_2O is only roughly the average composition of plant biomass). Primary production rates (usually given in mgC m^{-2}d^{-1}) can then be converted to oxygen production rates as C has a molar mass of 12.01 g, and a mole of O_2 takes up a volume of 22.4 l at a pressure of 101 325 Pa and a temperature of 0°C.

The Fraser Estuary is one of the most productive areas in the Pacific Ocean with mean annual primary production rates of 590 mgC m^{-2}d^{-1} (Puget Sound, located at the southern side of the estuary), 944 mgC m^{-2}d^{-1} (Strait of Georgia), and 100 mgC m^{-2}d^{-1} (Juan de

Fuca Strait) (Koblents-Mishke, 1965). These strong regional differences are also apparent in Figure 7.5 showing summer values of cholorphyll-a concentrations in the Fraser Estuary. The values in the Strait of Georgia are significantly higher than the ones in Juan de Fuca Strait due to higher water temperatures and calmer weather/sea state conditions.

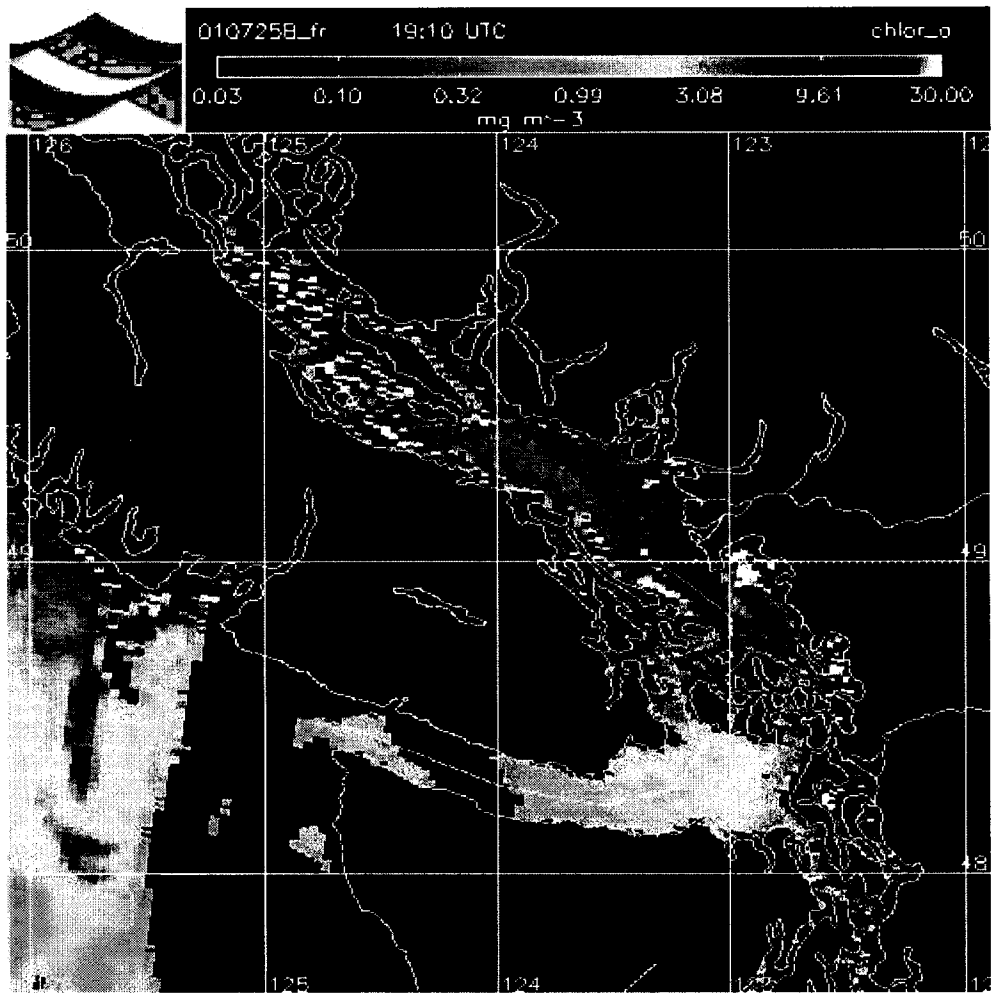

Figure 7.5: *Chlorophyll-a concentration in the Fraser Estuary in July 2001 (Figure provided by R.Pawlowicz, UBC, Canada, as part of STRATOGEM).*

Primary production rates also vary significantly over the year. In summer, they can be as high as $1260\,\mathrm{mgC\,m^{-2}d^{-1}}$ in Puget Sound (Figure 7.6), while winter values are only about

$280\,\mathrm{mgC\,m^{-2}d^{-1}}$ (Koblents-Mishke, 1965). The seasonal differences are caused by changes in solar radiation, water temperature, and possibly nutrient supplies.

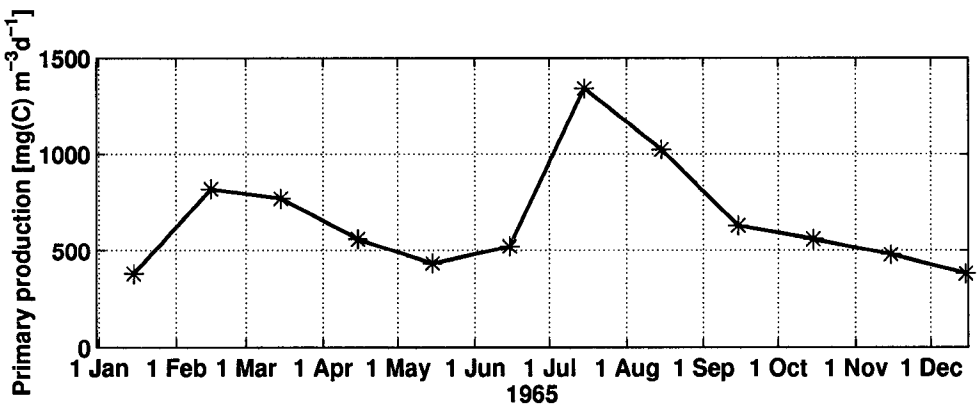

Figure 7.6: *Primary production rates in Puget Sound, WA, USA, in 1965, estimated from Koblents-Mishke (1965).*

The resulting mean oxygen production by photosynthesis Q_{phot} in the Fraser Estuary is listed in Table 7.3. For Haro Strait, a mean primary production rate of $520\,\mathrm{mgC\,m^{-2}d^{-1}}$ is assumed, a value between the ones for Juan de Fuca Strait and the Strait of Georgia and in qualitative agreement with Figure 7.5. The O_2-production rates are of the same order of magnitude as the diffusive gas flux (Table 7.2) and will be compared to it in more detail below.

Oxygen consumption

After the algae die off, they sink to the sea floor where they are decomposed – a process for which oxygen is needed. This could account at least partly for the low oxygen values in the deep part of the Strait of Georgia (Figure 1.8). Dissolved O_2-levels below 250–300 m reach values close to $2\,\mathrm{ml\,l^{-1}}$, which is considered to be the critical level for fish (The Swedish Environmental Protection Agency, 2003), but many fish are also significantly affected and attempt to leave the area at oxygen levels of $2-4\,\mathrm{ml\,l^{-1}}$. It is likely that O_2 is primarily

	Area [km^2]	Primary prod. [$mgC\,m^{-2}d^{-1}$]	$Q_{phot}(O_2)$ [m^3s^{-1}]
Juan de Fuca Strait	3 700[1)]	100	8
Haro Strait	450 [2)]	522	5
Strait of Georgia	6 800[1)]	944	139
Total	10 950	–	152

Table 7.3: *Surface area, primary production rates, and calculated mean oxygen production by photosynthesis Q_{phot} for Juan de Fuca Strait, Haro Strait, and the Strait of Georgia.* [1)] *Taken from Thomson (1994).* [2)] *Estimated.*

supplied to this region by diffusion of oxygenated water from intermediate depths (see also Section 7.2.3), or by short deep water renewal events by inflow from the Pacific Ocean (Masson, 2002). This is discussed in more detail in Section 7.2.4.

7.2.3 Oxygen advection

Oxygen is advected into the Fraser Estuary mainly through Juan de Fuca Strait, but also through some narrow passages at the northern end of the Strait of Georgia (Johnston Strait), and by the Fraser River.

At the entrance of Juan de Fuca Strait, oxygen levels are lower in the layer of inflowing Pacific water than in the upper layer as shown by monthly data set from 1969 by Crean & Ages (1971) and by observations in July 2000 by D. Masson (Figure 1.8). Annual mean oxygen levels of the lower layer are about $3.2\,ml\,l^{-1}$ and about $4.9\,ml\,l^{-1}$ for the upper layer. Multiplied with a lower layer transport of $100\,000\,m^3\,s^{-1}$ and a upper layer transport of $104\,400\,m^3\,s^{-1}$(Thomson, 1994) this yields an oxygen loss of $-190\,m^3\,s^{-1}$.

The Fraser River discharge varies between $1000\,m^3s^{-1}$ in winter and $10\,000\,m^3s^{-1}$ in late spring, with a mean value of $4\,400\,m^3s^{-1}$ (Thomson, 1994). It is likely that oxygen levels are close to saturation, so that an assumed value of $7.0\,ml\,l^{-1}$ would yield a mean oxygen input of $30\,m^3\,s^{-1}$.

The inflow/outflow at the northern end of the estuary through Johnstone Strait is about $30\,000\,m^3s^{-1}$ (Pawlowicz, 2002). Also here, no oxygen data are available. However, due to the very strong tidal currents, intense eddy activity, and bubble entrainment in the narrow channels around Johnstone Strait, we can assume that the inflow is highly oxygenated with values between $6.0\,ml\,l^{-1}$ and $7.0\,ml\,l^{-1}$. The outflow has an estimated oxygen level of $4.5\,ml\,l^{-1}$ (Crean & Ages, 1971), so that the difference between inflow and outflow is about $2.0\,ml\,l^{-1}$. The resulting oxygen input into the Fraser Estuary is then $60\,m^3\,s^{-1}$, which is probably a more conservative upper value.

Fraser Estuary	Oxygen flux $[m^3\,s^{-1}]$
Juan de Fuca Strait	-190
Fraser River	30
Johnstone Strait	60
Total	-100

Table 7.4: *Estimated mean annual advection of oxygen into the Fraser Estuary and Haro Strait.*

For the overall budget of the estuary (Table 7.4) advection is therefore an oxygen sink with an oxygen flux of $-100\,m^3\,s^{-1}$. However, for the supply of oxygen to intermediate depths in the Strait of Georgia, it is more important to know how much oxygen is advected into Haro Strait and Boundary Pass, where it is then mixed with dense bottom water before flowing into the Strait of Georgia. However, due to the strong tidal currents and mixing in Haro Strait, it is even more difficult to estimate the contribution of advection in that region. The sparse data does therefore not allow for a somewhat reliable estimate of the oxygen flux due to advection so that no comparison to the contribution of tidal fronts can be made.

7.2.4 Summary

We can now compare the importance of the different oxygen sources with each other. The values for diffusion, photosynthesis, advection, and tidal fronts are listed in Table 7.5. If we look at the whole Fraser Estuary, we see that diffusion and advection balance each other out, while photosynthesis supplies most oxygen to the estuary. The contribution of the tidal fronts is with 1.6% minor. We may estimate the oxygen consumption by decomposition of organic material by closing the budget, yielding about $-150\,\mathrm{m^3 s^{-1}}$.

Oxygen-Source/Sink	Fraser Estuary	**Strait of Georgia**
Diffusive gas flux	92	**6.5**
Photosynthesis	152	**5**
Advection	-100	?
Biological decomposition	-150 (?)	?
Tidal front at Boundary Pass	2.8 (model >0.1)	**0.4 (model 0.1)**
Tidal fronts in Haro Strait	3.2 (model >0.25)	**0.9 (model 0.25)**

Table 7.5: *Oxygen sources $[m^3\,s^{-1}]$ for the Fraser Estuary and the Strait of Georgia. For the diffusive gas flux, a mean value is given.*

However, for the aeration of intermediate water in the Strait of Georgia we have to look at the values in Haro Strait. The aerated surface water in the Strait mixes with dense water from the Pacific Ocean. This oxygenated water mass is then advected over the sill at Boundary Pass into intermediate depths in the Strait of Georgia (Figure 7.7).

The oxygen levels in the lower layer in Haro Strait and in intermediate depths in the Strait of Georgia are both about $4.5\,\mathrm{ml\,l^{-1}}$ (Figure 1.8). The additional oxygen brought into the Strait with the tongue of oxygenated water is therefore supplied by the aerated surface water from Haro Strait. Diffusion and photosynthesis contribute to it about the same amount of oxygen. The tidal fronts are now much more important with a portion of about

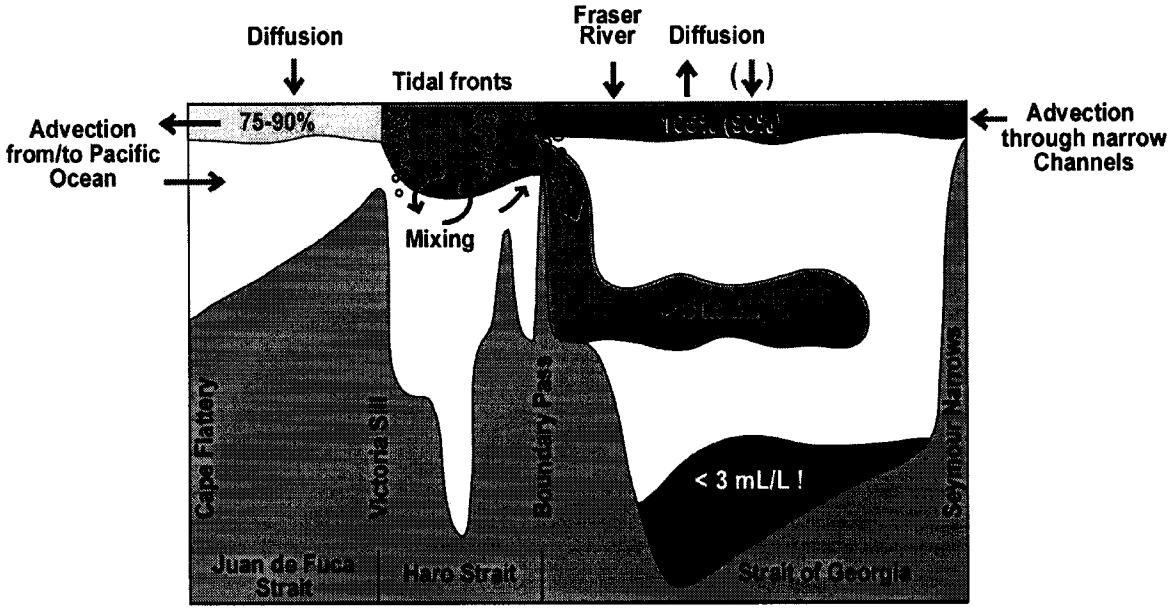

Figure 7.7: *Sketch of the oxygen sources and sinks in the Fraser Estuary.*

7% (again, taking the best guess). The tidal front at Boundary Pass contributes by itself 3%. This means that the oxygen concentration of the newly subducted intermediate water in the Strait of Georgia would be about $0.035\,\mathrm{ml\,l^{-1}}$ smaller without the contribution of the tidal fronts, if a 1:1 mixing ratio between aerated surface water and the dense water in Haro Strait is assumed.

The presented results suggest that the tidal fronts in Haro Strait may contribute significantly to the aeration of intermediate water in the Strait of Georgia. It should be kept in mind, however, that the results are rather uncertain in many respects. It would therefore be desirable to verify this conclusion in the future with additional measurements.

8 Application to other areas with strong tidal currents or flow convergence

Bubble induced air-sea gas exchange in tidal fronts is not only a common feature of the coastal waters of British Columbia, but is probably also found in other coastal environments where strong tidal currents interact with a rugged topography such as in the Strait of Messina, Italy, and the Bay of Fundy, Canada. These will be described below. Air-sea gas exchange by gas bubbles in tidal fronts may also be important in Ireland, Norway, Chile, Japan, and the North Sea (Wadden Sea).

The importance of bubble induced gas flux depends on the extent of tidal fronts as well as the bubble penetration depth, current speed, and stratification, and has to be compared with other oxygen sources and sinks (diffusive and advective gas flux, biological production/consumption, etc.) in the considered estuary. In general, bubble induced air-sea gas exchange is more important in estuaries with a small surface area and numerous tidal fronts than in large estuaries with only a few fronts.

But tidal fronts can also serve as a mechanism to contribute oxygen to water masses below the surface layer – either by bubble penetration depths exceeding the surface layer thickness or by subducting flows in association with the front. This may be especially important in anaerobic estuaries or regions of abundant marine life.

However, the processes which are important for the subduction of gas bubbles – converging flows enhancing bubble generation by wave breaking and associated downwelling currents – can also occur in the open ocean in form of Langmuir circulations or deep convection and will therefore be mentioned at the end of this Section.

8.1 Strait of Messina, Italy

Sicily and the Italian mainland are separated by the Strait of Messina. It is characterized by a 5 km wide contraction and a sill of 60 m depth, 5 km further to the South (Figure 8.1).

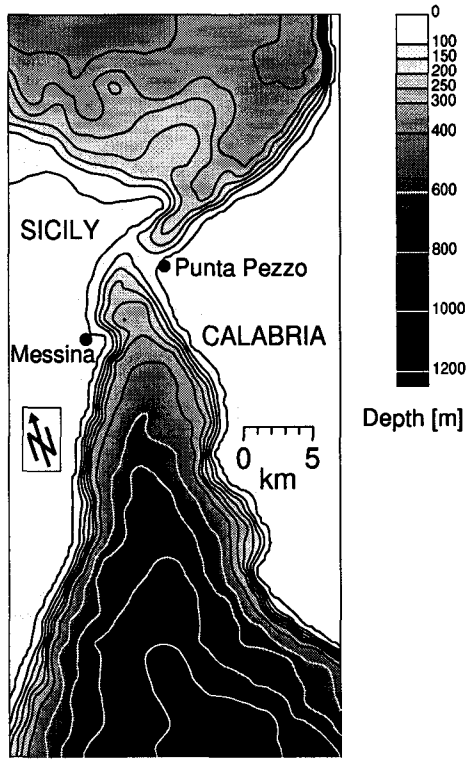

Figure 8.1: *Map of the Strait of Messina, Italy (adapted from Brandt* et al. *(1999)).*

Although the tidal amplitude in the Mediterranean Sea is only on the order of 10 cm, it drives strong currents of up to $3\,\mathrm{m\,s^{-1}}$ through the Strait, because the tidal regimes on both sides have a phase difference of about 180°.

Usually, the surface water in the South is denser than in the North of the Strait. However, during the observations on October 25, 1995, an increased inflow of light Atlantic Water into the Mediterranean reversed the density gradient along the Strait.

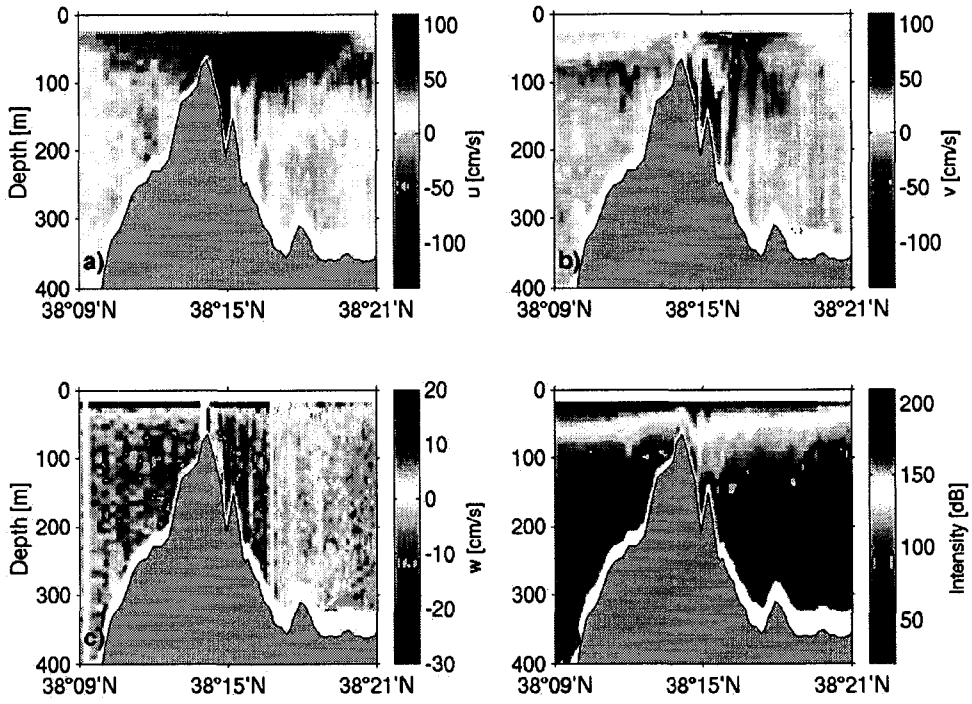

Figure 8.2: *Northward tidal flow through the Strait of Messina on October 25, 1995 (data from P. Brandt, IfM Kiel, Germany). a) Along-strait current; b) across-strait current; c) vertical current; d) acoustic backscatter intensity.*

The measurements show a northward flowing tidal current (Figure 8.2) shooting over the sill with a horizontal speed of up to $1.5\,\mathrm{m\,s^{-1}}$. Although the measurements are noisy and the spatial resolution is quite limited, they show an increase in acoustic backscatter intensity at the downstream side of the sill. It is not clear, if this is due to the entrainment of gas bubbles or – more likely – to the lowering of the interface due to hydraulic effects or internal waves travelling from the sill into northward direction (Brandt *et al.*, 1999). But even if gas bubbles were entrained, the oxygenated water still remained in the surface layer and does not contribute oxygen to some intermediate water mass.

However, during southward tidal flow, denser water from the North is flowing as surface

water over the sill plunging down into intermediate depths of $\sim$ 100 m (Brandt *et al.*, 1999) as it meets the lighter water in the South. The transition between surface water at the sill and intermediate depths to the South of it has to be associated with some kind of tidal front similar to the one at Boundary Pass (Chapter 2.2) or Battleship Island (Chapter 2.3.2). It can therefore be expected that also in the Strait of Messina, gas bubble clouds are injected into the ocean in a tidal front contributing to the oxygenation of intermediate water.

Although the physical processes seem to be the same as at Boundary Pass, the fronts in the Strait of Messina are negligible for the overall gas exchange in the Mediterranean Sea as the amount of entrained gas has to be compared to other sources/sinks over the whole ocean basin.

8.2 Bay of Fundy, Eastern Canada

The Bay of Fundy in Eastern Canada is well known for the world's highest tidal amplitudes of up to 16 m. These are associated with strong tidal currents.

Grand Manan Island (Figure 8.3) is located at the entrance of the Bay forming an obstacle for the tidal flow. At flood tide, the flow forms a pronounced tidal front at the northern tip of the island ("The long eddy") extending for $\sim$ 5 km to the North-East. This front seems to be a preferred place for foraging harbour porpoises as well as other whales (pers. communication D. Johnston, Duke Marine Lab, NC, USA).

The front is similar to the one at Stuart Island (Section 2.3.1), with two water masses being separated by a vertical front line, which may tilt further downstream (Northeast) due to restratification processes. In the frontal zone – which is indicated by the red arrows in Figure 8.4 – eddies are formed due to the high horizontal shear. There, areas of high acoustic backscatter intensity indicate clouds of gas bubbles which are drawn down by the eddies and vertical currents to depths of more than 35 m.

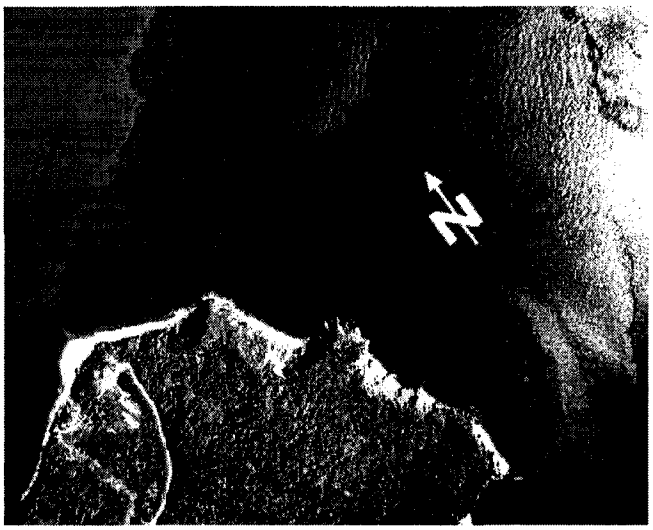

Figure 8.3: *Aerial view of the flood tidal front at the Northern tip of Grand Manan Island, Bay of Fundy, NB, Canada. The main flow direction is indicated by the red arrows (photo: Dave Johnston, Duke Marine Lab, NC, USA).*

8.3 Langmuir circulation, deep convection

Also other mechanisms than tides form convergence zones at the sea surface which may enhance the bubble formation by wave-current interaction as well as the downward transport of bubbles and aerated water.

It has been suggested by Thorpe (1982) that the downwelling currents associated with Langmuir circulations increase the penetration depths of gas bubbles. Consequently, the gas exchange is also enhanced as suggested by model calculations in Section 6. Langmuir circulations have a typical vertical scale of 10-15 m, so that these processes are limited to the upper ocean.

In the Labrador Sea, Irminger Sea, Greenland-Iceland-Norway-Sea, and the Gulf of Lions (Northern Mediterranean), deep water is formed by convection in some winters. The convection chimneys have a diameter $< 20\,\mathrm{km}$ with downwelling currents of $5-10\,\mathrm{cm\,s^{-1}}$ (Schott *et al.*, 1999). The divergence/convergence patterns may increase wave breaking and

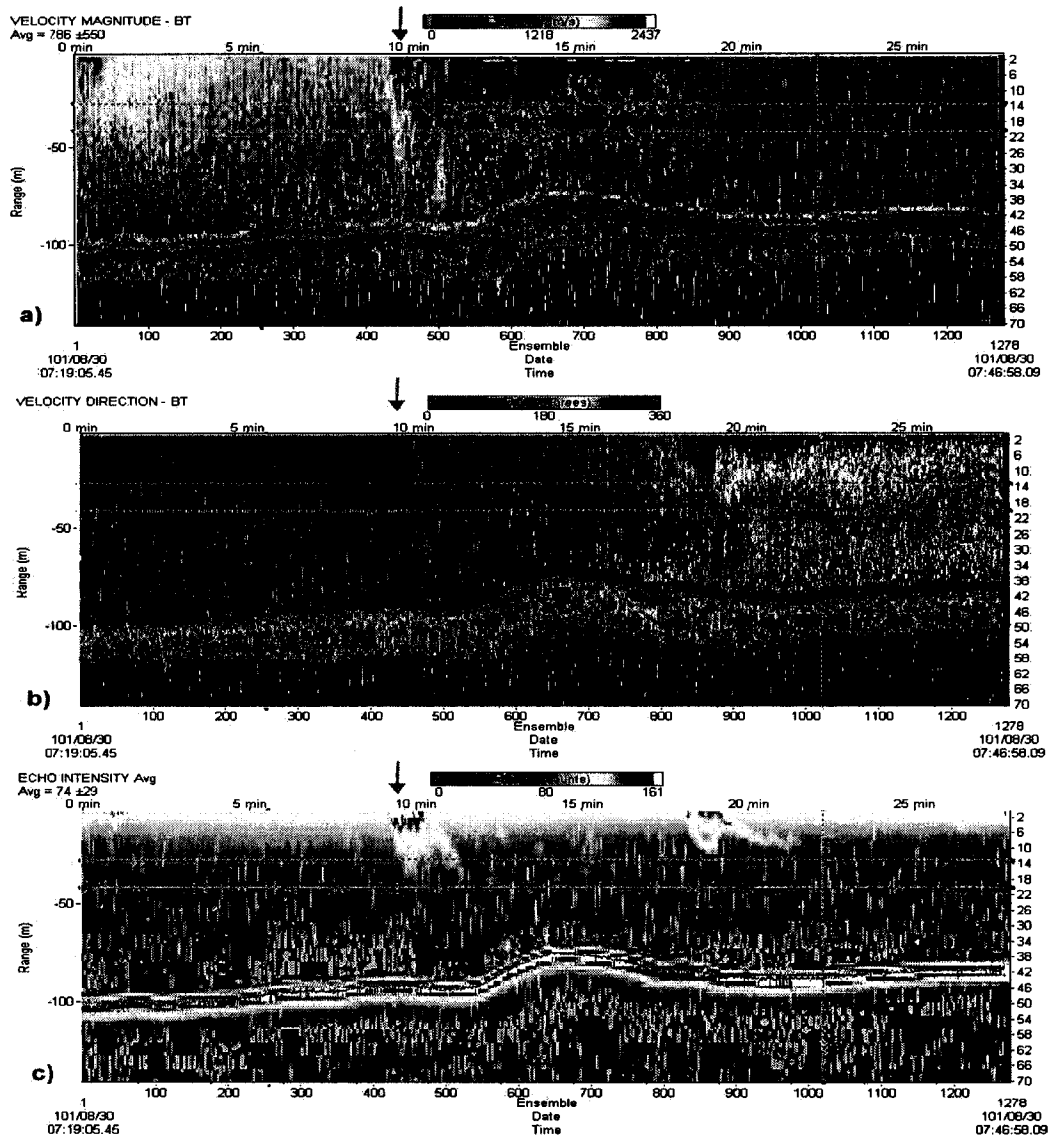

Figure 8.4: *ADCP-section through the tidal front at Grand Manan Island (Figure from Dave Johnston, Duke Marine Lab, NC, USA). The section is taken from Southeast (left) to Northwest (right). a) Velocity magnitude [$\mathrm{mm\,s^{-1}}$]; b) velocity direction [°]; c) backscatter intensity [dB].*

the formation of gas bubbles which may be transported downwards by the convective water. Gases as O_2, CO_2, and freon (as an oceanographic tracer) may then be carried down to depths of more than 1500 m, forming a direct connection between surface waters and deep ocean.

9 Conclusions and outlook

Intense ship-board observations have been carried out in Haro Strait during two research cruises in October 1999 and September 2000 in order to study the dynamics of the hydraulic sill flow at Boundary Pass and to measure the contribution of tidal fronts to the aeration of the Fraser estuary. Measurements were made at the tidal fronts at Stuart Island, Battleship Island, and Boundary Pass with an ADCP, a (towed) CTD, an echo sounder, and an acoustical resonator for measuring bubble size distributions.

The investigations concentrated on the processes at the flood tidal front at Boundary Pass, because of its potential importance for the aeration of intermediate and deep water in the Strait of Georgia. At flood tide, dense water from the Pacific Ocean is pushed over the sill where it mixes with aerated surface water. At the early stage of the tide (0-2 h after slack tide), this water flows as a hydraulic flow over the sill into intermediate depth. The flow is a strongly forced two-layer flow with an arrested upper layer of stagnant water. The current speeds in the active lower layer reach up to $1.5\,\mathrm{m\,s^{-1}}$ in the horizontal and $0.75\,\mathrm{m\,s^{-1}}$ in the vertical. Intense detrainment of water from the lower into the upper layer causes a volume loss of 60% between sill crest and the bottom of the sill over a horizontal distance of 200 m.

A pronounced tidal front forms at the location of the lower layer plunge point 120 m downstream of the sill crest. Surface waves travelling into this convergence zone tend to steepen and break creating gas bubbles, which are then drawn down by the strong vertical currents. It is a process which enhances the air-sea gas exchange.

At 2-4 h after slack tide, the tidal currents increase to $3\,\mathrm{m\,s^{-1}}$. The flow shoots over the sill separating at the sill crest. The front line is now diffuse and is pushed far downstream by the currents. Gas bubble clouds indicating downwelling currents are spread over a horizontal

distance of about 2 km. It is not clear if the water flowing over the sill is at this stage still dense enough to reach intermediate depths, as it is diluted by intense mixing downstream of the sill crest.

The hydraulic flow at the early stage of the tide has been modeled with a two-layer model for inviscid and steady flow. It is based on the Bernoulli equation and has been adapted from Farmer & Armi (1999). The results show that the interface depth calculated for a high volume loss due to detrainment can be explained by the model in principle, although the derived current speeds are too high. For a more accurate description, better boundary conditions, derived from observations of the horizontally changing detrainment velocity and reduced gravity, are needed.

The steepening of surface waves due to wave-current interaction in the convergence zone of the tidal front has been modeled with a one-dimensional model by Bretherton & Garrett (1969). The energy dissipated by wave breaking was then calculated and the size distribution of injected gas bubbles determined. It depends on the amount of dissipated energy which goes into the subduction of bubbles, the bubble entrainment depth, and the assumed spectral slope of the initial size distribution. Values for these parameters were derived from the literature.

The behaviour of gas bubbles in a fluid is described with a model by Thorpe (1982). It shows that gas bubbles which were observed at a depth of 160 m at Boundary Pass must have had a radius of at least 2 mm when they were injected at the surface, and that they were drawn down by vertical currents exceeding $0.27\,\mathrm{m\,s^{-1}}$.

The enhancement of air-sea gas exchange by vertical currents is investigated, leading to a bulk description of gas bubble behaviour. This description allows us to calculate gas exchange from the total injected void fraction instead of tracking the dissolution of gas from single bubbles. The description can be used for temporarily or spatially varying flow fields and is applied to the conditions in the tidal front at Boundary Pass.

Bubbles injected within a few meters of the tidal front contribute to the aeration of inter-

mediate water in the Strait of Georgia. Calculations show that the waves which inject most bubbles in that zone have short wave lengths, if they approach from the West and relatively long wave lengths, if they approach from the East. The total oxygen flux in the tidal front at Boundary Pass has been estimated for different wind/wave conditions. A comparison of the results with observations, as well as with other oxygen sources in the Fraser Estuary shows that tidal fronts can contribute significantly to the air-sea gas exchange in an estuary.

Tidal fronts may be also important for the aeration of other estuaries where strong tidal currents interact with topography, as in Eastern Canada, Norway, Chile, or Japan. The investigated processes may be also important in regions of deep water formation, where convection chimneys can transport gases to depths $> 1500\,\mathrm{m}$.

Outlook

The bulk description of gas bubble behaviour introduced in Section 6 could be a useful tool for parameterizing the contribution of gas bubbles to air-sea gas exchange in (global) numerical models, as it provides a computationally very efficient way of describing bubble physics. However, for a successful application, a much better link between dissipated wave energy (and possibly wind speed or surface roughness) and bubble entrainment has to be established. The parameters which would have to be better determined by measurements are in particular the bubble entrainment depth and the portion of energy which goes into the subduction of bubbles.

Better measurements could also help to improve the understanding of near surface processes which are important for the entrainment and subduction of gas bubbles by downwelling currents. Gas bubbles can only be subducted if they are transported away from the surface to depths where the vertical currents are not zero. Eddies and "micro-convergence zones" at the edge of upwelling rings may be mechanisms for this in tidal fronts.

Many of the parameters relevant for estimating the air-sea gas exchange in tidal fronts could be also measured with a Lidar (Light detection and ranging) mounted on a small plane. It would provide quasi-synoptic information on the spatial extent of the front, wave height, as well as backscatter intensity in the upper 30-50 m of the water column providing information on gas bubble entrainment and possibly void fraction.

It would be certainly desirable to carry out additional measurements in the tidal fronts in Haro Strait as the observed processes suggest that they may contribute significantly to the aeration of water. The present results, however, are too uncertain to confirm this for sure.

The results could be further improved by calculating the gas exchange budget for other gases. Especially Ar is of interest as it has very similar physical characteristics to O_2, but is not influenced by biological processes, so that the oxygen production by photosynthesis may be determined.

Bibliography

ARMI, L. & FARMER, D. 1986 Maximal two-layer exchange through a contraction with barotropic net flow. *J. Fluid Mech.* **164**, 27–51.

ARMI, L. & FARMER, D. 2002 Stratified flow over topography: Bifurcation fronts and transition to uncontrolled state. *Proc. Roy. Soc.* **458, A**, 513–538.

BALDY, S. 1988 Bubbles in the close vicinity of breaking waves: statistical characteristics of the generation and dispersion mechanism. *J. Geopys. Res.* **93, C7**, 8239–8248.

BALDY, S. & BOURGUEL, M. 1987 Bubbles between the wave trough and wave crest levels. *J. Geopys. Res.* **92, C3**, 2919–2929.

BLANCHARD, D. & WOODCOCK, A. 1957 Bubble formation and modification in the sea and its meteorological significance. *Tellus* **9 (2)**, 145–157.

BRANDT, P., RUBINO, A., QUADFASEL, D., ALPERS, W., SELLSCHOPP, J. & FIEKAS, H.-V. 1999 Evidence for the influence of Atlantic-Ionian stream fluctuations on the tidally induced dynamics in the Strait of Messina. *J. Am. Met. Soc.* **29**, 1071–1080.

BRETHERTON, F. & GARRETT, C. 1969 Wavetrains in inhomogeneous moving media. *Proc. Roy. Soc.* **302, A**, 529–554.

BRETSCHNEIDER, C. 1958 Revisions in wave forecasting: deep and shallow water. In *Proceedings, 6th conference on coastal engineering council of wave research*, pp. 1–18. University of California, Berkeley.

CHANSON, H. & JAW-FANG, L. 1979 Plunging jet characteristics of plunging breakers. *Coastal Eng.* **31**, 125–141.

CRAWFORD, G. & FARMER, D. 1987 On the spatial distribution of ocean bubbles. *J. Geophys. Res.* **92, C8**, 8231–8243.

CREAN, P. & AGES, A. 1971 Oceanographic records from twelve cruises in the Strait of Georgia and Juan de Fuca Strait. *Dept. of Energy, Mines, and Resources, Marine Research Branch* **1-4**, 389.

DEANE, G. 1997 Sound generation and air entrainment by breaking waves in the surf zone. *J. Acoust. Soc. Am.* **102 (5)**, 2671–2689.

DEANE, G. 1999 Acoustic hot-spots and breaking wave noise in the surf zone. *J. Acoust. Soc.* **105 (5)**, 3151–3167.

DEANE, G. & STOKES, M. 1999 Air entrainment processes and bubble size distributions in the surf zone. *J. Phys. Oceanogr.* **29**, 1393–1403.

DEANE, G. & STOKES, M. 2002 Scale dependance of bubble creation mechanisms in breaking waves. *Nature* **418**, 839–844.

DONELAN, M., LONGUET-HIGGINS, M. & TURNER, J. 1972 Periodicity in whitecaps. *Nature* **239**, 449–451.

FAN, L.-S. & TSUCHIYA, K. 1990 Bubble wake dynamics in liquids and liquid-solid suspensions. In *The Role of Air-Sea Exchange in Geochemical Cycling* (ed. Butterworth-Heinmann). Stoneham, MA.

FAN, L.-S., YANG, G., LEE, D., TSUCHIYA, K. & X.LUO 1999 Some aspects of high-pressure phenomena of bubbles in liquids and liquid-solid suspensions. *Chem. Engin. Science* **54**, 4681–4709.

FARMER, D. & ARMI, L. 1986 Maximal two-layer exchange over a sill and through the combination of a sill and contraction with barotropic flow. *J. Fluid Mech.* **164**, 53–76.

FARMER, D. & ARMI, L. 1999 Stratified flow over topography: The role of small scale entrainment and mixing in flow establishment. *Proc. Roy. Soc.* **455, A**, 3221–3258.

FARMER, D., D'ASARO, E., TREVORROW, M. & DAIKIRI, G. 1995 Three-dimensional structure in a tidal convergence front. *Continental Shelf Res.* **15, 13**, 1649–1673.

FARMER, D., PAWLOWICZ, R. & JIANG, R. 2002 Tilting separation flows: a mechanism for intense vertical mixing in the coastal ocean. *Dyn. Atmos. Ocean* **36**, 43–58.

FARMER, D. & SMITH, J. 1980 Tidal interaction of stratified flow with a sill in Knight Inlet. *Deep-Sea Res.* **27A**, 239–254.

FARMER, D. & VAGLE, S. 1988 On the determination of breaking surface wave distributions using ambient sound. *J. Geophys. Res.* **93, C4**, 3591–3600.

FARMER, D., VAGLE, S. & BOOTH, A. 1998 A free-flooding acoustical resonator for measurement of bubble size distributions. *J. of Atm. and Oceanic Tech.* **15**, 1132–1146.

FISHERIES AND OCEANS CANADA 2000 Canadian tide and current tables.

FOREMAN, M. & THOMSON, R. 1997 Three-dimensional simulations of tides and buoyancy currents along the west coast of Vancouver Island. *J. Phys. Oceanogr.* **27**, 1300–1325.

GALVIN, C. 1968 Breaker type classification on three laboratory beaches. *J. Geophys. Res.* **73, 12**, 3651–3659.

GARGETT, A. & MOUM, J. 1995 Mixing efficiencies in turbulent tidal fronts: results from direct and indirect measurements of density flux. *J. Phys. Oceanogr.* **25**, 2583–2608.

GARRETT, C., LI, M. & FARMER, D. 2000 The connection between bubble size spectra and energy dissipation rates in the upper ocean. *J. Phys. Oceanogr.* **30**, 2163–2171.

HWANG, P., HSU, Y.-H. & WU, J. 1990 Air bubbles produced by breaking wind waves: a laboratory study. *J. Phys. Oceanogr.* **20**, 19–28.

JOHNSON, B. & COOKE, R. 1979 Bubble populations and spectra in coastal waters: a photographic approach. *J. Geophys. Res.* **84, C7**, 3761–3766.

KEELING, R. 1993 On the role of large bubbles in air-sea gas exchange and supersaturation in the ocean. *J. Mar. Res.* **51**, 237–271.

KIRKE, J. 1994 *Light and photosynthesis in aquatic ecosystems*, 2nd edn. Cambridge: Cambridge University Press.

KOBLENTS-MISHKE, O. 1965 Primary production in the Pacific Ocean. *Oceanology* **2**, 104–116.

KRAUSS, W. 1973 *Dynamics of the homogeneous and the quasihomogeneous ocean.* Berlin, Stuttgart: Gebrüder Borntraeger.

LAMARRE, E. & MELVILLE, W. 1991 Air entrainment and dissipation in breaking waves. *Nature* **351**, 469–472.

LAMARRE, E. & MELVILLE, W. 1994 Void-fraction measurements and sound-speed fields in bubble plumes generated by breaking waves. *J. Acoust. Soc.* **95 (3)**, 1317–1328.

LEBLOND, P., MA, H., DOHERTY, F. & POND, S. 1991 Deep and intermediate water replacement in the Strait of Georgia. *Atmos Ocean* pp. 288–312.

LISS, P. & MERLIVAT, L. 1986 Relationship between wind speed and gas exchange over the ocean. In *The Role of Air-Sea Exchange in Geochemical Cycling* (ed. P. Buat-Menard), , vol. 97, C5, pp. 113–129. D. Reidel, Hingham, Mass.

LOEWEN, M., O'DOR, M. & SKAFEL, M. 1996 Bubbles entrained by mechanically generated breaking waves. *J. Geophys. Res.* **101, C**, 20.759–20.769.

LONGUET-HIGGINS, M. 1969 On wave breaking and the equilibrium spectrum of wind-generated waves. *Proc. Roy. Soc.* **310, A**, 151–159.

MASSON, D. 2002 Deep water renewal in the Strait of Georgia. *Estuarine, Coastal, Shelf Science* **54**, 115–126.

MEDWIN, H. 1970 In situ acoustic measurements of bubble populations in coastal ocean waters. *J. Geophys. Res.* **75, 3**, 599–611.

MEDWIN, H. 1977*a* Acoustical determination of bubble-size spectra. *J. Acoust. Soc. Am.* **62,** 4, 1041–1044.

MEDWIN, H. 1977*b* Counting bubbles acoustically: a review. *Ultrasonics* pp. 7–13.

MEDWIN, H. & BREITZ, N. 1989 Ambient and transient bubble spectral densities in quiescent seas and under spilling breakers. *J. Geophys. Res.* **94, 9**, 12,751–12,759.

MELVILLE, W. & RAPP, R. 1985 Momentum flux in breaking waves. *Nature* **317 (10)**, 514–516.

MERLIVAT, L. & MEMERY, L. 1983 Gas exchange across an air-water interface: experimental results and modeling of bubble contribution to transfer. *J. Geophys. Res.* **88**, 707–724.

NEPF, H., WU, C. & CHAN, E. 1998 A comparison of two- and three-dimensional wave breaking. *J. Phys. Oceanogr.* **28**, 1496–1510.

PAWLAK, G. & ARMI, L. 1986 Mixing and entrainment in developing stratified currents. *J. Fluid Mech.* **424**, 45–73.

PAWLOWICZ, R. 2002 Observations and linear analysis of sill-generated internal tides and estuarine flow in Haro Strait. *J. Geophys. Res.* **107, C6**, 10,1029.

PAWLOWICZ, R. & FARMER, D. 1998 Diagnosing vertical mixing in a two-layer exchange flow. *J. Geophys. Res.* **103, C13**, 30.695–30,711.

PHILLIPS, O. 1977 *The dynamics of the upper ocean*, 2nd edn. Cambridge: Cambridge University Press.

PRATT, L. 1986 Hydraulic control of sill flow with bottom friction. *J. Phys. Oceanogr.* **16**, 1970–1980.

RDI 1989 Principles of operation: a practical primer. *RD Instruments* .

SCHOTT, F., VISBECK, M., SEND, U., FISCHER, J., STRAMMA, L. & DESAUBIES, Y. 1999 Observations of deep convection in the Gulf of Lions, Northern Mediterranean, during the winter 1991/92. *J. Phys. Oceanogr.* **26**, 505–524.

SVERDRUP, H. & MUNK, W. 1947 Wind, sea, and swell: theory of relations of forecasting. *Tech. Rep.* Publication 601. U.S. Navy Hydrographic Office.

TERRILL, E., MELVILLE, W. & SRAMSKI, D. 1998 Bubble entrainment by breaking waves and their effect on the inherent optical properties of the upper ocean. *SPIE Ocean Opt.* **14**, 1–11.

THE SWEDISH ENVIRONMENTAL PROTECTION AGENCY 2003 The swedish environmental protection agency. http://www.internat.environ.se.

THOMSON, R. 1994 Physical oceanography of the Strait of Georgia - Puget Sound - Juan de Fuca Strait system. *Symposium on the marine environment* pp. 36–98.

THORPE, S. 1982 On the clouds of bubbles formed by breaking wind-waves in deep water, and their role in air-sea gas transfer. *Phil. Trans. R. Soc. Lond.* **A304**, 155–210.

THORPE, S. 1984 A model of the turbulent diffusion of bubbles below the sea surface. *J. Phys. Oceanogr.* **14**, 841–854.

THORPE, S. 1986 Measurements with an automatically recording inverted echo sounder; aries and the bubble clouds. *J. Phys. Oceanogr.* **16**, 1462–1478.

THORPE, S. & STUBBS, A. 1979 Bubbles in a freshwater lake. *Nature* **279**, 403–405.

VAGLE, S. 1989 An acoustical study of the upper ocean boundary layer. PhD thesis, University of Victoria.

VAGLE, S. 2001 Bubble transport in rip currents. *J. Geophys. Res.* **106, C6**, 11,677–11,689.

WALDICHUK, M. 1957 Physical oceanography of the Strait of Georgia, British Columbia. *Fish. Res. Brd. Canada* **14 (3)**, 321–486.

WALLACE, D. & WIRICK, C. 1992 Large air-sea gas fluxes associated with breaking waves. *Nature* **356**, 694–696.

WANNINKHOF, R. 1992 Relationship between wind speed and gas exchange over the ocean. *J. Geophys. Res.* **97, C5**, 7373–7382.

WOOLF, D. & THORPE, S. 1991 Bubbles and the air-sea exchange of gases in near-saturation conditions. *J. Mar. Res.* **49**, 435–466.

WU, J. 1981 Bubble populations and spectra in near-surface ocean: summary and review of field measurements. *J. Geopys. Res.* **86, C1**, 457–463.

ZHU, D. & LAWRENCE, G. 1998 Non-hydrostatic effects in layered shallow water flows. *J. Fluid Mech.* pp. 1–16.

A Symbols and Abbreviations used

Hydraulic model

The indices $i=1,2$ stand for the upper and lower layer respectively. The subscript f marks properties at the frontal location and the subscript s properties at the end of sill slope.

B	Bottom depth	u_i	Hor. flow component $\perp$ sill crest
C_d	Drag coefficient	v_{ij}	Entrainment velocity
E	Bernoulli constant	w_i	Vert. current component
F_i	Froude number	x	Horizontal distance
g	Gravitational acceleration	z	Vertical distance
g'	Reduced gravity		
h_i	Layer thickness	α	Slope of interface
H	Mean lower layer thickness	δ	Portion of lost volume
L	Typical horizontal length scale	Δ	Total portion of lost volume
P_i	Hydrostatic pressure	η_1	Sea surface elevation
q_i	Volume flux	η_2	Interface depth
t	Time	ρ_i	Density of sea water

Bubble model

The indices $j = 1, 2, 3, 4$ stand for one of the gases O_2, N_2, CO_2, and Ar.

D_j	Coefficient of diffusion	T	Temperature
f	Frequency	t	Time
g	Gravitational acceleration	V	Volume
n_j	Number of moles	w	Vertical current speed
Nu_j	Nusselt number	w_b	Rise speed of gas bubble
P	Total pressure	w_{turb}	Turbulent current speed
p	Hydrostatic pressure	w^*	Turbulent vertical current scale
p_{atm}	Atmos. pressure at sea surface	z	Vertical distance
P_{w_j}	Partial pressure of gas in water	z^*	Turbulent length scale
Pe	Peclet number		
R	Ideal gas constant	γ	Surface tension coefficient
r	Bubble radius	ν	Water kinematic viscosity
r_{res}	Resonance radius	ρ	Density
Re	Bubble Reynolds number	σ_j	Oversaturation of gas in water
S_j	Solubility	χ_j	Molefraction in dry air

Wave model

a	Wave amplitude	t_*	Duration of wind
c	Phase speed	$\vec{u}$	Current speed vector
$\vec{c}_g$	Group speed vector	u	Horizontal current speed
c_g	Group speed	u_*	Wind speed
E	Total wave energy	$\mathcal{V}$	Void fraction
$\mathcal{E}$	Ratio of E_b to E_w	x	Horizontal distance
E_b	Energy for subducting bubbles	z	Depth
E_{pot}	Potential energy		
E_w	Energy lost by breaking	α	Spectral slope of size distrib.
$\mathcal{F}$	Wind fetch	β	Scaling factor of size distrib.
g	Gravitational acceleration	γ	Bubble entrainment depth
H	Water depth	η	Sea surface elevation
H_s	Significant wave height	κ	Wave number
N	Bubble size distribution	λ	Wave length
k	Wave number component along x	ϕ	Phase
r	Bubble radius	ρ	Density
$\mathcal{S}$	Wind stress factor	ω	Wave frequency
t	Time	τ	Wave period

Gas exchange in a convergence zone

a	Wave amplitude	t	Time
c	Phase speed of wave	u	Horizontal current speed
D	Dissolution coefficient	V	Volume
$\mathcal{E}$	Ratio of E_b to E_w	w	Vertical current speed
E_b	Energy for subducting bubbles	z	Depth
E_w	Energy lost by wave breaking		
g	Gravitational acceleration		
G	Percentage of diss. gas	α	Spectral slope of size distrib.
$\mathcal{G}$	Total percentage of diss. gas	γ	Bubble entrainment depth
$\mathcal{R}$	Radius of Langmuir vortex	λ	Wave length
N	Bubble size distribution	ρ	Water density
p_{atm}	Atmospheric pressure	σ	Oversaturation of gas in water
r	Bubble radius	χ	Mole fraction

Gas exchange in the Fraser Estuary

$\mathcal{E}$	Energy portion for bubble subduction	T	Temperature
D	Dissolution coefficient	$\mathcal{T}$	Duration of gas entrainment
k_j	Gas transfer velocity	$\mathcal{V}$	Void fraction
$\mathcal{L}$	Length of front	w	Vertical current speed
p_{atm}	Atmospheric pressure	$\mathcal{W}$	Width of front
P	Gas pressure		
Q	Gas flux	α	Spectral slope of size distrib.
r	Bubble radius	γ	Bubble entrainment depth
R	Universal gas constant	σ_j	Percentage oversaturation
S	Solubility	χ_j	Molefraction in dry air

Appendix

E_{kin}	Kinetic energy	z	Depth
E_{pot}	Potential energy		
g	Gravitational acceleration	ϑ	Beam angle of ADCP
u	Horizontal current speed	ρ_i	Density
w	Vertical current speed	φ	Angle of flow direction

B Observations

B.1 Tidal currents

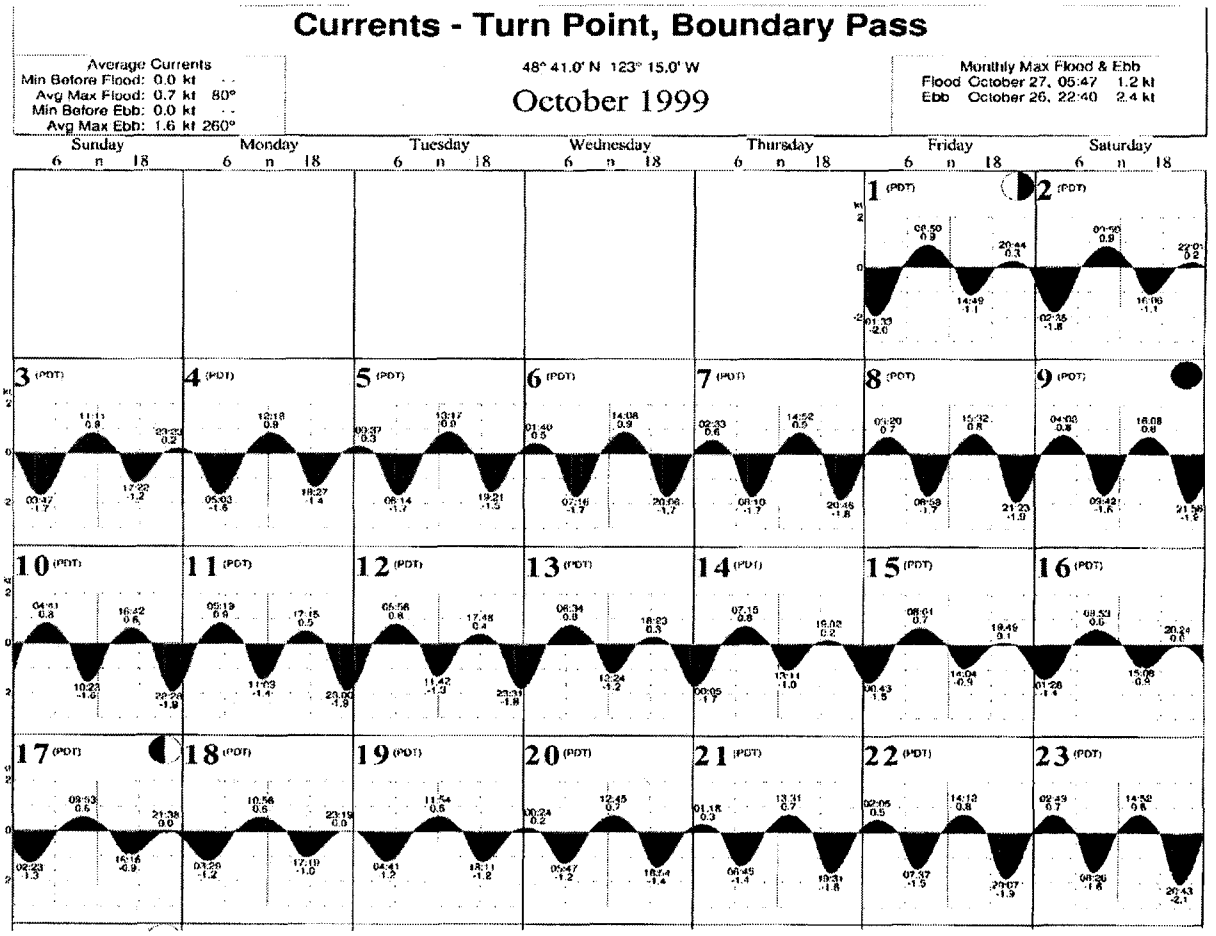

Figure B.1: *Tidal currents at Turn Point (Stuart Island) and Boundary Pass during CCGS Vector cruise 9934 (4-14 October 1999). Currents speeds above 0.75 kt and below −1.5 kt are marked in green and red, respectively. currents*

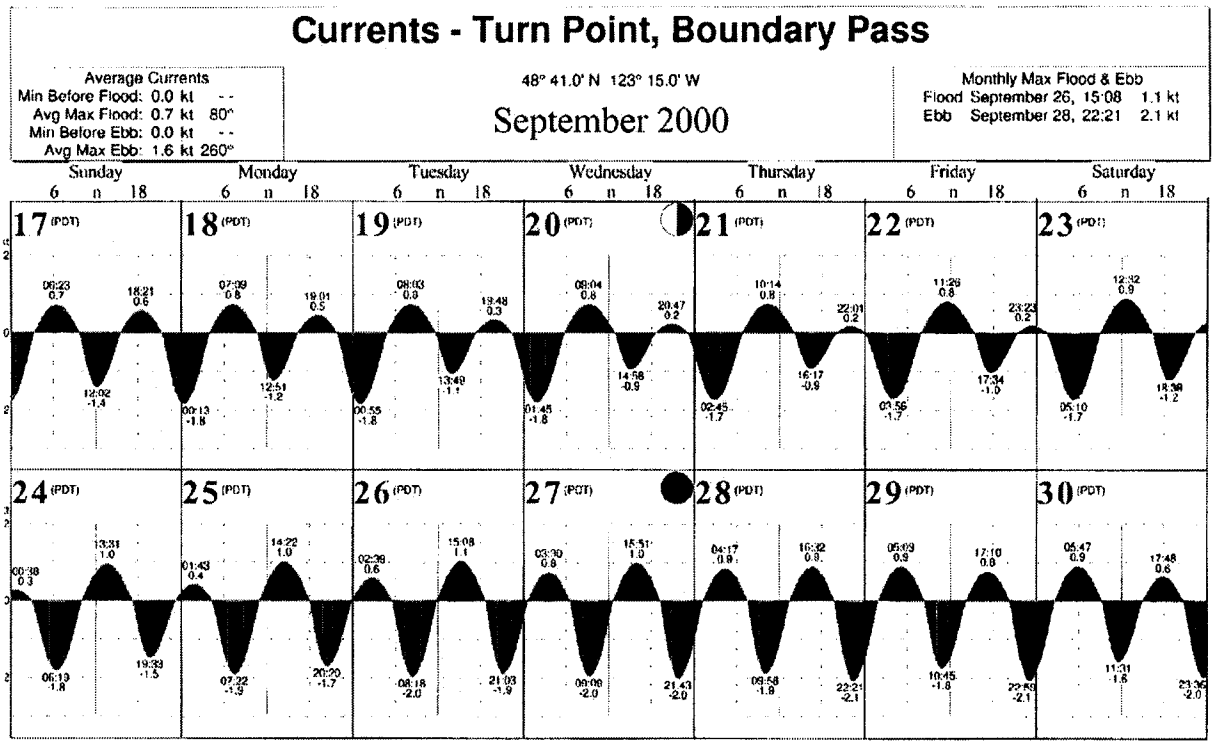

Figure B.2: *Tidal currents at Turn Point (Stuart Island) and Boundary Pass during CCGS Vector cruise 0032 (18-30 September 2000). Currents speeds above 0.75 kt and below −1.5 kt are marked in green and red, respectively.*

B.2 CTD-stations

CTD-Station	Latitude	Longitude	CTD-Station	Latitude	Longitude
A1	48°N 42.62′	123°W 14.12′	F5	48°N 43.90′	123°W 13.40′
A2	48°N 39.20′	123°W 09.50′	F6	48°N 43.65′	123°W 14.50′
A3	48°N 41.10′	123°W 07.20′			
A4	48°N 41.30′	122°W 59.60′	P1	48°N 46.70′	123°W 00.90′
A5	48°N 35.60′	123°W 03.20′	P2	48°N 47.40′	123°W 00.90′
A6	48°N 33.40′	123°W 12.00′	P3	48°N 48.80′	123°W 00.90′
			P4	48°N 49.50′	123°W 00.90′
B2	48°N 38.18′	123°W 12.22′	P5	48°N 46.70′	122°W 59.20′
B3	48°N 37.80′	123°W 12.44′	P6	48°N 47.40′	122°W 59.20′
B4	48°N 37.42′	123°W 12.66′	P7	48°N 48.40′	122°W 59.20′
B5	48°N 38.25′	123°W 11.54′	P8	48°N 49.50′	122°W 59.20′
B6	48°N 37.86′	123°W 11.71′			

Table B.1: *CTD stations during Vector cruises 9934 and 0032. A: Haro Strait and adjacent channels; B: Battleship Island; F: Stuart Island flood tidal front; P: Boundary Pass; S: Stuart Island ebb tidal front (see also Figures 2.1 and 2.2).*

CTD-Station	Latitude	Longitude	CTD-Station	Latitude	Longitude
B7	48°N 37.47′	123°W 11.89′	S1	48°N 15.15′	123°W 41.38′
B8	48°N 37.08′	123°W 12.07′	S2	48°N 15.32′	123°W 40.98′
B10	48°N 37.92′	123°W 10.99′	S3	48°N 14.90′	123°W 41.13′
B11	48°N 37.12′	123°W 11.20′	S4	48°N 14.48′	123°W 41.28′
B13	48°N 37.80′	123°W 09.99′	S5	48°N 14.58′	123°W 40.06′
B16	48°N 37.80′	123°W 08.98′	S6	48°N 14.17′	123°W 40.21′
B18	48°N 37.73′	123°W 13.19′	S7	48°N 13.76′	123°W 40.36′
B19	48°N 37.35′	123°W 13.38′	S8	48°N 13.80′	123°W 39.18′
B20	48°N 37.69′	123°W 07.30′	S9	48°N 13.40′	123°W 39.33′
B21	48°N 37.78′	123°W 05.45′	S10	48°N 13.00′	123°W 39.48′
			S15	48°N 40.82′	123°W 15.74′
F1	48°N 41.70′	123°W 13.70′	S16	48°N 39.90′	123°W 14.97′
F2	48°N 41.60′	123°W 12.50′	S17	48°N 39.03′	123°W 14.23′
F3	48°N 42.20′	123°W 12.70′	S18	48°N 40.72′	123°W 16.10′
F4	48°N 42.80′	123°W 12.90′	S19	48°N 39.75′	123°W 15.40′

Table B.2: *CTD stations during Vector cruises 9934 and 0032. A: Haro Strait and adjacent channels; B: Battleship Island; F: Stuart Island flood tidal front; P: Boundary Pass; S: Stuart Island ebb tidal front (see also Figures 2.1 and 2.2).*

B.3 Comparison of 2-beam and 4-beam solutions for ADCP measurements

The ADCP measures the Doppler shift for each of its four beams, which then yields the current speed along each beam. The calculation of horizontal and vertical current speed from the raw data is based on the assumption of horizontal homogeneity of the flow field. Each of the two beam pairs of the ADCP gives then a solution for the vertical current speed w and the horizontal current speed u/v in the plane of the beams, with one plane in the ship's direction and the other one orthogonal to it (in the configuration used during the cruises). The mean of the two values for w provides the vertical current speed while the difference yields an error velocity, which indicates if the assumption of homogeneity is valid (RDI, 1989).

This 4-beam solution is provided by the data processing software *transect*. However, tidal fronts are usually characterized by strong horizontal gradients of the flow field. The two beam pairs will be therefore treated separately (2-beam solution) for determining the vertical current speed w in order to study the robustness of the 4-beam solution. The horizontal current speed u has to be calculated in the same way though, unless the flow direction or magnitude is prescribed.

At Boundary Pass, the flow field close to the sill is mainly 2-dimensional, i.e. the currents in the plane parallel to the sill crest (orthogonal to the ship's direction) are relative homogeneous. It can therefore be assumed that the solution for w which is calculated from the beams parallel to the sill crest (beams #1 and #2) provides the most accurate estimate. This result will be compared to the 4-beam solution.

The ADCP measures the current speeds $u_{\#1}$ and $u_{\#2}$ in direction of beams #1 and #2 (Figure B.3). The horizontal and vertical flow components u and w can then be calculated by using

$$u = \frac{u_{\#1}}{\cos(\vartheta + \varphi)} \sin\varphi \quad , \quad w = \frac{u_{\#1}}{\cos(\vartheta + \varphi)} \cos\varphi \quad , \tag{B.1}$$

where $\vartheta = 20°$ is the beam angle of the ADCP and φ the angle between flow direction and

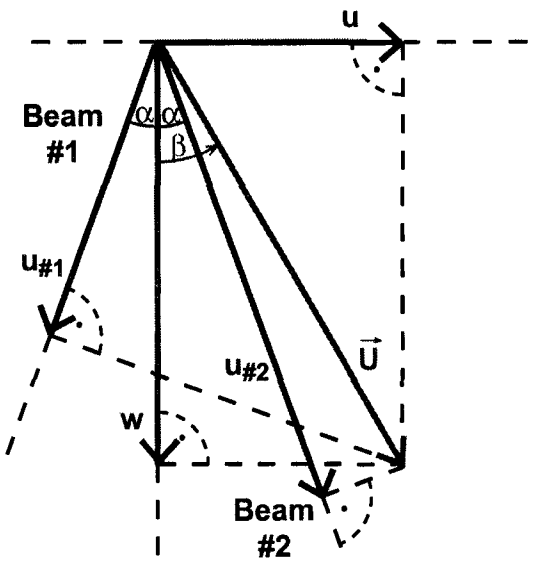

Figure B.3: *The current vector $\vec{U}$ (green) with its components u and w (red) is calculated from the currents in beam coordinates ($u_{\#1}$, $u_{\#2}$; blue). The angle between current vector and vertical z-axis is β and the beam angle of the ADCP is α.*

vertical z-axis, which is given by

$$\varphi = \vartheta + \arctan\left(\left[\cos(2\vartheta) - \frac{u_{\#1}}{u_{\#2}}\right] / \sin(2\vartheta)\right) \quad . \tag{B.2}$$

Figure B.4a shows the horizontal current speed u calculated from the 4-beam solution, which is identical to the result from the 2-beam solution as they are derived in the same way. The estimates of w from the 4-beam solution (b) show slightly lower values than the ones from the 2-beam solution (c). However, the differences (d) are $< 5\%$ in the strong downwelling regime close to the sill and have their highest values of about 10% in the mixing region downstream of it. This leads to the conclusion that also the 4-beam solution yields reasonable results, which is also true for the horizontal component u as it is directly linked to the value for w.

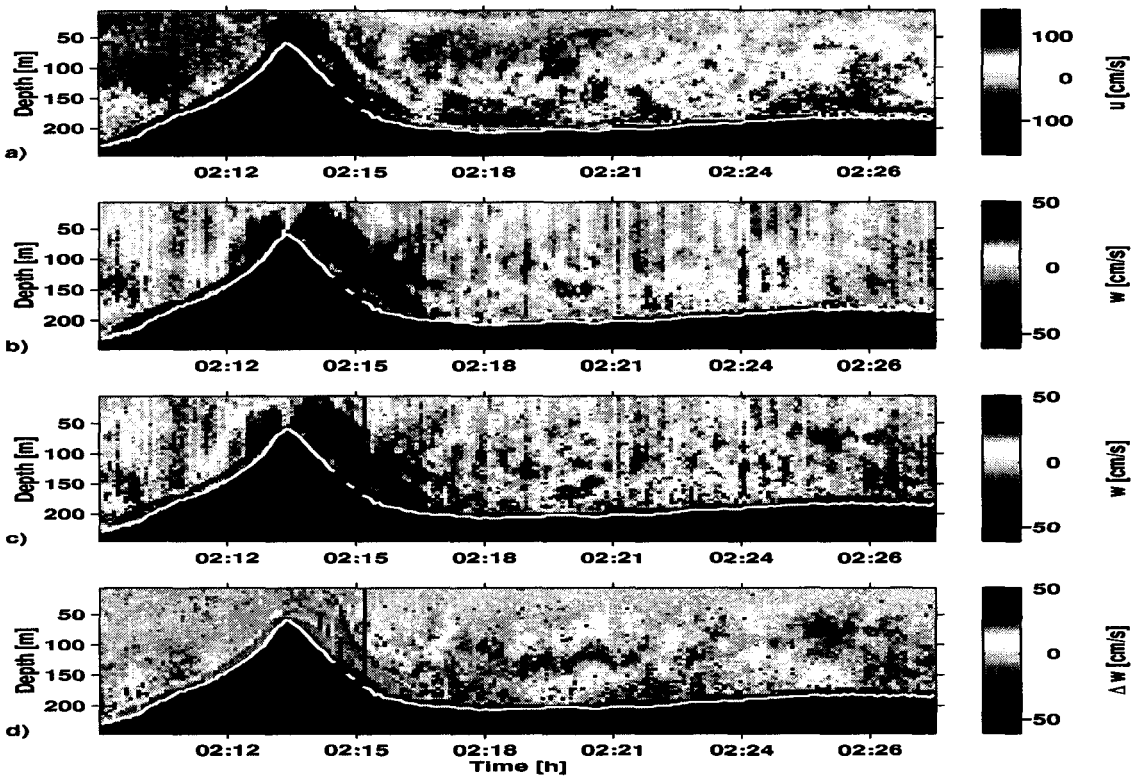

Figure B.4: *ADCP-transect at Boundary Pass. a) The horizontal current speed u calculated from the 4-beam solution, b) the vertical current speed w from the 4-beam solution, c) w from the 2-beam solution, d) the difference between w from the 2- and 4-beam solutions.*

B.4 Energy considerations for flow over an obstacle

A parcel of water has the tendency to flow around an obstacle rather than over it, as energy is required to lift it in a stratified environment. However, if the current speed (kinetic energy) is sufficient enough, it may flow over the obstacle.

The sill at Boundary Pass has a gap at the south-eastern side of the passage. At the beginning of the flood tidal period, the lower layer water flows from Boundary Pass through this gap into the Strait of Georgia, but not over the sill. Later on when the currents are stronger, the water is lifted over the sill establishing a hydraulically controlled two-layer flow (Section 2).

The current speed at which water of density ρ_2 from the lower layer is lifted over the sill can be estimated by simple considerations. The potential energy which is necessary for this is given for a parcel of water of unit volume by $E_{pot} = (\rho_2 - \rho_1) g \Delta z$, where ρ_1 is the density of the upper layer, g the gravitational acceleration, and Δz the height difference by which the water has to be lifted (e.g. sill height). The required energy can only be supplied by the kinetic energy $E_{kin} = 1/2\, \rho_2 u_2^2$ the water had upstream of the sill (u_2 is the current speed of the lower layer). Assuming that turbulent kinetic energy and energy dissipation by friction can be neglected, the energy is conserved. The ratio of potential and kinetic energy is given by

$$\frac{E_{pot}}{E_{kin}} = \frac{u_2^2}{2\,(1-\rho_1/\rho_2) g\, \Delta z} \quad . \tag{B.3}$$

If the ratio is > 1, then the amount of kinetic energy is sufficient to lift lower layer water over the sill, which is the case for a current speed u_2

$$u_2 > \sqrt{2(1-\rho_1/\rho_2)\, g\, \Delta z} \quad . \tag{B.4}$$

Typical values for the sill at Boundary Pass are $\rho_1 = 1022.5\,\mathrm{kg\,m^{-3}}$, $\rho_2 = 1024\,\mathrm{kg\,m^{-3}}$, and $\Delta z = 30\,\mathrm{m}$, which means that a current speed of $u_2 > 1\,\mathrm{m\,s^{-1}}$ is required to lift lower layer water over the sill. This matches well with the observations which show that the flow starts

to flow over the sill at about 2 h after low tide when the tides reach a current speed similar to the predicted one (Section 2).